

HIGH ORDER FINITE DIFFERENCE WENO SCHEMES FOR IDEAL
MAGNETOHYDRODYNAMICS

By

Xiao Feng

A DISSERTATION

Submitted to
Michigan State University
in partial fulfillment of the requirements
for the degree of

Mathematics — Doctor of Philosophy

2017

ABSTRACT

HIGH ORDER FINITE DIFFERENCE WENO SCHEMES FOR IDEAL MAGNETOHYDRODYNAMICS

By

Xiao Feng

In this dissertation we propose two high order finite difference numerical schemes for solving the ideal magnetohydrodynamic (MHD) equations.

The first scheme is single-stage single-step, maintains a divergence-free condition on the magnetic field, and has the capacity to preserve the positivity of the density and pressure. To accomplish this, we use a Taylor discretization of the Picard integral formulation (PIF) of the finite difference WENO method proposed in [*SINUM*, 53 (2015), pp. 1833–1856]. We use the version where fluxes are expanded to third-order accuracy in time, and for the fluid variables space is discretized using the classical fifth-order finite difference WENO discretization. We use constrained transport in order to obtain divergence-free magnetic fields, which means that we simultaneously evolve the magnetohydrodynamic (that has an evolution equation for the magnetic field) and magnetic potential equations alongside each other, and set the magnetic field to be the (discrete) curl of the magnetic potential after each time step. In this work, we compute these derivatives to fourth-order accuracy. In order to retain a single-stage, single-step method, we develop a novel Lax-Wendroff discretization for the evolution of the magnetic potential, where we start with technology used for Hamilton-Jacobi equations in order to construct a non-oscillatory magnetic field. The end result is an algorithm that is similar to our previous work [*JCP*, 268, (2014), pp. 302–325], but this time the time stepping is replaced through a Taylor method with the addition of a positivity-preserving limiter. Finally, positivity preservation is realized by introducing a parameterized flux limiter

that considers a linear combination of high and low-order numerical fluxes. The choice of the free parameter is then given in such a way that the fluxes are limited towards the low-order solver until positivity is attained. Given the lack of additional degrees of freedom in the system, this positivity limiter lacks energy conservation where the limiter turns on.

The second scheme is based on an alternative flux formulation of the WENO scheme [*JCP*, 77 (1988), pp. 439–471, *SIAM J. Sci. Comput.*, 35 (2013), pp. A1137–A1160, and *Methods Appl. Anal.*, 21 (2014), pp. 1–30], which can be applied on curvilinear meshes. This scheme computes the numerical flux by a Taylor expansion in space. The lowest order term in the expansion is computed by applying a Riemann solver to one-sided approximations to conserved quantities obtained from WENO interpolation. The higher order terms in the expansion are computed by central differences. An additional limiter based on the smoothness indicators from the WENO interpolation is applied to control the oscillations in the higher order terms. Constrained transport is done in a way similar to [*JCP*, 268, (2014), pp. 302–325]. A positivity preserving limiter similar to the one in the first scheme is applied in order to enhance the robustness of the scheme. When the Riemann solver used in this scheme is chosen to be a high resolution solver such as the HLLD solver, the scheme exhibits better resolution than schemes based on WENO reconstruction of fluxes and Lax-Friedrichs flux splitting.

We present numerical results for several standard test problems including smooth Alfvén wave problems (to verify formal order of accuracy), shock tube problems (to test the shock-capturing ability of the scheme), Orszag-Tang, and cloud shock interactions. These results assert the robustness and verify the high-order of accuracy of the proposed scheme.

ACKNOWLEDGMENTS

I would like to first express my sincere gratitude to my advisor, Professor Andrew Christlieb, for his continuous support of my PhD study. It was truly joyful and rewarding to work under his guidance. I would also like to thank the rest of my dissertation committee: Professor Yingda Cheng, Professor Sean Couch, Professor Keith Promislow, and Professor Jianliang Qian, for their insightful comments and advice.

My sincere thanks also goes to my fellow groupmates, friends, and collaborators, Dr. David Seal, Dr. Qi Tang, and Dr. Yan Jiang, for numerous stimulating discussions. I would also like to thank Ms. Barbara Miller for the example of professionalism she set for me, and for her tremendous help.

I am extremely grateful for my wife, Zhijie Yu, for she is the best life companion I can possibly imagine. Thank you and let's continue our explorations together!

Last but not the least, I would like to thank my parents for their support throughout the years. Thank you!

TABLE OF CONTENTS

LIST OF TABLES	vii
LIST OF FIGURES	viii
Chapter 1 Introduction	1
Chapter 2 The ideal MHD equations	9
2.1 Hyperbolicity of the ideal MHD equations	10
2.2 Discontinuities in the ideal MHD equations	12
Chapter 3 The WENO methodology	16
3.1 WENO interpolation	16
3.2 WENO reconstruction	20
Chapter 4 A high-order positivity-preserving single-stage single-step method for the ideal magnetohydrodynamic equation	22
4.1 A constrained transport framework	22
4.2 The Taylor-discretization PIF-WENO method	26
4.3 The evolution of the magnetic potential equation	27
4.3.1 The 2D magnetic potential equation	29
4.3.2 The 3D magnetic potential equation	35
4.4 Positivity preservation	38
4.5 Numerical results	45
4.5.1 Smooth Alfvén wave	45
4.5.1.1 Smooth Alfvén wave: The 2D problem	46
4.5.1.2 Smooth Alfvén wave: The 3D problem	46
4.5.2 2D rotated shock tube problem	48
4.5.3 2D Orszag-Tang vortex	53
4.5.4 2D rotor problem	55
4.5.5 Cloud-shock interaction	59
4.5.5.1 Cloud-shock interaction: The 2D problem	59
4.5.5.2 Cloud-shock interaction: The 3D problem	61
4.5.6 Blast wave example	63
4.5.6.1 Blast wave example: The 2D problem	63
4.5.6.2 Blast wave example: The 3D problem	64
4.5.7 Errors in energy conservation	64
Chapter 5 A high-order finite difference scheme for ideal magnetohydro- dynamics on curvilinear meshes based on an alternative for- mulation of the WENO scheme and constrained transport	70
5.1 An alternative flux formulation of the WENO scheme	71

5.1.1	Introduction	71
5.1.2	A limiter on the higher order terms in the numerical flux	73
5.1.3	One-dimensional systems	75
5.1.4	Multidimensional cases	78
5.1.5	Curvilinear meshes	79
5.2	HLL type Riemann solvers for MHD equations	80
5.2.1	The HLL approximate Riemann solver	82
5.2.2	The HLLC approximate Riemann solver	83
5.2.3	The HLLD approximate Riemann solver	87
5.3	Constrained transport	94
5.4	A positivity-preserving limiter	96
5.5	Numerical results	97
5.5.1	2D smooth Alfvén wave problem	97
5.5.2	Brio-Wu shock tube	98
5.5.2.1	1D shock tube	99
5.5.2.2	2D rotated shock tube	102
5.5.3	2D Orszag-Tang vortex	102
5.5.4	2D cloud-shock interaction	108
Chapter 6 Conclusions and future work		113
BIBLIOGRAPHY		116

LIST OF TABLES

<p>Table 4.1: 2D smooth Alfvén wave. Here, we show L^∞-errors at a final time of $t = 1.0$ for the solution with and without the energy “correction” step. Table (a) has the energy correction turned off, and Table (b) has the energy correction turned on. Because time is only discretized to third-order accuracy, we observe the predicted third-order accuracy of the solver here.</p>	47
<p>Table 4.2: 2D smooth Alfvén wave. Here, we show L^∞-errors at a short final time of $t = 0.01$ for the solution with and without the energy “correction” step. Table (a) has the energy correction turned off, and Table (b) has the energy correction turned on. Here, we refine Δt faster than Δx in order to expose the spatial order of accuracy of the solver. Because we only use a fourth-order accurate spatial discretization for $\nabla \times \mathbf{A}$, we only observe fourth-order accuracy despite the fact that the fluid variables are discretized to fifth-order accuracy.</p>	47
<p>Table 4.3: 3D smooth Alfvén wave. In this table we show the L^∞-errors at a moderate time of $t = 1.0$. In Table (a) the positivity-preserving limiter is off, and the the positivity-preserving limiter (and the energy correction step) is turned on for the results in Table (b). Because time is discretized to third-order accuracy, the final method is formally only third-order accurate in time. In Table 4.4 we run the solver to a short final time in order to expose the spatial order of accuracy.</p>	48
<p>Table 4.4: 3D smooth Alfvén wave. Here, we show the L^∞-errors at a short final time of $t = 0.01$. In addition, we refine Δt faster than the mesh spacing in order to extract the spatial order of accuracy. Table (a) has the positivity-preserving limiter turned off, and Table (b) has the positivity-preserving limiter (as well as the correction step) turned on. The results are almost identical.</p>	49
<p>Table 5.1: L^∞-errors in 2D smooth Alfvén problem. Alternative WENO with Lax-Friedrichs flux. Constrained transport and positivity-preserving limiter on.</p>	98
<p>Table 5.2: L^∞-errors in 2D smooth Alfvén problem. Alternative WENO with HLLD flux. Constrained transport and positivity-preserving limiter on.</p>	99

LIST OF FIGURES

<p>Figure 4.1: Stencil needed for magnetic potential. The values of A^z at each “×” (save the centermost value) is needed to correct the value of \mathbf{B} at the center. The shaded points are needed in Eqns. (4.26) and (4.30)–(4.34) to compute the value of A^z at the rightmost “×” point. Note that this stencil is contained in the stencil shown in [20], Fig. 2.</p>	34
<p>Figure 4.2: The rotated shock tube problem. Here, we compare the solver with (left panels) and without (right panels) constrained transport turned on. A uniform mesh of size 200×100 is used for both simulations. The angle of rotation for the initial conditions is $\phi = \tan^{-1}(0.5)$, and 30 equally spaced contours ranging from the minimum to the maximum of each function are used for the top two panels. The contour plot for the solution without CT contains small wiggles that are much more pronounced when slices of the solution are sampled. To this end, a slice of the solution along $y = 0$ is presented in the bottom two panels. Further evolution produces a solution that causes the code to fail in the case where CT is turned off. The positivity-preserving limiter is turned off in order to exercise the code. The solid lines in the bottom images are reference solutions that are computed by solving the equivalent 1D shock problem on a uniform mesh with 50,000 points with the fifth-order finite difference WENO method.</p>	51
<p>Figure 4.3: 2D rotated shock tube problem. The left panels have constrained transport turned on, and the right panels have constrained transport turned off. Components of the magnetic field at $t = 0.2$ along the slice $y = 0$. The mesh size is 200×100. The positivity-preserving limiter is turned off in order to exercise the code. Each solid line is the reference solution described in Fig. 4.2. We observe that constrained transport (with the Hamilton-Jacobi solver) allows us to numerically compute magnetic fields with far fewer oscillations than would otherwise be obtainable.</p>	52
<p>Figure 4.4: The Orszag-Tang problem. We show density contour plots at (a) $t = 0.5$, (b) $t = 2$, (c) $t = 3$, (d) $t = 4$. The solution is computed using PIF-WENO with constrained transport on and positivity-preserving limiter on, on a 192×192 mesh. A total of 15 equally spaced contours are used for each graph.</p>	54

Figure 4.5:	The Orszag-Tang problem. Density plots at $t = 1.5$ for solutions computed using different configurations in the numerical scheme. (a) PIF-WENO, with constrained transport turned off; (b) PIF-WENO with constrained transport and positivity preserving limiter turned on; (c) PIF-WENO with constrained transport turned on and positivity preserving limiter turned off; (d) The slice along $y = 0.5072$. The solutions are computed with a 192×192 mesh. A total of 15 equally spaced contours are used for each of (a), (b), and (c).	56
Figure 4.6:	The Orszag-Tang problem. Pressure plots at $t = 3.0$ for solutions computed using different configurations in the numerical scheme. (a) PIF-WENO with constrained transport turned on and positivity preserving limiter turned off; (b) PIF-WENO with constrained transport and positivity preserving limiter turned on; (c) The slice along $y = 1.9799$. The solutions are computed with a 192×192 mesh. A total of 15 equally spaced contours are used for each of (a) and (b).	57
Figure 4.7:	The 2D rotor problem. Shown here are (a) the pseudocolor plot of the magnetic pressure and (b) the magnetic field line. This solution is computed on a mesh of size 400×400 . Constrained transport and positivity-preserving limiters are turned on.	58
Figure 4.8:	The 2D cloud-shock interaction problem. Here, we run the solver to a final time of $t = 0.06$. In the first three panels, we show Schlieren plots for (a) the natural log of the density, (b) the norm of the magnetic field, and (c) the pressure for a mesh of size 256×256 . The same results for a mesh of size 512×512 are presented in panels (d)–(f), where we observe much higher resolution for the problem. Constrained transport and positivity-preserving limiter are turned on for both simulations.	60
Figure 4.9:	The 3D cloud-shock interaction problem. Schlieren plots of $\ln(\rho)$. The solution here is computed using a $256 \times 256 \times 256$ mesh. Cross-sections at $y = 0.5$ and $z = 0.5$ for the region $y \geq 0.5$ and $z \geq 0.5$ are shown. Constrained transport and positivity-preserving limiter are turned on.	62
Figure 4.10:	2D blast problem. Shown here are the contour plots at $t = 0.01$ of (a) density, (b) thermal pressure, (c) magnitude of velocity, and (d) magnetic pressure. A total of 40 equally spaced contours ranging from the min to the max of the function are used for each plot. The mesh size is 256×256	65
Figure 4.11:	3D blast problem. Shown here are the pseudocolor plots at $t = 0.01$ of (a) density and (b) pressure. The mesh size is $150 \times 150 \times 150$. In Figure 4.12 we plot a cut of the solution along $z = 0$. The positivity-preserving limiter is required to simulate this problem.	66

Figure 4.12: 3D blast problem. Shown are the contour plots at time $t = 0.01$ cut at $z = 0$ of (a) density, (b) thermal pressure, (c) norm of velocity, and (d) magnetic pressure. The solution is obtained using a $150 \times 150 \times 150$ mesh. A total of 40 equally spaced contours are used for each plot.	67
Figure 4.13: Energy conservation errors for the smooth Alfvén test cases. Shown here are results for the (a) 2D smooth Alfvén , and (b) 3D smooth Alfvén test cases. In order to extract the errors, we plot the results on a semi-log scale because otherwise the results are indiscernible from the t -axis. For this smooth test case, the effect of the the energy correction step (and hence the positivity-preserving limiter) is negligible because the solution remains smooth for the entire simulation.	68
Figure 4.14: Energy conservation errors. Shown here are conservation errors when the positivity-preserving limiter (and hence the energy correction step) is turned on. (a) 2D Orszag-Tang problem, (b) 2D rotor problem, (c) 2D blast problem, and (d) 3D blast problem. Note that the rotor and blast problems require the application of a positivity-preserving limiter in order to run, but this comes at the expense of losing energy conservation. For the Orszag-Tang test problem, we run to a late final time. Again, we observe that the errors in energy conservation decrease as the mesh is refined.	69
Figure 4.15: Energy conservation errors. Here, we show results for conservation errors when the positivity-preserving limiter (and hence the energy correction step) is turned off. The solver analytically conserves the discrete total energy up to machine precision. Shown here are results for the (a) 2D smooth Alfvén , and (b) 3D smooth Alfvén test cases. Note the logarithmic scale for the axes, and that these errors are numerically conserved up to machine precision.	69
Figure 5.1: A schematic diagram of the physical and computational domain for curvilinear meshes.	79
Figure 5.2: Perturbed mesh used for 2D Alfvén problem. 32×32 mesh. $(\xi, \eta) \in [0, 1]^2$. $x = \xi + 0.01 \sin(2\pi\eta \cdot 2)$, $y = \eta + 0.02 \sin(2\pi\xi \cdot 4)$	98
Figure 5.3: Brio-Wu shock tube. $t = 0.2$. Alternative WENO with Lax-Friedrichs flux. A uniform mesh of 200 points were used. Positivity-preserving limiter is turned on.	100
Figure 5.4: Brio-Wu shock tube. $t = 0.2$. Alternative WENO with HLLD flux. A uniform mesh of 200 points were used. Positivity-preserving limiter is turned on.	100

Figure 5.5:	Brio-Wu shock tube. $t = 0.2$. Alternative WENO with Lax-Friedrichs flux. A non-uniform mesh of 200 points were used. Positivity-preserving limiter is turned on.	101
Figure 5.6:	Brio-Wu shock tube. $t = 0.2$. Alternative WENO with HLLD flux. A non-uniform mesh of 200 points were used. Positivity-preserving limiter is turned on.	101
Figure 5.7:	Rotated Brio-Wu shock tube. $t = 0.2$. Alternative WENO with Lax-Friedrichs flux. 200×100 uniform mesh. Constrained transport and positivity-preserving limiter turned off.	103
Figure 5.8:	Rotated Brio-Wu shock tube. $t = 0.2$. Alternative WENO with Lax-Friedrichs flux. 200×100 uniform mesh. Constrained transport and positivity-preserving limiter turned on.	104
Figure 5.9:	Rotated Brio-Wu shock tube. $t = 0.2$. Alternative WENO with HLLD flux. 200×100 uniform mesh. Constrained transport and positivity-preserving limiter turned on.	105
Figure 5.10:	Orszag-Tang test problem. Contour plot of density at $t = 3$. A perturbed 192×192 mesh. 15 equally spaced contour lines. Alternative WENO with Lax-Friedrichs flux. Constrained transport and positivity-preserving limiter turned on.	106
Figure 5.11:	Orszag-Tang test problem. Plot of density at $t = 3$. A perturbed 192×192 mesh. 15 equally spaced contour lines. Alternative WENO with HLLD flux. Constrained transport and positivity-preserving limiter turned on.	107
Figure 5.12:	2D cloud-shock interaction. Alternative WENO with Lax-Friedrichs flux. 256×256 uniform mesh. Schlieren plots at $t = 0.06$. Constrained transport and positivity-preserving limiter turned on.	109
Figure 5.13:	2D cloud-shock interaction. Alternative WENO with HLLD flux. 256×256 uniform mesh. Schlieren plots at $t = 0.06$. Constrained transport and positivity-preserving limiter turned on.	109
Figure 5.14:	Sketch of the non-uniform mesh used in cloud-shock problem. Actual mesh is 256×256 . A 32×32 mesh is shown here for clarity.	110
Figure 5.15:	2D cloud-shock interaction. Alternative WENO with Lax-Friedrichs flux. 256×256 non-uniform mesh. Schlieren plots at $t = 0.06$. Constrained transport and positivity-preserving limiter turned on. The second row shows the region near the center of the computational domain.	111

Figure 5.16: 2D cloud-shock interaction. Alternative WENO with HLLD flux. 256×256 non-uniform mesh. Schlieren plots at $t = 0.06$. Constrained transport and positivity-preserving limiter turned on. The second row shows the region near the center of the computational domain. 112

Chapter 1

Introduction

A plasma is a substance where a sufficiently large portion consists of free charged particles, so that due to the electromagnetic forces, which are long-range in nature, the substance as a whole exhibits *collective behaviors* [11]. Magnetohydrodynamics (MHD) are single-fluid models for plasmas where it is assumed that the plasma is quasi-neutral (zero net charge in any spatial scales under consideration). The ideal MHD equations further assume perfect conductivity (zero electric resistance). Although it is one of the simplest models of plasmas, it is nonetheless a “remarkably accurate description of the low-frequency, long-wavelength dynamics of real plasmas” [72]. As a consequence, the MHD equations, both ideal and non-ideal, find applications in a wide range of areas including space physics and controlled thermonuclear fusion [53, 11].

In this dissertation, we propose and investigate two high-order finite difference numerical schemes for ideal MHD equations based on the Weighted Essentially Non-Oscillatory (WENO) methodology. The first scheme is a single-stage, single-step scheme that is designed with the goal of embedding in Adaptive Mesh Refinement frameworks and achieving low storage in mind. The second scheme is a scheme based on an alternative flux formulation of the WENO scheme, which can be applied on curvilinear meshes. In both schemes, we use unstaggered constrained transport, where a magnetic potential is evolved along side with the MHD quantities, to control the divergence error of the magnetic field, and we use a flux

limiter to retain the positivity of the density and pressure in MHD.

High-order numerical schemes based on the Essentially Non-Oscillatory (ENO) [61] as well as the Weighted ENO (WENO) reconstruction technique [50, 59, 2, 75, 4, 23, 17] have been applied successfully to ideal MHD in the past two decades. These high order schemes are capable of resolving complex features such as shocks and turbulences using fewer grid points than low-order schemes for the same level of error, as is common with many high-order shock-capturing schemes.

It often happens in large-scale MHD simulations that the complex features are concentrated in a small portion of the simulation domain. Adaptive mesh refinement (AMR) is a technique that is designed for treating such locality of complexity in hydrodynamics and magnetohydrodynamics. One of the main difficulties with implementing high order schemes within an AMR framework is that boundary conditions for the refined region need to be specified in a consistent manner [62]. This becomes difficult for multistage Runge-Kutta (RK) methods, because high order solutions cannot be found if one simply uses high-order interpolated values (in time) at the ghost points that are required for the intermediate stages of the method. Preliminary work that combines WENO spatial discretizations with strong stability preserving Runge-Kutta (SSP-RK) time-stepping is conducted in [74, 92], and very recent work makes use of curvilinear grids to extend finite difference methods to problems with geometry [17]. However, the authors in [17] use global time steps (which precludes the possibility of introducing local time stepping), and perhaps more troublesome, they drop mass conservation for their framework to work.

In choosing building blocks for AMR code, it has been argued that single-stage, single-step methods are advantageous [24, 5], partly because fewer synchronizations are needed per step than multistage RK methods. The fact that single-stage, single-step methods do not

have an issue with these synchronizations is possibly one of the reasons they have gained much attention in the past two decades, and one reason we choose to pursue these methods. Broadly construed, these methods are based on Lax and Wendroff’s original idea of using the Cauchy-Kovalevskaya procedure to convert temporal derivatives into spatial derivatives in order to define a numerical method [54]. Notable high-order single-stage, single-step methods include the Arbitrary DERivative (ADER) methods [85, 87], the Lax-Wendroff finite difference WENO methods [68], the Lax-Wendroff discontinuous Galerkin (DG) methods [67] and space-time schemes applied directly to second-order wave equations [45, 9]. Of the three classes of high-order methods based upon Lax-Wendroff time stepping, only the ADER methods have been applied to magnetohydrodynamics [5, 4, 13], whereas similar investigations have not been done for the other classes. An additional advantage that single-stage single-step Taylor methods offer is their *low-storage* opportunities. This requires care, because these methods can easily end up requiring the same amount of storage as their equivalent RK counterpart (e.g., if each time derivative is stored in order to reduce coding complexity).

The single-stage single-step scheme we propose in this dissertation is based on the Taylor discretization of the Picard integral formulation of the finite difference WENO (PIF-WENO) method [20]. Compared with other WENO methods that use Lax-Wendroff time discretizations [68], our method has the advantage that its focus is on constructing high-order Taylor expansions of the fluxes (which are used to define a conservative method through WENO reconstruction) as opposed to the conserved variables. This allows, for example, the adaptation of a positivity-preserving limiter, which we describe in this document.

The other scheme we propose in this dissertation is based on an alternative flux formulation of WENO schemes [51, 52]. In this alternative formulation, the numerical flux is

computed by applying a Riemann solver to approximations of conserved quantities obtained by WENO interpolation. This approach can be found in the early work of Shu and Osher on ENO schemes [78]. However, direct reconstruction of numerical fluxes has enjoyed a widespread popularity from early on (see [41] and the references therein), in part due to the lower computational cost. One disadvantage of this direct reconstruction approach, though, is that the incorporation of upwinding into the scheme is commonly done through the very diffusive Lax-Friedrichs flux splitting. The alternative flux formulation can mitigate this problem by using less diffusive Riemann solvers. For more discussion on the advantages of this alternative formulation, we refer the reader to [51, 52].

The idea of using Riemann solvers in numerical schemes for hyperbolic conservation laws has its root in the seminal work of Godunov [35]. Since then, a tremendous amount of effort has been put in pursuit of good approximate Riemann solvers. Notable work on Euler equations for hydrodynamics include the work of Godunov [36], Roe [69], Harten et al [42], and Toro et al [88]. The Harten-Lax-van Leer (HLL) solver in [42] assumes one intermediate state in the approximate solution to the Riemann problem. The HLLC (C for contact discontinuity) solver in [88] improved upon that by assuming two intermediate states and making use of knowledge specific to the Euler equation to achieve exact resolution of isolated contact discontinuities. Similar ideas were applied to magnetohydrodynamics in the work of Gurski [40], Li [58], and Miyoshi and Kusano [64]. Of these solvers, the HLLD (D for discontinuities) solver in [64] assumes the largest number of intermediate states (four) in the approximate solution and is capable of resolving contact, rotational, and tangential discontinuities exactly, and, when the estimates of fastest signal speeds are exact, also resolving fast shocks exactly. This solver has since been used in many mature MHD simulation codes including FLASH [29] and Athena [82].

We remark here that there has been an ongoing, inconclusive debate on the correct conditions to single out the physically correct weak solution to a Riemann problem for ideal MHD. The entropy conditions that worked very well for Euler equations (see, e.g., [55]) cannot serve this purpose for MHD equations because of lack of convexity in the MHD fluxes [89]. In numerical tests for the shock tube problem first examined by Brio and Wu in [15], intermediate shocks, which were deemed inadmissible by earlier criteria [48], show up ubiquitously in the results. Due to lack of decisive evidence from physical observations and experiments (however, see [32]), currently there is no agreement on the physical reality of intermediate shocks. Takahashi and Yamada [83] gives an excellent review of the current controversy and also reports their own study of this issue, which are in favor of Falle and Komissarov’s argument [31] that the apparent intermediate shocks are actually a consequence of a certain symmetry in the setup of the shock tube problem. We also refer the reader to the same authors’ work [84] for the description of an exact MHD Riemann solver, where one could switch between the various admissibility conditions.

Another issue that we address in our second scheme is the handling of curvilinear meshes (also called structured grids by some authors). One reason for solving the MHD equations on curvilinear meshes is because the geometry for certain MHD applications is best described by a non-Cartesian coordinate system [28, 70, 37, 81]. More recent work include, for example, that of Chacon [16] and Stegmeir et al [80]. See also [17] for a very recent piece of work on high order numerical schemes for generic hyperbolic conservation law on curvilinear meshes. The way we handle curvilinear meshes in the (second) scheme in this dissertation follows the method in [52], where a hyperbolic system of conservation laws on the Cartesian coordinates is transformed to one on the curvilinear coordinates. We refer the reader to the references therein for further discussions.

An important issue in simulations of MHD systems is the controlling of the divergence error of the magnetic field, since numerical schemes based on the transport equations alone will, in general, accumulate errors in the divergence of the magnetic field. Failure to address this issue creates an unphysical force parallel to the magnetic field [14], and if this is not taken care of, it will often lead to failure of the simulation code. Popular techniques used to solve this problem include (1) the non-conservative eight-wave method [38], (2) the projection method [14], (3) the hyperbolic divergence cleaning method [27], and (4) the various constrained transport methods [1, 8, 23, 25, 30, 33, 43, 44, 71]. Tóth conducted an extensive survey in [90].

Both schemes proposed in this dissertation uses the unstaggered constrained transport framework proposed by Rossmannith [71]. This framework evolves a vector potential that sits on the same mesh as the conserved quantities. This vector potential is then used to correct the magnetic field. Historically, the term “constrained transport” has been used to refer to a class of methods that incorporate the divergence-free condition into the discretization of the transport equation of the magnetic field, often done in a way that can be interpreted as maintaining an electric field on a staggered mesh [30, 90]. Some authors actually still distinguish between this type of “constrained transport” and the “vector potential” approach [47]. However, as is well-known, evolving a vector potential is conceptually equivalent to evolving an electric field. The unstaggered approach has the added benefit of ease for potential embedding in an AMR framework.

An important piece in any vector-potential based constrained transport method is the discretization of the evolution equation of the vector potential. This evolution equation is a nonconservative weakly hyperbolic system, and it can be treated numerically from this viewpoint [44]. An alternative approach is to view it as a modified system of Hamilton-Jacobi

equations [23]. Both schemes proposed in this dissertation adopts the latter approach. The first, single-stage, single-step scheme uses a method inspired by a Lax-Wendroff numerical scheme for Hamilton-Jacobi equations that was proposed in [66]. The artificial resistivity terms used in [23] are adapted into the present single-stage, single-step scheme. The second scheme, which is based on an alternative flux formulation of the WENO scheme, uses the same method as in [23] to evolve the vector potential, with necessary transformations when applied on curvilinear meshes.

One further challenge for numerical simulations of MHD is that of retaining the positivity of the density and pressure. This is critical when the thermal pressure takes up only a small portion of the total energy, i.e., when the β value is small. Almost all positivity-preserving methods exploit the presumed positivity-preserving property of certain low-order schemes, such as the Lax-Friedrichs scheme. Whereas earlier methods often rely on switching between high- and low-order updates [7, 46], more recent work tends to use combinations of the two. Examples include the work of Balsara [3] and Cheng et al. [18], which limit the conserved quantities at certain nodal points, and the work of Christlieb et al. [22], which combines high- and low-order fluxes through a single free parameter at each flux interface. In the current work, we adopt an approach similar to that used in [22]. This approach seeks a suitable convex combination of the high- and low-order fluxes at each cell at each time step. This flux limiter we adopt is an adaptation of the maximum principle preserving (MPP) flux limiter [93] (that has its roots in flux corrected transport schemes [12, 95]) for the purposes of retaining positivity of the density and pressure. We note that positivity-preserving has also been investigated for hydrodynamics. The limiters mentioned in this paragraph can be viewed as generalizations of limiters that have been applied to Euler's equations [96, 21, 73].

The rest of this dissertation is as follows. We will first briefly review ideal MHD equations

in Chapter 2 and then review the WENO methodology and include the interpolation and reconstruction formulas we use for future reference in Chapter 3. After that, in Chapter 4, we propose and investigate our first scheme, a single-stage, single-step high order finite difference numerical scheme for ideal MHD equations. In Chapter 5, we propose and investigate our second scheme, a high order finite difference numerical scheme for ideal MHD equations, based on an alternative flux formulation of the WENO scheme and applicable to curvilinear meshes. In Chapter 6, we draw our conclusions.

Chapter 2

The ideal MHD equations

In this chapter, we briefly review the ideal MHD equations. In particular, we will review its hyperbolicity and discontinuities, both of which will be used later.

In the conservation form, the (normalized) ideal MHD equations are

$$\partial_t \begin{bmatrix} \rho \\ \rho \mathbf{u} \\ \mathcal{E} \\ \mathbf{B} \end{bmatrix} + \nabla \cdot \begin{bmatrix} \rho \mathbf{u} \\ \rho \mathbf{u} \otimes \mathbf{u} + p_{\text{tot}} \mathbb{I} - \mathbf{B} \otimes \mathbf{B} \\ \mathbf{u}(\mathcal{E} + p_{\text{tot}}) - \mathbf{B}(\mathbf{u} \cdot \mathbf{B}) \\ \mathbf{u} \otimes \mathbf{B} - \mathbf{B} \otimes \mathbf{u} \end{bmatrix} = 0, \quad (2.1)$$

$$\nabla \cdot \mathbf{B} = 0, \quad (2.2)$$

where ρ is the mass density, $\rho \mathbf{u}$ is the momentum density, \mathcal{E} is the total energy density, \mathbf{B} is the magnetic field, p is the thermal pressure, $\|\cdot\|$ is the Euclidean vector norm, $p_{\text{tot}} = p + \frac{1}{2}\|\mathbf{B}\|^2$ is the total pressure, $\gamma = 5/3$ is the ideal gas constant, and the pressure satisfies the equation of state

$$\mathcal{E} = \frac{p}{\gamma - 1} + \frac{\rho \|\mathbf{u}\|^2}{2} + \frac{\|\mathbf{B}\|^2}{2}. \quad (2.3)$$

Here the quantities are normalized in such a way that the permeability and permittivity do not show up explicitly in the equations. In other words, we choose a unit system in which they are both equal to 1.

2.1 Hyperbolicity of the ideal MHD equations

We now briefly review the definition of a hyperbolic system of conservation laws, of which the ideal MHD equations (2.1) are an example. A more thorough treatment can be found in [56]. We also briefly review the waves in the ideal MHD equations in this section, which can be found in most of MHD literature. See, for example, [48, 10].

Definition 2.1. An *hyperbolic system of conservation laws* is a system of equations of the form

$$\partial_t \mathbf{q} + \nabla \cdot \mathbb{F} = 0, \quad (2.4)$$

where the *conserved quantities* \mathbf{q} , which is a vector function of time t and space \mathbf{x} , and the *flux tensor* \mathbb{F} , which is a (rank-2) tensor function of \mathbf{q} , are subject to the condition that for all (unit) direction vector \mathbf{n} , the Jacobian $\mathbf{n} \cdot \frac{\partial \mathbb{F}}{\partial \mathbf{q}}$ is diagonalizable with real eigenvalues.

In Definition 2.1, if we assume we have n components in \mathbf{q} and m dimensions in space and write out the components, we have

$$\begin{aligned} \mathbf{q} &= (q_j)_{j=1,\dots,n}, & \mathbb{F} &= (F_{i,j})_{i=1,\dots,m, j=1,\dots,n}, \\ \mathbf{n} &= (n_i)_{i=1,\dots,m}, & \mathbf{n} \cdot \frac{\partial \mathbb{F}}{\partial \mathbf{q}} &= \sum_{i=1}^m n_i \left(\frac{\partial F_{i,j}}{\partial q_k} \right)_{j,k=1,\dots,n}. \end{aligned} \quad (2.5)$$

For future reference, we also write out the flux in the \mathbf{n} direction, which is

$$\mathbf{n} \cdot \mathbb{F} = \left(\sum_{i=1}^m n_i F_{i,j} \right)_{j=1,\dots,m}. \quad (2.6)$$

The diagonalizability condition of the Jacobian in Definition 2.1 means that locally in any direction at any point in space, the structure of \mathbf{q} is approximately that of plane waves. The

eigenvalues of $\mathbf{n} \cdot \frac{\partial \mathbb{F}}{\partial \mathbf{q}}$ are the speeds of the waves in direction \mathbf{n} at a given point. We note however that in the case when \mathbb{F} is not a linear function of \mathbf{q} , the solution to Equation 2.4 can and usually does develop very complex structures as time evolves.

In the ideal MHD system 2.1, the wave speeds are given by

$$\lambda_{1,8} = \mathbf{u} \cdot \mathbf{n} \mp c_f \quad (\text{fast magnetosonic waves}), \quad (2.7)$$

$$\lambda_{2,7} = \mathbf{u} \cdot \mathbf{n} \mp c_a \quad (\text{Alfvén waves}), \quad (2.8)$$

$$\lambda_{3,6} = \mathbf{u} \cdot \mathbf{n} \mp c_s \quad (\text{slow magnetosonic waves}), \quad (2.9)$$

$$\lambda_4 = \lambda_5 = \mathbf{u} \cdot \mathbf{n} \quad (\text{entropy and divergence waves}), \quad (2.10)$$

where

$$a = \sqrt{\frac{\gamma p}{\rho}} \quad (\text{sound speed}), \quad (2.11)$$

$$c_a = \sqrt{\frac{(\mathbf{B} \cdot \mathbf{n})^2}{\rho}} \quad (\text{Alfvén speed}), \quad (2.12)$$

$$c_f = \left(\frac{1}{2} \left(a^2 + \frac{\|\mathbf{B}\|^2}{\rho} + \sqrt{\left(a^2 + \frac{\|\mathbf{B}\|^2}{\rho} \right)^2 - 4a^2 \frac{(\mathbf{B} \cdot \mathbf{n})^2}{\rho}} \right) \right)^{\frac{1}{2}} \quad (\text{fast magnetosonic speed}), \quad (2.13)$$

$$c_s = \left(\frac{1}{2} \left(a^2 + \frac{\|\mathbf{B}\|^2}{\rho} - \sqrt{\left(a^2 + \frac{\|\mathbf{B}\|^2}{\rho} \right)^2 - 4a^2 \frac{(\mathbf{B} \cdot \mathbf{n})^2}{\rho}} \right) \right)^{\frac{1}{2}} \quad (\text{slow magnetosonic speed}). \quad (2.14)$$

We note that the eigen decomposition of the Jacobian for ideal MHD is very complicated and is itself a subtle issue. The work in this dissertation all uses the decomposition given

in [10].

2.2 Discontinuities in the ideal MHD equations

A distinguished feature of the hyperbolic system (2.4) is that a solution in the classical sense usually do not exist for all time t . Discontinuities often develop, even if the initial conditions are smooth. Therefore, one considers *weak solutions* to Equation (2.4), which are functions \mathbf{q} that satisfy the corresponding *integral form of conservation laws*, and could possibly contain discontinuities.

We now review the types of discontinuities in the ideal MHD equations (2.1). This knowledge will later be applied in Section 5.2.

For the hyperbolic system of conservation laws (2.4), suppose we start with the initial conditions

$$\mathbf{q}(t = 0, \mathbf{x}) = \begin{cases} \mathbf{q}_L, & \text{if } \mathbf{n} \cdot \mathbf{x} < 0, \\ \mathbf{q}_R, & \text{if } \mathbf{n} \cdot \mathbf{x} \geq 0, \end{cases} \quad (2.15)$$

where \mathbf{q}_L and \mathbf{q}_R are constant vectors, and \mathbf{n} is an arbitrary direction vector. This is called a *Riemann problem*. The solution to such a problem is a function \mathbf{q} that depends only on t and $\mathbf{n} \cdot \mathbf{x}$. We are interested in the case when the solution consists of a single moving discontinuity, that is, when

$$\mathbf{q}(t, \mathbf{x}) = \begin{cases} \mathbf{q}_L, & \text{if } \mathbf{n} \cdot \mathbf{x} < St, \\ \mathbf{q}_R, & \text{if } \mathbf{n} \cdot \mathbf{x} \geq St, \end{cases} \quad (2.16)$$

where S is the speed at which the discontinuity moves. In this case, the integral form of the

hyperbolic conservation law mandates the *Rankine-Hugoniot condition*

$$S(\mathbf{q}_R - \mathbf{q}_L) = \mathbf{n} \cdot \mathbb{F}(\mathbf{q}_R) - \mathbf{n} \cdot \mathbb{F}(\mathbf{q}_L). \quad (2.17)$$

In the ideal MHD equations, the divergence condition (2.2) implies that the magnetic field in the initial conditions (2.15) must satisfy

$$\mathbf{n} \cdot \mathbf{B}_L = \mathbf{n} \cdot \mathbf{B}_R. \quad (2.18)$$

Under the condition (2.18), the Rankine-Hugoniot condition (2.17) implies that a single moving discontinuity in ideal MHD must be one from the following list.

1. A (fast or slow) *shock*. In this case, we have

$$\mathbf{n} \cdot \mathbf{u}_L, \mathbf{n} \cdot \mathbf{u}_R \neq S, \quad (2.19)$$

$$\mathbf{n} \cdot \mathbf{u}_L \neq \mathbf{n} \cdot \mathbf{u}_R, \quad (2.20)$$

$$\rho_L \neq \rho_R. \quad (2.21)$$

2. A *rotational discontinuity*. In this case, we have

$$\mathbf{n} \cdot \mathbf{u}_L, \mathbf{n} \cdot \mathbf{u}_R \neq S, \quad (2.22)$$

$$\mathbf{n} \cdot \mathbf{u}_L = \mathbf{n} \cdot \mathbf{u}_R, \quad (2.23)$$

$$\rho_L = \rho_R, \quad (2.24)$$

$$(\mathbf{u}_R - \mathbf{u}_L)_t = \frac{1}{\sqrt{\rho}}(\mathbf{B}_R - \mathbf{B}_L)_t, \quad (2.25)$$

where $(\cdot)_t$ represents the vector component tangential to the discontinuity interface (i.e., the component perpendicular to \mathbf{n}).

3. A *contact discontinuity*. In this case, we have

$$\mathbf{n} \cdot \mathbf{B} \neq 0, \tag{2.26}$$

$$\mathbf{B}_L = \mathbf{B}_R, \tag{2.27}$$

$$\mathbf{u}_L = \mathbf{u}_R, \tag{2.28}$$

$$p_L = p_R. \tag{2.29}$$

4. A *tangential discontinuity*. In this case, we have

$$\mathbf{n} \cdot \mathbf{B} = 0, \tag{2.30}$$

$$p_{\text{tot}L} = p_{\text{tot}R}. \tag{2.31}$$

Here we can have arbitrary jumps in the tangential velocities and tangential magnetic fields.

Remark 2.1. We note that (fast or slow) shocks are the only types of discontinuities that can possibly admit jumps in the normal velocities or the total pressures.

Remark 2.2. Rotational, contact, and tangential discontinuities are *linearly degenerate*. Rotational discontinuities correspond to Alfvén waves. Contact and tangential discontinuities correspond to entropy and divergence waves. None of the discontinuities in this list is genuinely nonlinear.

Remark 2.3. We mentioned that $\mathbf{n} \cdot \mathbf{B}$ must be the same on the two sides of the discontinuity.

ity. However, in Section 5.2, when we look at approximate Riemann solvers to be used in numerical schemes for multidimensional problems, we will need to solve Riemann problems where this condition does not hold. We will discuss how we handle this issue in that section.

Remark 2.4. For more discussions on weak solutions, integral forms of conservation laws, Rankine-Hugoniot conditions, linear degeneracy, and genuine non-linearity, see [56]. For more discussions on discontinuities in the ideal MHD equations, see [83].

Chapter 3

The WENO methodology

In this chapter, we give a brief description of the WENO interpolation and reconstruction procedures for future references. The discussion mostly follows [77].

3.1 WENO interpolation

Consider a uniform mesh with $x_i = i\Delta x$. Let r be a positive integer and $m = 2r - 1$. Suppose we want to interpolate the one-sided approximation $q_{i+1/2}^-$ from values of q on an m -point (biased) stencil

$$S^- = \{x_{i-r+1}, \dots, x_{i+r-1}\}. \quad (3.1)$$

A polynomial interpolation over S^- would give $q_{i+1/2}^-$ as a linear combination of the values $\{q_{i-r+1}, \dots, q_{i+r-1}\}$, which can then be written as a convex linear combination of the interpolations obtained from r -point substencils of S^- . To be more precise, let

$$S_k = \{x_{i-r+1+k}, \dots, x_{i+k}\}, \text{ where } k = 0, \dots, r-1 \quad (3.2)$$

be the r -point substencils of S^- . The polynomial interpolation over S gives

$$q_{i+1/2}^- = \sum_{s=-r+1}^{r-1} b_s q_{i+s} = q(x_{i+1/2}) + \mathcal{O}(\Delta x^{2r-1}), \quad (3.3)$$

where b_s 's are constant coefficients. Similarly, the polynomial interpolation over S_k gives

$$q_{i+1/2}^{(k)} = \sum_{s=-r+1}^0 b_s^{(k)} q_{i+k+s} = q(x_{i+1/2}) + \mathcal{O}(\Delta x^r), \quad (3.4)$$

where $b_s^{(k)}$'s are constant coefficients. There then exist constant positive numbers d_k such that

$$q_{i+1/2}^- = \sum_{k=0}^{r-1} d_k q_{i+1/2}^{(k)} \quad (3.5)$$

and

$$\sum_{k=0}^{r-1} d_k = 1. \quad (3.6)$$

In the WENO literature, d_k 's are called *linear weights*, because the approximation $q_{i+1/2}^-$ defined by Equations (3.4) and (3.5) is a linear combination of the q_i 's. When q is discontinuous within S^- , the polynomial interpolation gives rise to excessive oscillations. This is known as the *Runge's phenomenon* or the *Gibb's phenomenon*. The WENO methodology tackles this problem by replacing d_k with some ω_k which satisfies

$$\sum_{k=0}^{r-1} \omega_k = 1 \quad (3.7)$$

and

$$\begin{aligned} \omega_k &= d_k + \mathcal{O}(\Delta x^{r-1}), & \text{when } q \text{ is smooth on } S^-, \text{ and} \\ \omega_k &= \mathcal{O}(\Delta x^{r-1}), & \text{when } q \text{ is discontinuous on } S_k. \end{aligned} \quad (3.8)$$

In order to obtain ω_k 's satisfying Equation (3.8), we can first compute *smoothness indicators*

of the polynomial interpolants over the substencils by setting

$$\beta_k = \sum_{l=1}^{r-1} \int_{x_{i-1/2}}^{x_{i+1/2}} \Delta x^{2l-1} \left(\frac{\partial^l p_k(x)}{\partial^l x} \right)^2 dx, \quad (3.9)$$

where $p_k(x)$ is the polynomial that interpolates $q_{i+1/2}^{(k)}$ from the values of q on S_k . From these smoothness indicators we compute the unnormalized weights

$$\alpha_k = \frac{d_k}{(\epsilon + \beta_k)^2}, \quad (3.10)$$

where ϵ is a small positive number (taken to be 10^{-6} in all our examples) to avoid division by zero. Normalizing the α_k 's gives the WENO weights

$$\omega_k = \frac{\alpha_k}{\sum_{s=0}^{r-1} \alpha_s}. \quad (3.11)$$

Since the interpolation given by

$$q_{i+1/2}^- = \sum_{k=0}^{r-1} \omega_k q_{i+1/2}^{(k)} \quad (3.12)$$

is no longer a linear function of the q_i 's, the weights ω_k are called *nonlinear weights* in the WENO literature.

To illustrate the algorithm just described, let's look at the example with $r = 3$. In this case, the big stencil is

$$S^- = \{x_{i-2}, x_{i-1}, x_i, x_{i+1}, x_{i+2}\} \quad (3.13)$$

and the substencils are

$$S_0 = \{x_{i-2}, x_{i-1}, x_i\}, \quad S_1 = \{x_{i-1}, x_i, x_{i+1}\}, \quad S_2 = \{x_i, x_{i+1}, x_{i+2}\}. \quad (3.14)$$

Equations (3.3) and (3.4) becomes

$$q_{i+1/2}^- = \frac{3}{128}q_{i-2} - \frac{5}{32}q_{i-1} + \frac{45}{64}q_i + \frac{15}{32}q_{i+1} - \frac{5}{128}q_{i+2} \quad (3.15)$$

and

$$\begin{aligned} q_{i+1/2}^{(0)} &= \frac{3}{8}q_{i-2} - \frac{5}{4}q_{i-1} + \frac{15}{8}q_i, \\ q_{i+1/2}^{(1)} &= -\frac{1}{8}q_{i-1} + \frac{3}{4}q_i + \frac{3}{8}q_{i+1}, \\ q_{i+1/2}^{(2)} &= \frac{3}{8}q_i + \frac{3}{4}q_{i+1} - \frac{1}{8}q_{i+2}. \end{aligned} \quad (3.16)$$

From Equations (3.5), (3.15), and (3.16), we can obtain

$$d_0 = \frac{1}{16}, \quad d_1 = \frac{5}{8}, \quad d_2 = \frac{5}{16}. \quad (3.17)$$

The smoothness indicators (3.9) become

$$\begin{aligned} \beta_0 &= \frac{13}{12}(q_{i-2} - 2q_{i-1} + q_i)^2 + \frac{1}{4}(q_{i-2} - 4q_{i-1} + 3q_i)^2, \\ \beta_1 &= \frac{13}{12}(q_{i-1} - 2q_i + q_{i+1})^2 + \frac{1}{4}(q_{i-1} - q_{i+1})^2, \\ \beta_2 &= \frac{13}{12}(q_i - 2q_{i+1} + q_{i+2})^2 + \frac{1}{4}(3q_i - 4q_{i+1} + q_{i+2})^2. \end{aligned} \quad (3.18)$$

Thus, the approximation $q_{i+1/2}^-$ given by (3.12) will satisfy $q_{i+1/2}^- = q(x_{i+1/2}) + \mathcal{O}(\Delta x^5)$ when q is smooth on S^- , and will, in the case when S^- contains a discontinuity, be effectively chosen to be the interpolation obtained from the substencils not containing the discontinuity.

This completes the description of the WENO interpolation procedure to compute $q_{i+1/2}^-$. The approximation to $q(x_{i+1/2})$ from the other side, $q_{i+1/2}^+$, is computed from the stencil $S^+ = \{x_{i-r+2}, \dots, x_{i+r}\}$. The interpolation procedure is similar and the formulas can be obtained from the ones for $q_{i+1/2}^-$ by exploiting the mirror-symmetry between the stencils S^- and S^+ .

3.2 WENO reconstruction

The WENO reconstruction solves the problem of computing derivatives. Given a function $q(x)$, we can define a sliding function h by the implicit formula

$$q(x) = \frac{1}{\Delta x} \int_{x-\Delta x/2}^{x+\Delta x/2} h(\xi) d\xi. \quad (3.19)$$

The Fundamental Theorem of Calculus implies

$$q'(x) = \frac{1}{\Delta x} \left(h \left(x + \frac{\Delta x}{2} \right) - h \left(x - \frac{\Delta x}{2} \right) \right). \quad (3.20)$$

Now suppose we know the values of q on a uniform mesh $x_i = i\Delta x$. This is equivalent to knowing the values of the primitive function H of h defined by

$$H(x) = \int_{x_{-1/2}}^x h(\xi) d\xi, \quad (3.21)$$

where $x_{-1/2}$ is any fixed number. We thus can interpolate H and obtain an (weighted) essentially non-oscillatory interpolant polynomial by the WENO interpolation procedure described in Section 3.1, and take its derivative to get $h(x_{i+1/2})$. The value of $q'(x_i)$ can

then be computed from Equation 3.20. For stencils of $m = 2r - 1$ points, the error in $h(x_{i+1/2})$ thus obtained is of $\mathcal{O}(\Delta x^m)$, and so is the error in $q'(x_i)$, due to cancellations in the leading error terms.

In the case when $r = 3$, the big stencil S^- and its substencils were given in (3.13) and (3.14). The values h reconstructed from the substencils are

$$\begin{aligned} h_{i+1/2}^{(0)} &= \frac{1}{3}q_{i-2} - \frac{7}{6}q_{i-1} + \frac{11}{6}q_i, \\ h_{i+1/2}^{(1)} &= -\frac{1}{6}q_{i-1} + \frac{5}{6}q_i + \frac{1}{3}q_{i+1}, \\ h_{i+1/2}^{(2)} &= \frac{1}{3}q_i + \frac{5}{6}q_{i+1} - \frac{1}{6}q_{i+2}. \end{aligned} \tag{3.22}$$

The linear weights are

$$d_0 = \frac{1}{10}, \quad d_1 = \frac{3}{5}, \quad d_2 = \frac{3}{10}. \tag{3.23}$$

The smoothness indicators β_k 's are the same as in (3.18). From here, we can then compute the nonlinear weights ω_k 's and take the combination of the $h_{i+1/2}^k$'s using these weights to obtain $h_{i+1/2}$. For future reference, we shall let $\Phi_{\text{WENO5}}(q_{i-2}, q_{i-1}, q_i, q_{i+1}, q_{i+2})$ be the value of $h_{i+1/2}$ so obtained.

Chapter 4

A high-order positivity-preserving single-stage single-step method for the ideal magnetohydrodynamic equation

In this chapter, we describe our first scheme, a high-order positivity-preserving single-stage single-step scheme for the ideal MHD equations. In Section 4.1, we describe the unstaggered constrained transport framework we used a vector potential to control the divergence error of the magnetic field. In Section 4.2, we review the Taylor-discretization PIF-WENO method, which is a single-stage method for solving hyperbolic conservation laws. In Section 4.3, we describe how we solve the evolution equation of the vector potential. In Section 4.4, we describe the positivity preservation limiter we used. Finally, in Section 4.5, we present our numerical results.

The contents of this chapter is published in [19].

4.1 A constrained transport framework

In this section we review the unstaggered constrained transport framework proposed in [71]. This framework makes use of the fact that because the magnetic field \mathbf{B} is divergence-free,

it admits a vector potential \mathbf{A} that satisfies

$$\mathbf{B} = \nabla \times \mathbf{A}. \quad (4.1)$$

It is therefore possible to maintain, at the discrete level, the divergence-free property of \mathbf{B} by evolving \mathbf{A} alongside the conserved quantities, and correcting \mathbf{B} to be the curl of \mathbf{A} .

The evolution equation for the magnetic potential can be derived by starting with Maxwell's equations. That is, if we start with Faraday's law (instead of starting with the ideal MHD equations), we have

$$\partial_t \mathbf{B} = -\nabla \times \mathbf{E}. \quad (4.2)$$

Next, we approximate the electric field by Ohm's law for a perfect conductor

$$\mathbf{E} = \mathbf{B} \times \mathbf{u}, \quad (4.3)$$

which yields the induction equation used for ideal MHD:

$$\partial_t \mathbf{B} + \nabla \times (\mathbf{B} \times \mathbf{u}) = 0. \quad (4.4)$$

(After applying some appropriate vector identities, Eqn. (4.4) can be written in a conservative form.) By substituting (4.1) into (4.4), we obtain

$$\nabla \times (\partial_t \mathbf{A} + (\nabla \times \mathbf{A}) \times \mathbf{u}) = 0. \quad (4.5)$$

This implies there is a scalar function ψ such that

$$\partial_t \mathbf{A} + (\nabla \times \mathbf{A}) \times \mathbf{u} = -\nabla \psi. \quad (4.6)$$

Different choices of ψ in (4.6) correspond to different gauge conditions. It is noted in [43] that the Weyl gauge, which sets $\psi \equiv 0$, leads to stable numerical solutions. With the Weyl gauge, the evolution equation for magnetic potential (4.6) becomes

$$\partial_t \mathbf{A} + (\nabla \times \mathbf{A}) \times \mathbf{u} = 0. \quad (4.7)$$

In the constrained transport framework, both the conserved quantities $\mathbf{q} := (\rho, \rho \mathbf{u}, \mathcal{E}, \mathbf{B})$ and the magnetic potential \mathbf{A} are evolved. The time step from t^n to t^{n+1} proceeds as follows:

StepCT 1 Discretize (2.1) and update the conserved quantities

$$(\rho^n, \rho \mathbf{u}^n, \mathcal{E}^n, \mathbf{B}^n) \rightsquigarrow (\rho^{n+1}, \rho \mathbf{u}^{n+1}, \mathcal{E}^*, \mathbf{B}^*), \quad (4.8)$$

where \mathcal{E}^* and \mathbf{B}^* are subject to corrections described in Steps 3 and 4 below.

StepCT 2 Discretize (4.7) and update the magnetic potential: $\mathbf{A}^n \rightsquigarrow \mathbf{A}^{n+1}$.

StepCT 3 Correct \mathbf{B} to be the curl of \mathbf{A} through

$$\mathbf{B}^{n+1} = \nabla \times \mathbf{A}^{n+1}. \quad (4.9)$$

Note that this step modifies the pressure.

StepCT 4 Modify the total energy so the pressure remains unchanged (see below).

In the current chapter, the discretization we use for (4.8) is the Taylor-discretization of the PIF-WENO method [20]. This method is a single-stage single-step method for systems of hyperbolic conservation laws. We give a brief review of this method in Section 4.2.

It is noted in [43] that Equation (4.7) is a weakly hyperbolic system that must be treated carefully in order to avoid numerical instabilities. Along the lines of our previous work in [23], we use a discretization that is inspired by numerical schemes for Hamilton-Jacobi equations, in order to be able to define non-oscillatory derivatives of the magnetic field. We present this discretization in Section 4.3.

For certain problems, such as those involving low- β plasma, negative density or pressure occur in numerical simulations, even when constrained transport is present. This requires the use of a positivity-preserving limiter [22, 73, 93]. This limiter preserves the positivity of density and pressure by modifying the numerical flux that evolves the conserved variables. We describe this limiter in detail in Section 4.4. When this limiter is used, we also apply the following fix to the pressure in **StepCT 4** by modifying the total energy through

$$\mathcal{E}^{n+1} = \mathcal{E}^* + \frac{1}{2}(\|\mathbf{B}^{n+1}\|^2 - \|\mathbf{B}^*\|^2). \quad (4.10)$$

This energy “correction” keeps the pressure the same as before the magnetic field correction in (4.9). While this clearly has the disadvantage of violating the conservation of energy, it is nonetheless needed in order to preserve the positivity of pressure (otherwise the modifications made to the magnetic field to obtain a divergence free property could potentially cause the pressure to become negative). This technique is explored in [8, 22, 90]. In the results presented in the current work, we use the energy correction (4.10) if and only if the positivity-preserving limiter is turned on.

4.2 The Taylor-discretization PIF-WENO method

We now briefly review the Taylor-discretization Picard integral formulation weighted essentially non-oscillatory (PIF-WENO) method [20]. This method applies to generic hyperbolic conservation laws in arbitrary dimensions, of which the ideal MHD equation is an example.

For the purpose of illustration, we present the method here for a 2D system. In 2D, a hyperbolic conservation law takes the form

$$\partial_t \mathbf{q} + \partial_x \mathbf{f}(\mathbf{q}) + \partial_y \mathbf{g}(\mathbf{q}) = 0, \quad (4.11)$$

where $\mathbf{q}(t, x, y) : \mathbb{R}^+ \times \mathbb{R}^2 \rightarrow \mathbb{R}^m$ is the vector of m conserved variables, and $\mathbf{f}, \mathbf{g} : \mathbb{R}^m \rightarrow \mathbb{R}^m$ are the two components of the flux function. Formally integrating (4.11) in time from t^n to t^{n+1} , one arrives at the *Picard integral formulation* of (4.11) given by

$$\mathbf{q}^{n+1} = \mathbf{q}^n - \Delta t \partial_x \mathbf{F}^n(x, y) - \Delta t \partial_y \mathbf{G}^n(x, y), \quad (4.12)$$

where the *time-averaged fluxes* \mathbf{F} and \mathbf{G} are defined as

$$\mathbf{F}^n(x, y) = \frac{1}{\Delta t} \int_{t^n}^{t^{n+1}} \mathbf{f}(\mathbf{q}(t, x, y)) dt, \quad \text{and} \quad \mathbf{G}^n(x, y) = \frac{1}{\Delta t} \int_{t^n}^{t^{n+1}} \mathbf{g}(\mathbf{q}(t, x, y)) dt. \quad (4.13)$$

Given a domain $\Omega = [a_x, b_x] \times [a_y, b_y]$, the point-wise approximations $\mathbf{q}_{i,j}^n \approx \mathbf{q}(t^n, x_i, y_j)$ are placed at

$$x_i = a_x + \left(i - \frac{1}{2}\right) \Delta x, \quad \Delta x = \frac{b_x - a_x}{m_x}, \quad i \in \{1, \dots, m_x\}, \quad (4.14)$$

$$y_i = a_y + \left(i - \frac{1}{2}\right) \Delta y, \quad \Delta y = \frac{b_y - a_y}{m_y}, \quad y \in \{1, \dots, m_y\}, \quad (4.15)$$

and time $t = t^n$, where m_x and m_y are positive integers. The PIF-WENO scheme solves (4.11) by setting

$$\mathbf{q}_{i,j}^{n+1} = \mathbf{q}_{i,j}^n - \frac{\Delta t}{\Delta x} \left(\hat{\mathbf{F}}_{i+1/2,j}^n - \hat{\mathbf{F}}_{i-1/2,j}^n \right) - \frac{\Delta t}{\Delta y} \left(\hat{\mathbf{G}}_{i,j+1/2}^n - \hat{\mathbf{G}}_{i,j-1/2}^n \right), \quad (4.16)$$

where $\hat{\mathbf{F}}_{i\pm 1/2,j}$ and $\hat{\mathbf{G}}_{i,j\pm 1/2}$ are obtained by applying the classical WENO reconstruction to the time-averaged fluxes $\mathbf{F}_{i,j}^n$ and $\mathbf{G}_{i,j}^n$ instead of to the “frozen-in-time” fluxes, as is traditional in a method of lines (MOL) formulation. Here, $\mathbf{F}_{i,j}^n$ and $\mathbf{G}_{i,j}^n$ are approximated using a third-order Taylor expansion in time, followed by an application of Cauchy-Kovalevskaya procedure to replace the temporal derivatives with spatial derivatives. The resulting scheme on the conserved quantities is third-order accurate in time. We omit the details here and refer the reader to [20]. Extensions to three dimensions follow by including a third component for the flux function.

4.3 The evolution of the magnetic potential equation

Recall that the evolution equation for the magnetic potential is defined in (4.7). If we expand the curl and cross-product operator, we see that \mathbf{A} satisfies

$$\partial_t \mathbf{A} + N^x \partial_x \mathbf{A} + N^y \partial_y \mathbf{A} + N^z \partial_z \mathbf{A} = 0, \quad (4.17)$$

where

$$N^x = \begin{bmatrix} 0 & -u^y & -u^z \\ 0 & u^x & 0 \\ 0 & 0 & u^x \end{bmatrix}, \quad N^y = \begin{bmatrix} u^y & 0 & 0 \\ -u^x & 0 & -u^z \\ 0 & 0 & u^y \end{bmatrix}, \quad N^z = \begin{bmatrix} u^z & 0 & 0 \\ 0 & u^z & 0 \\ -u^x & -u^y & 0 \end{bmatrix} \quad (4.18)$$

are matrices defined by components of the velocity field $\mathbf{u} = (u^x, u^y, u^z)$. The system (4.17)–(4.18) has the following properties that we take into account when making a discretization:

1. This system is weakly hyperbolic. This means that all of the eigenvalues of (4.17) are real, but in contrast to being strictly hyperbolic, the system is not necessarily diagonalizable. While this weak hyperbolicity is an artifact of how the magnetic potential is evolved, it must be treated carefully to avoid creating numerical instabilities [43];
2. Each equation of this system can be viewed as a Hamilton-Jacobi equation with a source term [23].

One consequence of this second observation is that we can use Hamilton-Jacobi technology in order to define magnetic fields that have non-oscillatory derivatives. That is, a single derivative of \mathbf{B} is a second derivative of \mathbf{A} , in which case care need be taken in order to retain a non-oscillatory property.

In the next two subsections, we will describe how we discretize the system (4.17)–(4.18), with these two properties in mind. Before we do that, we make several remarks. The first is that in the discretization, \mathbf{A} sits on the same mesh as the conserved quantities, hence the name “*unstaggered* constrained transport”. The second is that the curl operator $\nabla \times$ is discretized in the same way as in [23], which defines a divergence free magnetic field (at the discrete level). A final remark is that the discretization we present here is third-order

accurate in time, which is in accordance with the discretization we use for the conserved quantities.

4.3.1 The 2D magnetic potential equation

We begin with the two-dimensional case, where the conserved quantities and the magnetic potential do not depend on z . In this case, the divergence-free condition is

$$\nabla \cdot \mathbf{B} = \partial_x B^x + \partial_y B^y = 0. \quad (4.19)$$

Thus B^z has no impact on the divergence of \mathbf{B} . It therefore suffices to correct only the first two components of the magnetic field. A computationally cost-efficient way of doing this is to discard the first two components of the magnetic potential, evolve only the third component according to the evolution equation

$$\partial_t A^z + u^x \partial_x A^z + u^y \partial_y A^z = 0, \quad (4.20)$$

and for the magnetic field correction, only correct B^x and B^y through

$$B^x = \partial_y A^z \quad \text{and} \quad B^y = -\partial_x A^z. \quad (4.21)$$

This is equivalent to imposing $\partial_z A^x = 0$ and $\partial_z A^y = 0$ on the system (4.17)–(4.18), and skipping B^z in the magnetic field correction in Eqn. (4.9).

Equation (4.20) has the favorable property of being *strongly hyperbolic* [71], in contrast to the weak hyperbolicity in the 3D case. This equation is also a Hamilton-Jacobi equation,

with Hamilton principal function A^z , and Hamiltonian

$$H(t, x, y, \partial_x A^z, \partial_y A^z) = u^x(t, x, y) \partial_x A^z + u^y(t, x, y) \partial_y A^z. \quad (4.22)$$

It is therefore possible to discretize Equation (4.20) using a numerical scheme for Hamilton-Jacobi equations [23]. In line with the single-stage single-step theme of the proposed scheme, we use a method that is inspired by the Lax-Wendroff WENO schemes for Hamilton-Jacobi equations from [66].

A Lax-Wendroff WENO scheme for Hamilton-Jacobi equations is based on the Taylor expansion in time of the Hamilton principal function. In order to retain third-order accuracy in time, we require a total of three time derivatives of $A_{i,j}^z$:

$$A_{i,j}^{z\ n+1} = A_{i,j}^{z\ n} + \Delta t \partial_t A_{i,j}^{z\ n} + \frac{\Delta t^2}{2!} \partial_t^2 A_{i,j}^{z\ n} + \frac{\Delta t^3}{3!} \partial_t^3 A_{i,j}^{z\ n}, \quad (4.23)$$

where the temporal derivatives on the right-hand-side are computed in the following manner:

1. The first derivative is approximated by the Lax-Friedrichs type numerical Hamiltonian, with high-order reconstruction of $\partial_x A^z$ and $\partial_y A^z$ [65]. Namely, we define

$$\begin{aligned} \partial_t A_{i,j}^z &:= -\hat{H}(\partial_x A_{i,j}^{z-}, \partial_x A_{i,j}^{z+}, \partial_y A_{i,j}^{z-}, \partial_y A_{i,j}^{z+}) \\ &= -u_{i,j}^x \left(\frac{\partial_x A_{i,j}^{z-} + \partial_x A_{i,j}^{z+}}{2} \right) - u_{i,j}^y \left(\frac{\partial_y A_{i,j}^{z-} + \partial_y A_{i,j}^{z+}}{2} \right) \\ &\quad + \alpha^x \left(\frac{\partial_x A_{i,j}^{z+} - \partial_x A_{i,j}^{z-}}{2} \right) + \alpha^y \left(\frac{\partial_y A_{i,j}^{z+} - \partial_y A_{i,j}^{z-}}{2} \right), \end{aligned} \quad (4.24)$$

where

$$\alpha^x = \max_{i,j} |u_{i,j}^x| \quad \text{and} \quad \alpha^y = \max_{i,j} |u_{i,j}^y| \quad (4.25)$$

are the maximum velocities taken over the entire grid, (i.e., the numerical flux is the global Lax-Friedrichs flux), and $\partial_x A_{i,j}^{z\pm}$, $\partial_y A_{i,j}^{z\pm}$ are defined by WENO reconstructions through

$$\begin{aligned}
\partial_x A_{i,j}^{z-} &= \Phi_{\text{WENO5}} \left(\frac{\Delta_x^+ A_{i-3,j}^z}{\Delta x}, \frac{\Delta_x^+ A_{i-2,j}^z}{\Delta x}, \frac{\Delta_x^+ A_{i-1,j}^z}{\Delta x}, \frac{\Delta_x^+ A_{i,j}^z}{\Delta x}, \frac{\Delta_x^+ A_{i+1,j}^z}{\Delta x} \right), \\
\partial_x A_{i,j}^{z+} &= \Phi_{\text{WENO5}} \left(\frac{\Delta_x^+ A_{i+2,j}^z}{\Delta x}, \frac{\Delta_x^+ A_{i+1,j}^z}{\Delta x}, \frac{\Delta_x^+ A_{i,j}^z}{\Delta x}, \frac{\Delta_x^+ A_{i-1,j}^z}{\Delta x}, \frac{\Delta_x^+ A_{i-2,j}^z}{\Delta x} \right), \\
\partial_y A_{i,j}^{z-} &= \Phi_{\text{WENO5}} \left(\frac{\Delta_y^+ A_{i,j-3}^z}{\Delta y}, \frac{\Delta_y^+ A_{i,j-2}^z}{\Delta y}, \frac{\Delta_y^+ A_{i,j-1}^z}{\Delta y}, \frac{\Delta_y^+ A_{i,j}^z}{\Delta y}, \frac{\Delta_y^+ A_{i,j+1}^z}{\Delta y} \right), \\
\partial_y A_{i,j}^{z+} &= \Phi_{\text{WENO5}} \left(\frac{\Delta_y^+ A_{i,j+2}^z}{\Delta y}, \frac{\Delta_y^+ A_{i,j+1}^z}{\Delta y}, \frac{\Delta_y^+ A_{i,j}^z}{\Delta y}, \frac{\Delta_y^+ A_{i,j-1}^z}{\Delta y}, \frac{\Delta_y^+ A_{i,j-2}^z}{\Delta y} \right),
\end{aligned} \tag{4.26}$$

and $\Delta_x^+ A_{i,j}^z := A_{i+1,j}^z - A_{i,j}^z$ and $\Delta_y^+ A_{i,j}^z := A_{i,j+1}^z - A_{i,j}^z$. The function Φ_{WENO5} is the classical fifth-order WENO reconstruction whose formula we gave in Section 3.2. Note that this difference operator is designed for Hamilton-Jacobi problems, and does not produce the typical flux difference form that most hyperbolic solvers produce.

2. The higher derivatives $\partial_t^2 A^z$ and $\partial_t^3 A^z$ are converted into spatial derivatives by way of the Cauchy-Kovalevskaya procedure, and the resulting spatial derivatives are approximated using central differences. For example, $\partial_t^2 A^z$ is converted into spatial derivatives

by

$$\begin{aligned}
\partial_t^2 A^z &= \partial_t(\partial_t A^z) \\
&= \partial_t(-u^x \partial_x A^z - u^y \partial_y A^z) \\
&= -\partial_t u^x \partial_x A^z - u^x \partial_t \partial_x A^z - \partial_t u^y \partial_y A^z - u^y \partial_t \partial_y A^z \\
&= -\partial_t u^x \partial_x A^z - u^x \partial_x(\partial_t A^z) - \partial_t u^y \partial_y A^z - u^y \partial_y(\partial_t A^z) \tag{4.27} \\
&= -\partial_t u^x \partial_x A^z - u^x \partial_x(-u^x \partial_x A^z - u^y \partial_y A^z) - \partial_t u^y \partial_y A^z \\
&\quad - u^y \partial_y(-u^x \partial_x A^z - u^y \partial_y A^z) \\
&= -\partial_t u^x \partial_x A^z - u^x(-\partial_x u^x \partial_x A^z - u^x \partial_x^2 A^z - \partial_x u^y \partial_y A^z - u^y \partial_x \partial_y A^z) \\
&\quad - \partial_t u^y \partial_y A^z - u^y(-\partial_y u^x \partial_x A^z - u^x \partial_x \partial_y A^z - \partial_y u^y \partial_y A^z - u^y \partial_y^2 A^z),
\end{aligned}$$

where

$$\partial_t u^x = \partial_t \left(\frac{\rho u^x}{\rho} \right) = \frac{\partial_t(\rho u^x)\rho - (\rho u^x)\partial_t \rho}{\rho^2}, \tag{4.28}$$

and

$$\partial_t u^y = \partial_t \left(\frac{\rho u^y}{\rho} \right) = \frac{\partial_t(\rho u^y)\rho - (\rho u^y)\partial_t \rho}{\rho^2}, \tag{4.29}$$

with $\partial_t(\rho u^x)$, $\partial_t(\rho u^y)$, and $\partial_t \rho$ converted into spatial derivatives by way of (2.1). Note that we do not find it necessary to use a FD WENO discretization for ρ_t . There are a total of 49 distinct spatial derivatives that need to be approximated in (4.27)–(4.29). Similar expressions exist for $\partial_t^3 A^z$. These are done by using the central differencing

formulae

$$\partial_x U_{i,j} = \frac{-U_{i-1,j} + U_{i+1,j}}{2\Delta x}, \quad (4.30)$$

$$\partial_x^2 U_{i,j} = \frac{U_{i-1,j} - 2U_{i,j} + U_{i+1,j}}{\Delta x^2}, \quad (4.31)$$

$$\partial_x \partial_y U_{i,j} = \frac{U_{i-1,j-1} - U_{i-1,j+1} - U_{i+1,j-1} + U_{i+1,j+1}}{4\Delta x \Delta y}, \quad (4.32)$$

$$\partial_x^3 U_{i,j} = \frac{-U_{i-2,j} + 2U_{i-1,j} - 2U_{i+1,j} + U_{i+2,j}}{2\Delta x^3}, \quad (4.33)$$

$$\partial_x^2 \partial_y U_{i,j} = \frac{2U_{i,j-1} - 2U_{i,j+1} - U_{i-1,j-1} + U_{i-1,j+1} - U_{i+1,j-1} + U_{i+1,j+1}}{2\Delta x^2 \Delta y}, \quad (4.34)$$

and similar ones for the y -, yy -, xyy - and yyy -derivatives, where U is any of ρ , ρu^x , ρu^y , ρu^z , \mathcal{E} , B^x , B^y , B^z , or A^z .

Remark 4.1. In the current work, the magnetic field correction in Eqn. (4.21) is discretized to fourth-order accuracy with central difference formulas. For example, we define the y -derivative of A^z to be

$$B_{i,j}^x = \partial_y A^z \approx \frac{A_{i,j-2}^z - 8A_{i,j-1}^z + 8A_{i,j+1}^z - A_{i,j+2}^z}{12\Delta y}, \quad (4.35)$$

and others similarly. Therefore in the discretization of equations (2.1) and (4.17), we aim for fourth-order accuracy in space. For the fluid equations in (2.1), we use the fifth-order accurate spatial discretization defined in [20]. In the case of (4.17), Eqn. (4.23) is a fifth-order approximation to $\partial_t A^z(t^n, x_i, y_j)$ since the reconstructions (4.26) give, for example,

$$\partial_x A_{i,j}^{z+} = \partial_x A^z(t^n, x_i, y_j) + \mathcal{O}(\Delta x^5), \quad (4.36)$$

whereas Eqns. (4.30)–(4.34) are chosen so that Eqn. (4.23) is fourth-order accurate in space

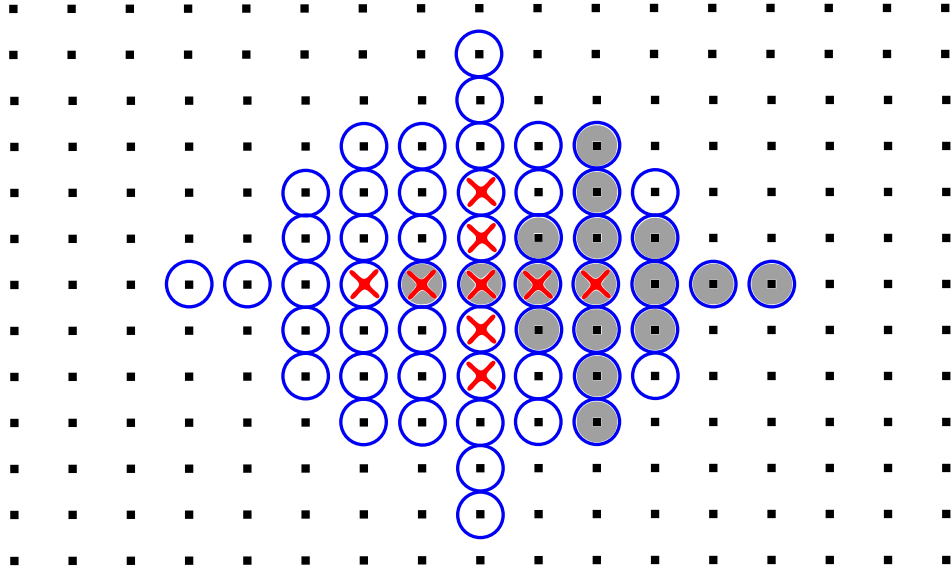


Figure 4.1: Stencil needed for magnetic potential. The values of A^z at each “ \times ” (save the centermost value) is needed to correct the value of \mathbf{B} at the center. The shaded points are needed in Eqns. (4.26) and (4.30)–(4.34) to compute the value of A^z at the rightmost “ \times ” point. Note that this stencil is contained in the stencil shown in [20], Fig. 2.

when $\Delta t = \mathcal{O}(\Delta x)$. This fourth-order accuracy is verified in our numerical results.

Remark 4.2. In each dimension, the stencil needed to compute \mathbf{B} from \mathbf{A} is 5 points wide, and an inspection of (4.26) and (4.30)–(4.34) indicates that the stencil needed to compute \mathbf{A} is 7 points wide. This results in a stencil that is 11 points wide in each dimension. A more careful analysis of (4.30)–(4.34) shows that this stencil is indeed contained within the stencil given by the PIF-WENO discretization of Eqn. (4.11) (which is sketched in Fig. 2 of [20]). We present a sketch of the stencil required to discretize the magnetic potential in Fig. 4.1.

We note that our discretization differs from that found in [66] in that we do not store any lower temporal derivatives for use in computation of higher temporal derivatives. That is, the method proposed in [66] stores the values of $\partial_t A^z$ computed in Equation (4.27), and makes use of the central differences of $\partial_t A^z$. Although that approach saves the trouble of

expanding Eqn. (4.34), our approach has the following advantages that are in line with our goals:

Minimal storage. Our approach avoids the necessity of storing the lower temporal derivatives (at the expense of a more complicated code). Note here that it would be not only $\partial_t A^z$ and $\partial_{tt} A^z$, but also the temporal derivatives of ρ , ρu^x , ρu^y , ρu^z , \mathcal{E} , B^x , B^y , and B^z that must be stored if the approach in [66] were to be taken. This would lead to a formidable amount of temporary storage when applied to the magnetic potential evolution equation in 3D;

Smaller stencils. The method in [66] would require a stencil that is 15 points wide in each dimension in order to provide the necessary \mathbf{A} values for correcting the magnetic field. Our method only needs a stencil that is 11 points wide. This somewhat simplifies the future work of embedding the scheme into an AMR framework, but the biggest improvement is the reduction of temporary storage.

4.3.2 The 3D magnetic potential equation

The 3D magnetic potential equation (4.17)–(4.18) is weakly hyperbolic, and therefore special attention is needed. This can be treated by introducing artificial resistivity terms into the system [23, 43, 44]. To illustrate the technique, we consider the first row of the system which is

$$\partial_t A^x - u^y \partial_x A^y - u^z \partial_x A^z + u^y \partial_y A^x + u^z \partial_z A^x = 0. \quad (4.37)$$

A discretization of $\partial_t A^x$ in the spirit of (4.24) would give the following numerically problematic formulation

$$\begin{aligned}
\partial_t A_{i,j,k}^x &= -u_{i,j,k}^y \left(\frac{\partial_y A_{i,j,k}^{x-} + \partial_y A_{i,j,k}^{x+}}{2} \right) - u_{i,j,k}^z \left(\frac{\partial_z A_{i,j,k}^{x-} + \partial_z A_{i,j,k}^{x+}}{2} \right) \\
&+ \alpha^y \left(\frac{\partial_y A_{i,j,k}^{x+} - \partial_y A_{i,j,k}^{x-}}{2} \right) + \alpha^z \left(\frac{\partial_z A_{i,j,k}^{x+} - \partial_z A_{i,j,k}^{x-}}{2} \right) \\
&+ u_{i,j,k}^y \left(\frac{\partial_x A_{i,j,k}^{y-} + \partial_x A_{i,j,k}^{y+}}{2} \right) + u_{i,j,k}^z \left(\frac{\partial_x A_{i,j,k}^{z-} + \partial_x A_{i,j,k}^{z+}}{2} \right)
\end{aligned} \tag{4.38}$$

where

$$\alpha^y = \max_{i,j,k} |u_{i,j,k}^y| \quad \text{and} \quad \alpha^z = \max_{i,j,k} |u_{i,j,k}^z|, \tag{4.39}$$

and $\partial_y A_{i,j,k}^{x-}$, $\partial_y A_{i,j,k}^{x+}$, $\partial_z A_{i,j,k}^{x-}$, $\partial_z A_{i,j,k}^{x+}$, $\partial_x A_{i,j,k}^{2-}$, $\partial_x A_{i,j,k}^{2+}$, $\partial_x A_{i,j,k}^{3-}$, and $\partial_x A_{i,j,k}^{3+}$ are reconstructed in a manner similar to (4.26). The problem with (4.38) is that this formulation lacks numerical resistivity in the x -direction.

As is the case in [23], we find that the addition of an artificial resistivity term to (4.38) yields satisfactory numerical results. With the artificial resistivity term, the evolution equation (4.37) becomes

$$\partial_t A^x - u^y \partial_x A^y - u^z \partial_x A^z + u^y \partial_y A^x + u^z \partial_z A^x = \epsilon^x \partial_x^2 A^x, \tag{4.40}$$

where ϵ^x ideally satisfies

$$\epsilon^x = \mathcal{O}(\Delta x^6), \text{ when } \partial_x A^x \text{ is smooth,} \tag{4.41}$$

and

$$\epsilon^x = \mathcal{O}(\Delta x), \text{ when } \partial_x A^x \text{ is non-smooth.} \quad (4.42)$$

We define the artificial resistivity ϵ^x in the following manner. Define a smoothness indicator γ^x for $\partial_x A^x$ as follows:

$$\gamma_{i,j,k}^x = \left| \frac{a^-}{a^- + a^+} - \frac{1}{2} \right|, \quad (4.43)$$

where

$$a^- = \left(\epsilon + (\Delta x \partial_x A_{i,j,k}^{x-})^2 \right)^{-2} \quad \text{and} \quad a^+ = \left(\epsilon + (\Delta x \partial_x A_{i,j,k}^{x+})^2 \right)^{-2}. \quad (4.44)$$

Here, ϵ is a small positive number introduced to avoid dividing by a number close to 0 when the potential is smooth ($\epsilon = 10^{-8}$ in all our numerical simulations). Now we define ϵ^x to be

$$\epsilon^x = 2\nu\gamma^x \frac{\Delta x^2}{\Delta t}, \quad (4.45)$$

where ν is a positive constant that controls the magnitude of the artificial resistivity. For a more detailed discussion of the weak hyperbolicity and the reasoning leading up to (4.45), we refer the reader to [43, 23]. In [43], it is shown that ν has to be in the range of $[0, 0.5]$ to maintain the stability up to CFL one for their finite volume method. Through numerical experimentation, we find that ν in the vicinity of 0.01 is sufficient to control potential oscillations in the magnetic field.

We thus use the following formulation as our discretization of (4.37)

$$\begin{aligned}
\partial_t A_{i,j,k}^x = & -u_{i,j,k}^y \left(\frac{\partial_y A_{i,j,k}^{x-} + \partial_y A_{i,j,k}^{x+}}{2} \right) - u_{i,j,k}^z \left(\frac{\partial_z A_{i,j,k}^{x-} + \partial_z A_{i,j,k}^{x+}}{2} \right) \\
& + \alpha^y \left(\frac{\partial_y A_{i,j,k}^{x+} - \partial_y A_{i,j,k}^{x-}}{2} \right) + \alpha^z \left(\frac{\partial_z A_{i,j,k}^{x+} - \partial_z A_{i,j,k}^{x-}}{2} \right) \\
& + u_{i,j,k}^y \left(\frac{\partial_x A_{i,j,k}^{y-} + \partial_x A_{i,j,k}^{y+}}{2} \right) + u_{i,j,k}^z \left(\frac{\partial_x A_{i,j,k}^{z-} + \partial_x A_{i,j,k}^{z+}}{2} \right) \\
& + 2\nu\gamma_{i,j,k}^x \left(\frac{A_{i-1,j,k}^x - 2A_{i,j,k}^x + A_{i+1,j,k}^x}{\Delta t} \right). \tag{4.46}
\end{aligned}$$

The discretization of $\partial_t A^y$ and $\partial_t A^z$ are similar and we omit them for brevity.

For our Lax-Wendroff formulation, it remains to discretize the higher temporal derivatives of the components of \mathbf{A} . We find it suffices to apply the same techniques as in Section 4.3.1 for $\partial_t^2 A^z$ and $\partial_t^3 A^z$. Namely, we convert all the temporal derivatives to spatial derivatives via the Cauchy-Kovalevskaya procedure, and approximate the resulting spatial derivatives with central differences. We note that the artificial resistivity term is only added to the first temporal derivative.

4.4 Positivity preservation

The scheme presented thus far can be applied to a large class of problems. However, for problems where the plasma density or pressure are near zero, Gibb's phenomenon can cause these values to become negative, and hence the numerical simulation will instantly fail. As a final ingredient to the solver, we introduce an additional option for retaining positivity of the solution. Given the lack of number of degrees of freedom, this limiter comes at the expense of energy conservation, but these regions only occur in small areas where the density

or pressure become negative.

A positivity-preserving scheme can be constructed by modifying the fluxes $\hat{\mathbf{F}}$ and $\hat{\mathbf{G}}$ in (4.16). Let $\hat{\mathbf{f}}_{i+1/2,j}$ and $\hat{\mathbf{g}}_{i,j+1/2}$ be the (global) Lax-Friedrichs fluxes defined by

$$\begin{aligned}\hat{\mathbf{f}}_{i+1/2,j} &= \frac{1}{2}(\mathbf{f}(\mathbf{q}_{i+1,j}^n) + \mathbf{f}(\mathbf{q}_{i,j}^n) - \alpha^x(\mathbf{q}_{i+1,j}^n - \mathbf{q}_{i,j}^n)), \\ \hat{\mathbf{g}}_{i,j+1/2} &= \frac{1}{2}(\mathbf{g}(\mathbf{q}_{i,j+1}^n) + \mathbf{g}(\mathbf{q}_{i,j}^n) - \alpha^y(\mathbf{q}_{i,j+1}^n - \mathbf{q}_{i,j}^n)),\end{aligned}\tag{4.47}$$

where α^x and α^y are the maximal wave speeds in the x and y directions, respectively. This type of formulation is commonly referred to as Lax-Friedrich's flux splitting in the ENO/WENO literature [78, 79, 50].

The update of \mathbf{q} using these Lax-Friedrichs fluxes is

$$\mathbf{q}_{i,j}^{\text{LF}} = \mathbf{q}_{i,j}^n - \frac{\Delta t}{\Delta x} \left(\hat{\mathbf{f}}_{i+1/2,j}^n - \hat{\mathbf{f}}_{i-1/2,j}^n \right) - \frac{\Delta t}{\Delta y} \left(\hat{\mathbf{g}}_{i,j+1/2}^n - \hat{\mathbf{g}}_{i,j-1/2}^n \right).\tag{4.48}$$

For an 8-component state vector $\mathbf{q} = (\rho, \rho\mathbf{u}, \mathcal{E}, \mathbf{B})$, we also introduce the notation $\rho(\mathbf{q})$ and $p(\mathbf{q})$ to represent the density and the thermal pressure of \mathbf{q} . Also, let ϵ_ρ and ϵ_p be small positive numbers.

The following claim was conjectured in [18].

Claim 4.1. *If $\rho(\mathbf{q}_{i,j}^n) > \epsilon_\rho$ and $p(\mathbf{q}_{i,j}^n) > \epsilon_p$ for all i, j , and the CFL number is less than or equal to 0.5, we then have $\rho(\mathbf{q}_{i,j}^{\text{LF}}) > \epsilon_\rho$ and $p(\mathbf{q}_{i,j}^{\text{LF}}) > \epsilon_p$ for all i, j .*

Though not proven, this claim is verified in [18] using a fairly large number of random values of \mathbf{q} . Our positivity limiter assumes this claim is true. However, as is noted in [18], if a different flux can be found such that it satisfies a property similar to that of the Lax-Friedrichs fluxes stated in Claim 4.1, we can then use these different fluxes in place of $\hat{\mathbf{f}}_{i+1/2,j}$

and $\hat{\mathbf{g}}_{i,j+1/2}$ in the construction of our positivity limiter.

The modified fluxes take the form

$$\tilde{\mathbf{F}}_{i+1/2,j} = \theta_{i+1/2,j}(\hat{\mathbf{F}}_{i+1/2,j} - \hat{\mathbf{f}}_{i+1/2,j}) + \hat{\mathbf{f}}_{i+1/2,j}, \quad (4.49)$$

$$\tilde{\mathbf{G}}_{i,j+1/2} = \theta_{i,j+1/2}(\hat{\mathbf{G}}_{i,j+1/2} - \hat{\mathbf{g}}_{i,j+1/2}) + \hat{\mathbf{g}}_{i,j+1/2}, \quad (4.50)$$

where $\theta_{i+1/2,j}$ and $\theta_{i,j+1/2}$ are chosen such that

- $0 \leq \theta_{i+1/2,j} \leq 1$, $0 \leq \theta_{i,j+1/2} \leq 1$,
- the update (4.16) with $\hat{\mathbf{F}}$ and $\hat{\mathbf{G}}$ replaced by the modified fluxes $\tilde{\mathbf{F}}$ and $\tilde{\mathbf{G}}$ defined in (4.49)–(4.50) yields positive density and pressure, and
- while subject to the positivity requirement just stated, $\theta_{i+1/2,j}$ and $\theta_{i,j+1/2}$ should be as close to 1 as possible, so that the high-order fluxes are used in regions where violation of positivity is unlikely to happen.

Following [22], we choose each θ in a series of two steps:

Step- θ (i) For each i, j , find “large” candidate limiting parameters $\Lambda_{L,i,j}$, $\Lambda_{R,i,j}$, $\Lambda_{D,i,j}$, and $\Lambda_{U,i,j} \in [0, 1]$ such that for all

$$(\theta_L, \theta_R, \theta_D, \theta_U) \in [0, \Lambda_{L,i,j}] \times [0, \Lambda_{R,i,j}] \times [0, \Lambda_{D,i,j}] \times [0, \Lambda_{U,i,j}], \quad (4.51)$$

the update defined by

$$\begin{aligned}
\mathbf{q} &:= \mathbf{q}_{i,j}^n \\
&\quad - \frac{\Delta t}{\Delta x} \left((\theta_R(\hat{\mathbf{F}}_{i+1/2,j} - \hat{\mathbf{f}}_{i+1/2,j}) + \hat{\mathbf{f}}_{i+1/2,j}) \right. \\
&\quad \quad \left. - (\theta_L(\hat{\mathbf{F}}_{i-1/2,j} - \hat{\mathbf{f}}_{i-1/2,j}) + \hat{\mathbf{f}}_{i-1/2,j}) \right) \\
&\quad - \frac{\Delta t}{\Delta y} \left((\theta_U(\hat{\mathbf{G}}_{i,j+1/2} - \hat{\mathbf{g}}_{i,j+1/2}) + \hat{\mathbf{g}}_{i,j+1/2}) \right. \\
&\quad \quad \left. - (\theta_D(\hat{\mathbf{G}}_{i,j-1/2} - \hat{\mathbf{g}}_{i,j-1/2}) + \hat{\mathbf{g}}_{i,j-1/2}) \right)
\end{aligned} \tag{4.52}$$

satisfies $\rho(\mathbf{q}) > \epsilon_\rho$ and $p(\mathbf{q}) > \epsilon_p$;

Step- θ (ii) For each i, j , set

$$\theta_{i+1/2,j} := \min\{\Lambda_{R,i,j}, \Lambda_{L,i+1,j}\} \tag{4.53}$$

$$\theta_{i,j+1/2} := \min\{\Lambda_{U,i,j}, \Lambda_{D,i,j+1}\}. \tag{4.54}$$

We note that with $\mathbf{q}_{i,j}^n$, $\hat{\mathbf{F}}$, $\hat{\mathbf{f}}$, $\hat{\mathbf{G}}$, and $\hat{\mathbf{g}}$ already computed, Equation (4.52) expresses the update \mathbf{q} as an affine function of $\theta_L, \theta_R, \theta_D, \theta_U$, which, by abuse of notation, is denoted by $\mathbf{q}(\theta_L, \theta_R, \theta_D, \theta_U)$. The coefficients of the θ 's in $\mathbf{q}(\theta_L, \theta_R, \theta_D, \theta_U)$ are denoted by $\mathbf{C}_L, \mathbf{C}_R, \mathbf{C}_D$, and \mathbf{C}_U . Thus we have

$$\begin{aligned}
\mathbf{C}_L &= \frac{\Delta t}{\Delta x} (\hat{\mathbf{F}}_{i-1/2,j} - \hat{\mathbf{f}}_{i-1/2,j}), & \mathbf{C}_R &= -\frac{\Delta t}{\Delta x} (\hat{\mathbf{F}}_{i+1/2,j} - \hat{\mathbf{f}}_{i+1/2,j}), \\
\mathbf{C}_D &= \frac{\Delta t}{\Delta y} (\hat{\mathbf{G}}_{i,j-1/2} - \hat{\mathbf{g}}_{i,j-1/2}), & \mathbf{C}_U &= -\frac{\Delta t}{\Delta y} (\hat{\mathbf{G}}_{i,j+1/2} - \hat{\mathbf{g}}_{i,j+1/2}),
\end{aligned} \tag{4.55}$$

and, with (4.48) in mind, the limited solution is

$$\mathbf{q}(\theta_L, \theta_R, \theta_D, \theta_U) = \mathbf{q}_{i,j}^{\text{LF}} + \mathbf{C}_L \theta_L + \mathbf{C}_R \theta_R + \mathbf{C}_D \theta_D + \mathbf{C}_U \theta_U. \tag{4.56}$$

With this notation, **Step- θ (i)** reduces to solving the following problem for each i, j :

Problem 4.1. *Given constant real vectors $\mathbf{C}_L, \mathbf{C}_R, \mathbf{C}_D$ and \mathbf{C}_U , and constant 8-component state vector $\mathbf{q}_{i,j}^{LF}$ such that $\rho(\mathbf{q}_{i,j}^{LF}) > \epsilon_\rho$ and $p(\mathbf{q}_{i,j}^{LF}) > \epsilon_p$, find $(\Lambda_{L,i,j}, \Lambda_{R,i,j}, \Lambda_{D,i,j}, \Lambda_{U,i,j})$ in $[0, 1] \times [0, 1] \times [0, 1] \times [0, 1]$ such that for all $(\theta_L, \theta_R, \theta_D, \theta_U)$ in $[0, \Lambda_{L,i,j}] \times [0, \Lambda_{R,i,j}] \times [0, \Lambda_{D,i,j}] \times [0, \Lambda_{U,i,j}]$, the expression*

$$\mathbf{q}(\theta_L, \theta_R, \theta_D, \theta_U) = \mathbf{q}_{i,j}^{LF} + \mathbf{C}_L\theta_L + \mathbf{C}_R\theta_R + \mathbf{C}_D\theta_D + \mathbf{C}_U\theta_U \quad (4.57)$$

satisfies

$$\rho(\mathbf{q}(\theta_L, \theta_R, \theta_D, \theta_U)) > \epsilon_\rho \quad (4.58)$$

and

$$p(\mathbf{q}(\theta_L, \theta_R, \theta_D, \theta_U)) > \epsilon_p. \quad (4.59)$$

The region $[0, \Lambda_{L,i,j}] \times [0, \Lambda_{R,i,j}] \times [0, \Lambda_{D,i,j}] \times [0, \Lambda_{U,i,j}]$ should be “as big as possible”.

We note the following fact.

Claim 4.2. *The sets S_ρ and S defined by*

$$S_\rho = \{(\theta_L, \theta_R, \theta_D, \theta_U) \in [0, 1]^4 \mid \rho(\mathbf{q}(\theta_L, \theta_R, \theta_D, \theta_U)) > \epsilon_\rho\} \quad (4.60)$$

and

$$S = \{(\theta_L, \theta_R, \theta_D, \theta_U) \in [0, 1]^4 \mid \rho(\mathbf{q}(\theta_L, \theta_R, \theta_D, \theta_U)) > \epsilon_\rho \text{ and } p(\mathbf{q}(\theta_L, \theta_R, \theta_D, \theta_U)) > \epsilon_p\} \quad (4.61)$$

are both convex.

Proof. Since ρ is a linear function of \mathbf{q} and \mathbf{q} is an affine function of $(\theta_L, \theta_R, \theta_D, \theta_U)$, we see that $\rho(\mathbf{q}(\theta_L, \theta_R, \theta_D, \theta_U))$ is an affine function of $(\theta_L, \theta_R, \theta_D, \theta_U)$. Thus S_ρ is the part of $[0, 1]^4$ that lies on one side of a hyperplane. This shows S_ρ is convex.

To see the convexity of S , note that by the equation of state 2.3, the pressure p is a concave function of the components of \mathbf{q} , whenever $\rho > 0$. Combined with the fact that $\mathbf{q}(\theta_L, \theta_R, \theta_D, \theta_U)$ is an affine function of $(\theta_L, \theta_R, \theta_D, \theta_U)$, we see that $p(\mathbf{q}(\theta_L, \theta_R, \theta_D, \theta_U))$ is a concave function of $(\theta_L, \theta_R, \theta_D, \theta_U)$, if $\rho(\mathbf{q}(\theta_L, \theta_R, \theta_D, \theta_U)) > 0$. This shows the convexity of S_p . \square

Note that Problem 4.1 is not well-defined, since the notion of “big” is not defined. The algorithm we are about to describe gives a solution that is satisfactory, in the sense that this algorithm yields a positivity-preserving limiter that behaves well in our numerical tests.

We now describe this algorithm. The first step of this algorithm is to find a “big” rectangular subset $R_\rho := [0, \Lambda_L^\rho] \times [0, \Lambda_R^\rho] \times [0, \Lambda_D^\rho] \times [0, \Lambda_U^\rho]$ of S_ρ . The Λ^ρ 's are computed

by

$$\Lambda_{\mathcal{I}}^{\rho} = \begin{cases} \min \left\{ 1, \frac{\rho(\mathbf{q}_{i,j}^{\text{LF}}) - \epsilon_{\rho}}{\epsilon + \sum_{\substack{\mathcal{J}, \\ C_{\mathcal{J}}^{(1)} < 0}} |C_{\mathcal{J}}^{(1)}|} \right\} & \text{if } C_{\mathcal{I}}^{(1)} < 0, \\ 1 & \text{if } C_{\mathcal{I}}^{(1)} \geq 0, \end{cases} \quad (4.62)$$

where ϵ is a small fixed positive number (10^{-12} in all our simulations) and the subscript letters \mathcal{I} and \mathcal{J} take values in L, R, D , and U . The value $C_{\mathcal{I}}^{(1)}$ denotes the first component of the $\mathbf{C}_{\mathcal{I}}$ vector.

The second step is to shrink this rectangular subset R_{ρ} to fit into S_{ρ} . The vertices of R_{ρ} are denoted by $\mathbf{A}^{k_L, k_R, k_D, k_U}$, where $k_{\mathcal{I}} = 0$ or 1 , such that the \mathcal{I} -th component of $\mathbf{A}^{k_L, k_R, k_D, k_U}$ is

$$A_{\mathcal{I}}^{k_L, k_R, k_D, k_U} = \begin{cases} \Lambda_{\mathcal{I}}^{\rho} & \text{if } k_{\mathcal{I}} = 1, \\ 0 & \text{if } k_{\mathcal{I}} = 0. \end{cases} \quad (4.63)$$

Now for each (k_L, k_R, k_D, k_U) , shrink $\mathbf{A}^{k_L, k_R, k_D, k_U}$ to get $\mathbf{B}^{k_L, k_R, k_D, k_U}$ in the following way. If $p(\mathbf{A}^{k_L, k_R, k_D, k_U}) \geq \epsilon_p$, set $\mathbf{B}^{k_L, k_R, k_D, k_U} = \mathbf{A}^{k_L, k_R, k_D, k_U}$. Otherwise, we solve for the smallest positive r such that $p(r\mathbf{A}^{k_L, k_R, k_D, k_U}) \geq \epsilon_p$, and set $\mathbf{B}^{k_L, k_R, k_D, k_U} = r\mathbf{A}^{k_L, k_R, k_D, k_U}$. In order to solve for this value, we apply a total of 10 iterations of the bisection method. A more efficient (approximate) solver could easily replace this step (e.g., a single step of the method of false position). Note that the different vertices $\mathbf{A}^{k_L, k_R, k_D, k_U}$ are in general shrunk by different factors r . Now we set

$$\Lambda_{\mathcal{I}, i, j} = \min_{\substack{(k_L, k_R, k_U, k_D), \\ k_{\mathcal{I}}=1}} B_{\mathcal{I}}^{k_L, k_R, k_U, k_D}, \quad (4.64)$$

where the subscript \mathcal{I} indicates the \mathcal{I} -th component. Note that this is equivalent to finding a rectangular subset inside the convex polygon with vertices $\mathbf{B}^{k_L, k_R, k_D, k_U}$, $k_{\mathcal{I}} = 0, 1$.

This completes the description of our positivity-preserving limiter in 2D. The 3D case is similar.

4.5 Numerical results

In this section, we present the results of numerical simulations using the proposed method. Unless otherwise specified, constrained transport is turned on, the gas constant $\gamma = 5/3$, the CFL number is 0.5, and for 3D simulations the artificial viscosity coefficient is $\nu = 0.01$.

4.5.1 Smooth Alfvén wave

The smooth Alfvén wave problem is often used for convergence studies of numerical schemes for ideal MHD equations [43, 71, 90]. This problem is a one-dimensional problem (computed in multiple dimensions) that has a known smooth solution. In 1D, the initial conditions for this problem are

$$\begin{aligned} &(\rho, u^x, u^y, u^z, p, B^x, B^y, B^z)(0, x) \\ &= (1, 0, 0.1 \sin(2\pi x), 0.1 \cos(2\pi x), 0.1, 1, 0.1 \sin(2\pi x), 0.1 \cos(2\pi x)). \end{aligned} \tag{4.65}$$

The exact solution to (4.65) propagates with the Alfvén speed that is unity (i.e., $\mathbf{q}(t, x) = \mathbf{q}(0, x+t)$). The 2D and 3D smooth Alfvén wave problems are obtained from the 1D problem by rotating the direction of wave propagation.

4.5.1.1 Smooth Alfvén wave: The 2D problem

The 2D version of the smooth Alfvén wave problem is obtained by rotating the direction of propagation by an angle of ϕ , so that the wave now propagates in direction $\mathbf{n} = \langle -\cos \phi, -\sin \phi, 0 \rangle$. Identical to [43, 23], the computational domain we use is $[0, 1/\cos \phi] \times [0, 1/\sin \phi]$, where $\phi = \tan^{-1}(0.5)$. Periodic boundary conditions are applied on all four sides.

For this problem, we present numerical results with and without the energy correction. In Table 4.1, we observe the overall third-order accuracy of the method, and in Table 4.2, we refine Δt faster than the mesh spacing as well as run the solution to a shorter final time in order to extract the spatial order of accuracy. For these test cases, we observe the predicted fourth-order accuracy in space. of convergence in space, third-order in time, and little difference between the results obtained with and without the energy correction turned on. When the flag for the positivity-preserving limiter is turned on in the code, we see identical results as without it, because this problem does not have density or pressure that is near zero. The choice of $m_y = 2m_x$ allows for $\Delta x = \Delta y$.

4.5.1.2 Smooth Alfvén wave: The 3D problem

The setup we use here is the same as that used in [43], Section 6.2.1. The direction of propagation is

$$\mathbf{n} = \langle -\cos \phi \cos \theta, -\sin \phi \cos \theta, \sin \theta \rangle, \quad (4.66)$$

and the computational domain is

$$\left[0, \frac{1}{\cos \phi \cos \theta}\right] \times \left[0, \frac{1}{\sin \phi \cos \theta}\right] \times \left[0, \frac{1}{\sin \theta}\right], \quad (4.67)$$

Mesh	CFL	Error in \mathbf{B}	Order	Error in A^z	Order
32×64	0.5	3.842×10^{-5}	—	5.356×10^{-6}	—
64×128	0.5	4.940×10^{-6}	2.96	7.530×10^{-7}	2.83
128×256	0.5	6.324×10^{-7}	2.97	9.697×10^{-8}	2.96
256×512	0.5	8.020×10^{-8}	2.98	1.218×10^{-8}	2.99

(a)

Mesh	CFL	Error in \mathbf{B}	Order	Error in A^z	Order
32×64	0.5	3.848×10^{-5}	—	5.320×10^{-6}	—
64×128	0.5	4.938×10^{-6}	2.96	7.469×10^{-7}	2.83
128×256	0.5	6.318×10^{-7}	2.97	9.628×10^{-8}	2.96
256×512	0.5	8.009×10^{-8}	2.98	1.210×10^{-8}	2.99

(b)

Table 4.1: 2D smooth Alfvén wave. Here, we show L^∞ -errors at a final time of $t = 1.0$ for the solution with and without the energy “correction” step. Table (a) has the energy correction turned off, and Table (b) has the energy correction turned on. Because time is only discretized to third-order accuracy, we observe the predicted third-order accuracy of the solver here.

Mesh	CFL	Error in \mathbf{B}	Order	Error in A^z	Order
32×64	0.5	3.852×10^{-6}	—	1.078×10^{-7}	—
64×128	0.25	2.356×10^{-7}	4.03	8.121×10^{-9}	3.73
128×256	0.125	1.466×10^{-8}	4.01	5.190×10^{-10}	3.97
256×512	0.0625	9.117×10^{-10}	4.01	3.291×10^{-11}	3.98

(a)

Mesh	CFL	Error in \mathbf{B}	Order	Error in A^z	Order
32×64	0.5	3.852×10^{-6}	—	1.078×10^{-7}	—
64×128	0.25	2.356×10^{-7}	4.03	8.121×10^{-9}	3.73
128×256	0.125	1.466×10^{-8}	4.01	5.190×10^{-10}	3.97
256×512	0.0625	9.117×10^{-10}	4.01	3.291×10^{-11}	3.98

(b)

Table 4.2: 2D smooth Alfvén wave. Here, we show L^∞ -errors at a short final time of $t = 0.01$ for the solution with and without the energy “correction” step. Table (a) has the energy correction turned off, and Table (b) has the energy correction turned on. Here, we refine Δt faster than Δx in order to expose the spatial order of accuracy of the solver. Because we only use a fourth-order accurate spatial discretization for $\nabla \times \mathbf{A}$, we only observe fourth-order accuracy despite the fact that the fluid variables are discretized to fifth-order accuracy.

Mesh	CFL	Error in B	Order	Error in A	Order
$16 \times 32 \times 32$	0.5	4.784×10^{-4}	—	5.116×10^{-5}	—
$32 \times 64 \times 64$	0.5	2.452×10^{-5}	4.29	3.181×10^{-6}	4.01
$64 \times 128 \times 128$	0.5	3.093×10^{-6}	2.99	4.612×10^{-7}	2.79
$128 \times 256 \times 256$	0.5	3.969×10^{-7}	2.96	6.133×10^{-8}	2.91

(a)

Mesh	CFL	Error in B	Order	Error in A	Order
$16 \times 32 \times 32$	0.5	4.882×10^{-4}	—	5.176×10^{-5}	—
$32 \times 64 \times 64$	0.5	2.485×10^{-5}	4.30	3.191×10^{-6}	4.02
$64 \times 128 \times 128$	0.5	3.105×10^{-6}	3.00	4.621×10^{-7}	2.79
$128 \times 256 \times 256$	0.5	3.977×10^{-7}	2.96	6.147×10^{-8}	2.91

(b)

Table 4.3: 3D smooth Alfvén wave. In this table we show the L^∞ -errors at a moderate time of $t = 1.0$. In Table (a) the positivity-preserving limiter is off, and the positivity-preserving limiter (and the energy correction step) is turned on for the results in Table (b). Because time is discretized to third-order accuracy, the final method is formally only third-order accurate in time. In Table 4.4 we run the solver to a short final time in order to expose the spatial order of accuracy.

where $\phi = \theta = \tan^{-1}(0.5)$. Periodic boundary conditions are imposed on all directions.

We again seek to numerically investigate the spatial and temporal orders of accuracy, with and without the energy correction step. The errors in **B** and **A** are presented in Tables 4.3–4.4. Here we choose $m_y = m_z = 2m_x$ so that $\Delta x = \Delta y = \Delta z / \cos \theta$. Similar to the 2D case, we observe fourth-order of convergence in space, third-order in time, and little difference between the results obtained with and without the energy correction step turned on.

4.5.2 2D rotated shock tube problem

Similar to the smooth Alfvén problems, the rotated shock tube problem is a 1D problem, with direction of wave propagation rotated a certain angle. The setup we use in the current

Mesh	CFL	Error in B	Order	Error in A	Order
$16 \times 32 \times 32$	0.5	6.752×10^{-5}	—	5.715×10^{-7}	—
$32 \times 64 \times 64$	0.25	4.280×10^{-6}	3.98	3.856×10^{-8}	3.89
$64 \times 128 \times 128$	0.125	2.666×10^{-7}	4.00	2.613×10^{-9}	3.88
$128 \times 256 \times 256$	0.0625	1.652×10^{-8}	4.01	1.711×10^{-10}	3.93

(a)

Mesh	CFL	Error in B	Order	Error in A	Order
$16 \times 32 \times 32$	0.5	6.752×10^{-5}	—	5.715×10^{-7}	—
$32 \times 64 \times 64$	0.25	4.280×10^{-6}	3.98	3.856×10^{-8}	3.89
$64 \times 128 \times 128$	0.125	2.666×10^{-7}	4.00	2.613×10^{-9}	3.88
$128 \times 256 \times 256$	0.0625	1.652×10^{-8}	4.01	1.712×10^{-10}	3.93

(b)

Table 4.4: 3D smooth Alfvén wave. Here, we show the L^∞ -errors at a short final time of $t = 0.01$. In addition, we refine Δt faster than the mesh spacing in order to extract the spatial order of accuracy. Table (a) has the positivity-preserving limiter turned off, and Table (b) has the positivity-preserving limiter (as well as the correction step) turned on. The results are almost identical.

work is the same as that in [15], which we repeat here for completeness.

The initial conditions consist of a shock

$$(\rho, u_\perp, u_\parallel, u^z, p, B_\perp, B_\parallel, B^z) = \begin{cases} (1, 0, 0, 0, 1, 0.75, 1, 0) & \text{if } \xi < 0, \\ (0.125, 0, 0, 0, 0.1, 0.75, -1, 0) & \text{if } \xi \geq 0, \end{cases} \quad (4.68)$$

where $\xi = x \cos \phi + y \sin \phi$, and u_\perp and B_\perp are vector components perpendicular to the shock interface, and u_\parallel and B_\parallel are the vector components parallel to the shock interface.

Namely

$$u^x = u_\perp \cos \phi - u_\parallel \sin \phi, \quad u^y = u_\perp \sin \phi + u_\parallel \cos \phi, \quad (4.69)$$

$$B^x = B_\perp \cos \phi - B_\parallel \sin \phi, \quad B^y = B_\perp \sin \phi + B_\parallel \cos \phi. \quad (4.70)$$

The initial condition for magnetic potential is

$$A^z(0, x, y) = \begin{cases} 0.75\eta - \xi & \text{if } \xi \leq 0, \\ 0.75\eta + \xi & \text{if } \xi > 0, \end{cases} \quad (4.71)$$

where $\eta = -x \sin \phi + y \cos \phi$.

The computational domain is $[-1, 1] \times [-0.5, 0.5]$ with a 200×100 mesh. The boundary conditions used are zeroth order extrapolation on the conserved quantities and first-order extrapolation on the magnetic potential. That is, we set the conserved quantities at the ghost points to be identical to the last value on the interior of the domain, and we define values for the magnetic potential at ghost points through repeated extrapolation of two point stencils starting with two interior points. On the top and bottom boundaries, the direction of extrapolation is parallel to the shock interface.

In Figure 4.2 we present results for the density of solutions computed using PIF-WENO with and without constrained-transport. We note that the contour plot of the solution obtained without constrained transport does not exhibit the unphysical wiggles as is the case in Fig 2(b) of [23]. However, as can be seen from the plots of the slice at $y = 0$, unphysical oscillations appear in the PIF-WENO scheme that has constrained transport turned off. It is also clear from these plots that the constrained transport method we propose in the current work is able to suppress the unphysical oscillations satisfactorily. As a side note, we find it helps to use a global, as opposed to a local value for α in the Lax-Friedrichs flux splitting for the high-order WENO reconstruction in order to further reduce undesirable spurious oscillations.

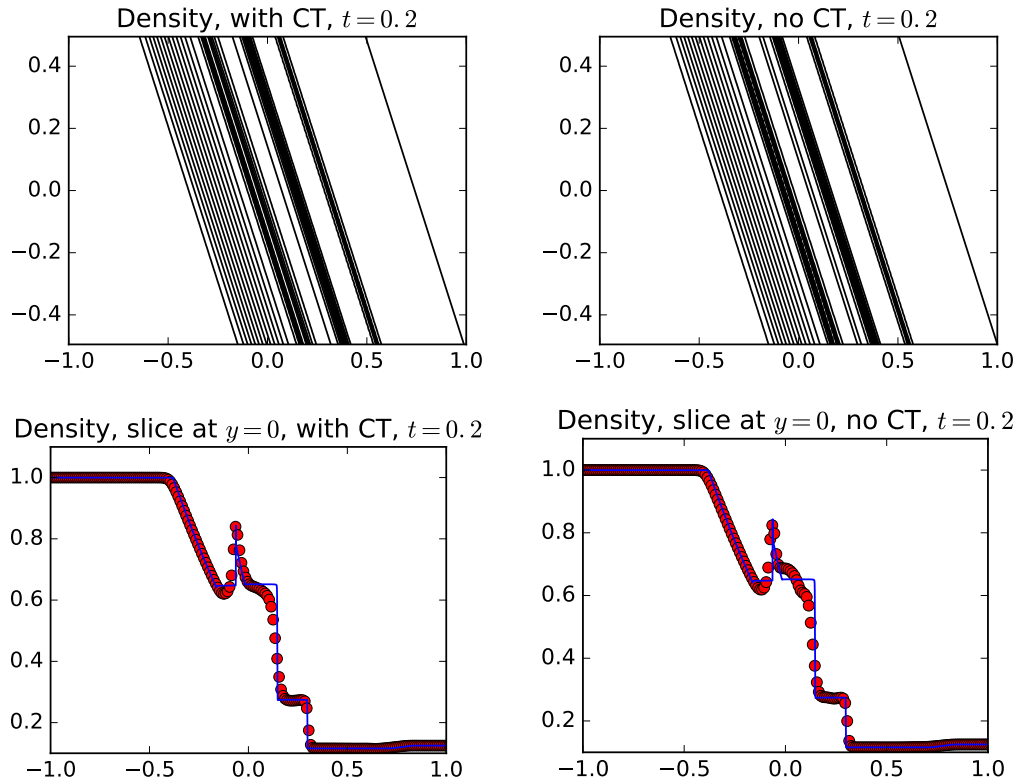


Figure 4.2: The rotated shock tube problem. Here, we compare the solver with (left panels) and without (right panels) constrained transport turned on. A uniform mesh of size 200×100 is used for both simulations. The angle of rotation for the initial conditions is $\phi = \tan^{-1}(0.5)$, and 30 equally spaced contours ranging from the minimum to the maximum of each function are used for the top two panels. The contour plot for the solution without CT contains small wiggles that are much more pronounced when slices of the solution are sampled. To this end, a slice of the solution along $y = 0$ is presented in the bottom two panels. Further evolution produces a solution that causes the code to fail in the case where CT is turned off. The positivity-preserving limiter is turned off in order to exercise the code. The solid lines in the bottom images are reference solutions that are computed by solving the equivalent 1D shock problem on a uniform mesh with 50,000 points with the fifth-order finite difference WENO method.

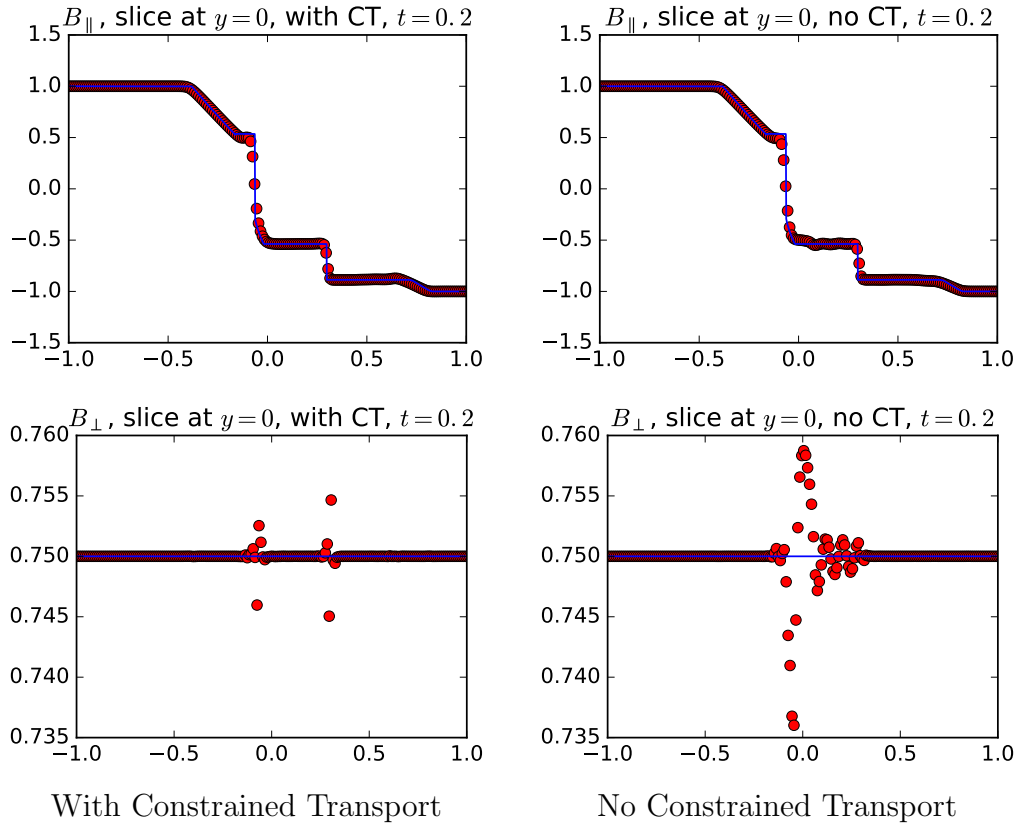


Figure 4.3: 2D rotated shock tube problem. The left panels have constrained transport turned on, and the right panels have constrained transport turned off. Components of the magnetic field at $t = 0.2$ along the slice $y = 0$. The mesh size is 200×100 . The positivity-preserving limiter is turned off in order to exercise the code. Each solid line is the reference solution described in Fig. 4.2. We observe that constrained transport (with the Hamilton-Jacobi solver) allows us to numerically compute magnetic fields with far fewer oscillations than would otherwise be obtainable.

4.5.3 2D Orszag-Tang vortex

In this section, we investigate the Orszag-Tang vortex problem. A notable feature of this problem is that shocks and cortices emerge from smooth initial conditions as time evolves. This is a standard test problem for numerical schemes for MHD equations [23, 26, 71, 90, 94]. The initial conditions are

$$\rho = \gamma^2, \quad \mathbf{u} = (-\sin(y), \sin(x), 0), \quad \mathbf{B} = (-\sin(y), \sin(2x), 0), \quad p = \gamma, \quad (4.72)$$

with an initial magnetic potential of

$$A^z(0, x, y) = 0.5 \cos(2x) + \cos(y). \quad (4.73)$$

The computational domain is $[0, 2\pi] \times [0, 2\pi]$, with double-periodic boundary conditions.

We present in Figure 4.4 the density contour plots at $t = 0.5$, $t = 2$, $t = 3$, and $t = 4$, computed by PIF-WENO with constrained transport on and positivity-preserving limiter on.

Control of divergence error of the magnetic field is critical for this test problem. If we turn off the constrained transport, the simulation crashes at $t = 1.67$. In Figure 4.5 we present plots of the density at time $t = 1.5$ obtained with different configurations of the numerical schemes. Note the development of the nonphysical features in the solution obtained without constrained transport.

We also note that in this problem, where the positivity-preserving limiter is not needed for the simulation, the limiter leads to little difference in the solution. We present in Figures 4.5 and 4.6 plots that demonstrate this. The plots of the type in Figures 4.4 and 4.6 are

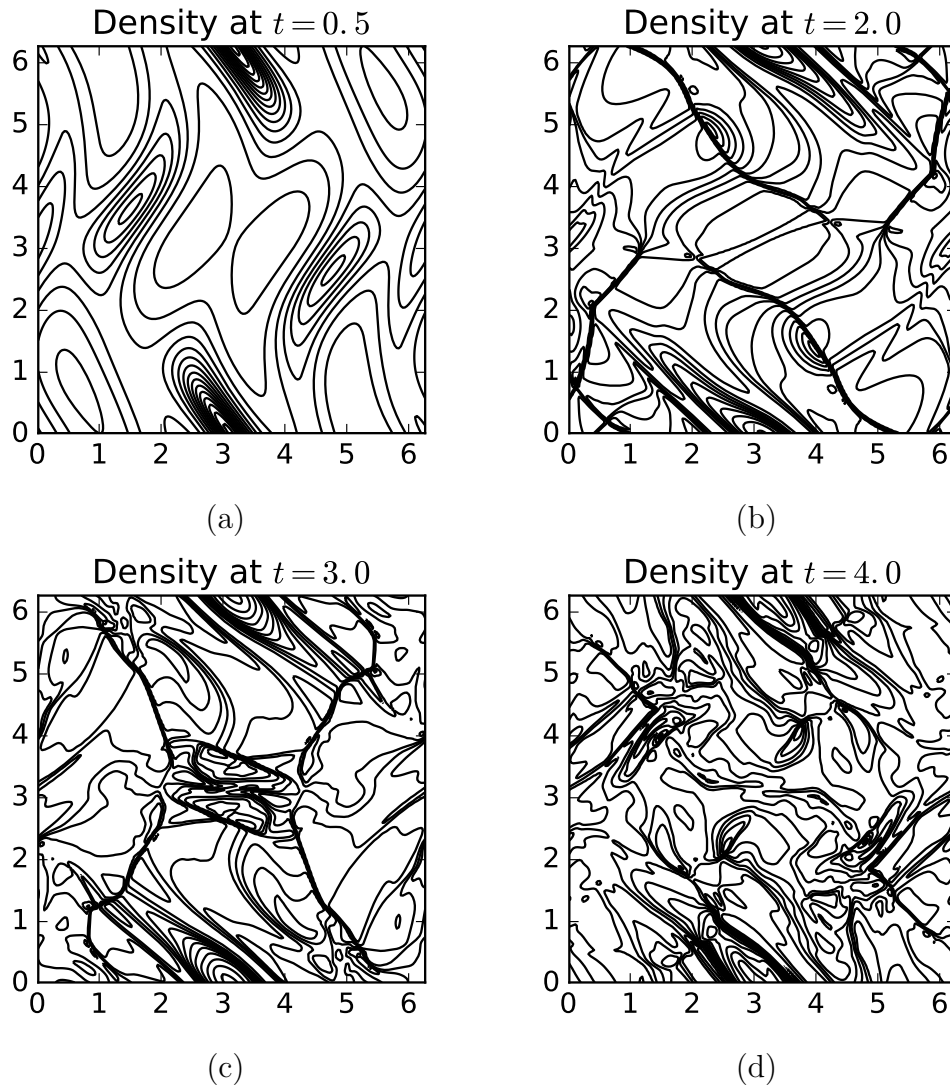


Figure 4.4: The Orszag-Tang problem. We show density contour plots at (a) $t = 0.5$, (b) $t = 2$, (c) $t = 3$, (d) $t = 4$. The solution is computed using PIF-WENO with constrained transport on and positivity-preserving limiter on, on a 192×192 mesh. A total of 15 equally spaced contours are used for each graph.

presented in many sources. Our plots agree with results from the literature [23, 26, 71, 90, 94].

4.5.4 2D rotor problem

This is a two-dimensional test problem that involves low pressure values [8]. The setup we use here is the same as the very low β version found in [91]. These initial conditions are

$$\rho = \begin{cases} 10 & \text{if } r \leq 0.1, \\ 1 + 9\tilde{f}(r) & \text{if } r \in (0.1, 0.115), \\ 1 & \text{if } r \geq 0.115, \end{cases} \quad (4.74)$$

$$u^x = \begin{cases} -10y + 5 & \text{if } r \leq 0.1, \\ (-10y + 5)\tilde{f}(r) & \text{if } r \in (0.1, 0.115), \\ 0 & \text{if } r \geq 0.115, \end{cases} \quad (4.75)$$

$$u^y = \begin{cases} 10x - 5 & \text{if } r \leq 0.1, \\ (10x - 5)\tilde{f}(r) & \text{if } r \in (0.1, 0.115), \\ 0 & \text{if } r \geq 0.115, \end{cases} \quad (4.76)$$

$$u^z = 0, \quad B^x = \frac{2.5}{\sqrt{4\pi}}, \quad B^y = 0, \quad B^z = 0, \quad p = 10^{-8}, \quad A^z = \frac{2.5}{\sqrt{4\pi}}y, \quad (4.77)$$

where

$$r = \sqrt{(x - 0.5)^2 + (y - 0.5)^2}, \quad \tilde{f}(r) = \frac{1}{3}(23 - 200r). \quad (4.78)$$

The computation domain we use is $[0, 1] \times [0, 1]$, with zeroth order extrapolation on the conserved quantities and first order extrapolation on the magnetic potential as the boundary

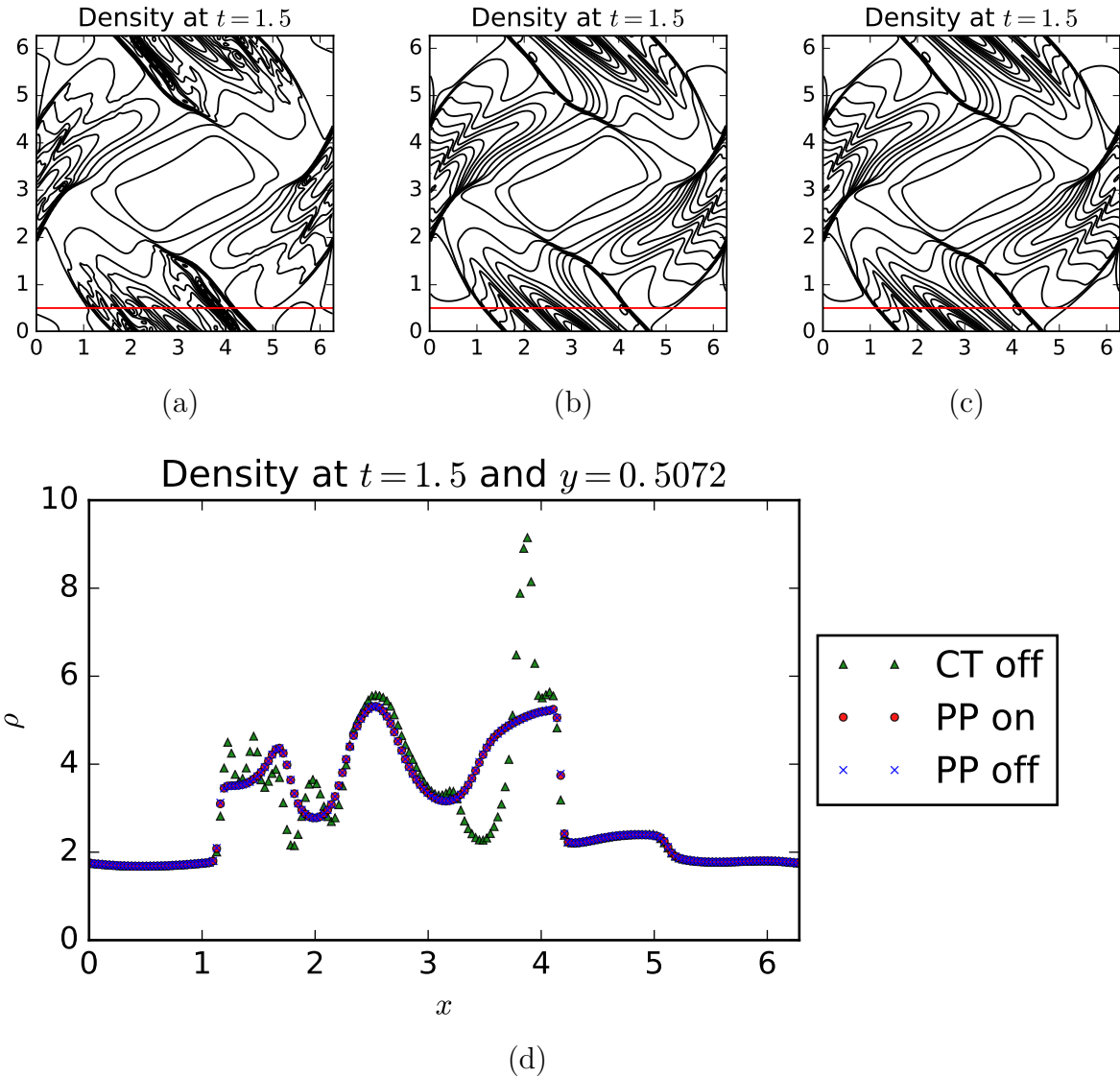


Figure 4.5: The Orszag-Tang problem. Density plots at $t = 1.5$ for solutions computed using different configurations in the numerical scheme. (a) PIF-WENO, with constrained transport turned off; (b) PIF-WENO with constrained transport and positivity preserving limiter turned on; (c) PIF-WENO with constrained transport turned on and positivity preserving limiter turned off; (d) The slice along $y = 0.5072$. The solutions are computed with a 192×192 mesh. A total of 15 equally spaced contours are used for each of (a), (b), and (c).

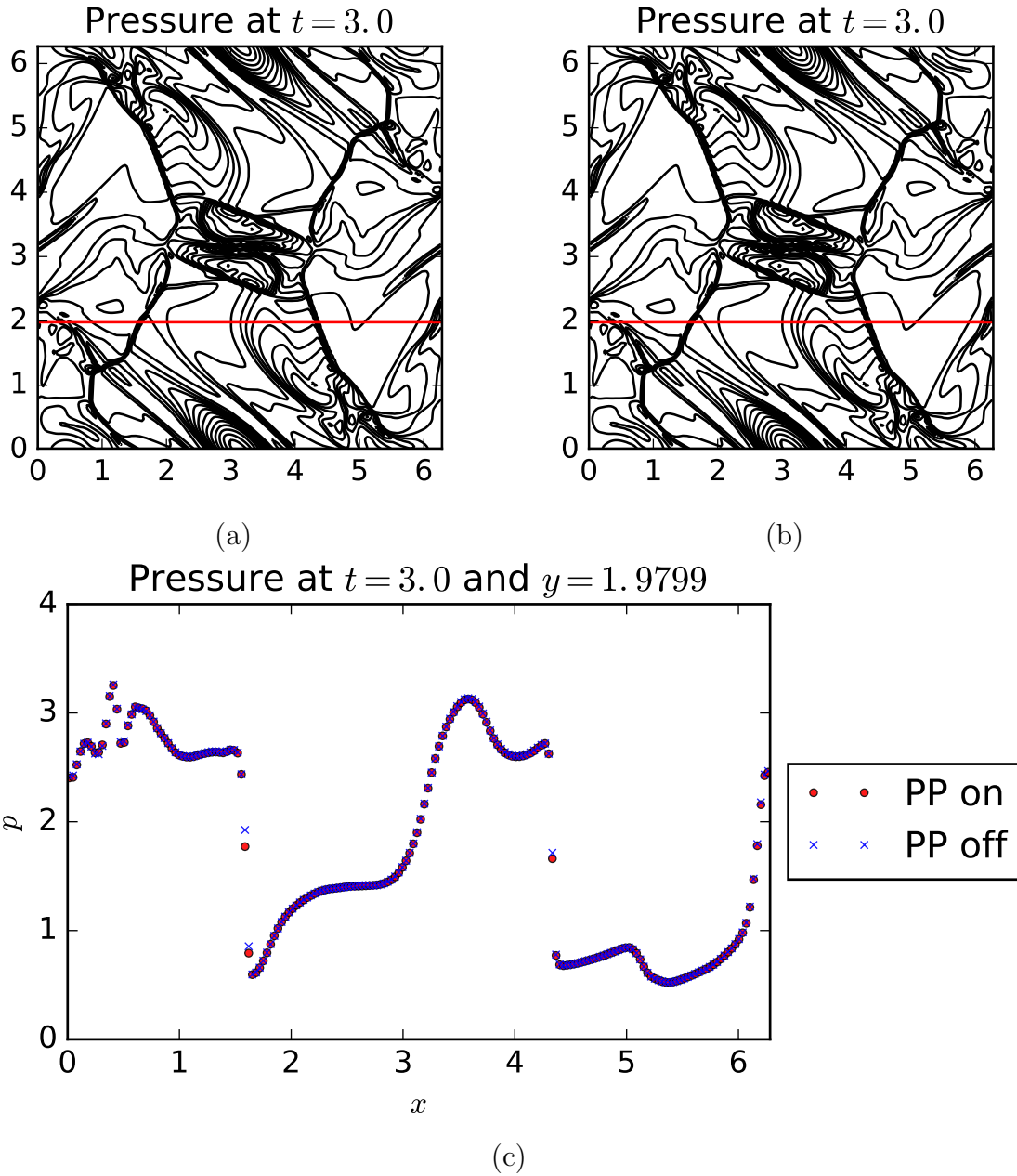


Figure 4.6: The Orszag-Tang problem. Pressure plots at $t = 3.0$ for solutions computed using different configurations in the numerical scheme. (a) PIF-WENO with constrained transport turned on and positivity preserving limiter turned off; (b) PIF-WENO with constrained transport and positivity preserving limiter turned on; (c) The slice along $y = 1.9799$. The solutions are computed with a 192×192 mesh. A total of 15 equally spaced contours are used for each of (a) and (b).

4.5.5 Cloud-shock interaction

The cloud-shock interaction problem is a standard test problem for MHD [23, 26, 43, 44, 71].

The initial conditions are

$$\begin{aligned}
 & (\rho, u^x, u^y, u^z, p, B^x, B^y, B^z) \\
 & = \begin{cases} (3.86859, 11.2536, 0, 0, 167.345, 0, 2.1826182, -2.1826182) & \text{if } x < 0.05, \\ (10, 0, 0, 0, 1, 0, 0.56418958, 0.56418958) & \text{if } x > 0.05 \text{ and } r < 0.15, \\ (1, 0, 0, 0, 1, 0, 0.56418958, 0.56418958) & \text{otherwise,} \end{cases}
 \end{aligned}$$

where $r = \sqrt{(x - 0.25)^2 + (y - 0.5)^2}$ in 2D, and $r = \sqrt{(x - 0.25)^2 + (y - 0.5)^2 + (z - 0.5)^2}$ in 3D denotes the distance to the center of the stationary cloud. For both problems, we use the initial magnetic potential

$$A^x = 0, \quad A^y = 0, \quad A^z = \begin{cases} -2.1826182x + 0.080921431 & \text{if } x \leq 0.05, \\ -0.56418958x & \text{if } x \geq 0.05. \end{cases} \quad (4.79)$$

In the 2D case, we only keep track of A^z .

4.5.5.1 Cloud-shock interaction: The 2D problem

The computational domain we use is $[0, 1] \times [0, 1]$, with zeroth order extrapolation on the conserved quantities and first order extrapolation on the magnetic potential as the boundary conditions on all four sides (i.e., conserved quantities at the ghost points are set equal to the last interior point, and values for the magnetic potential are defined through repeated extrapolation of two point stencils).

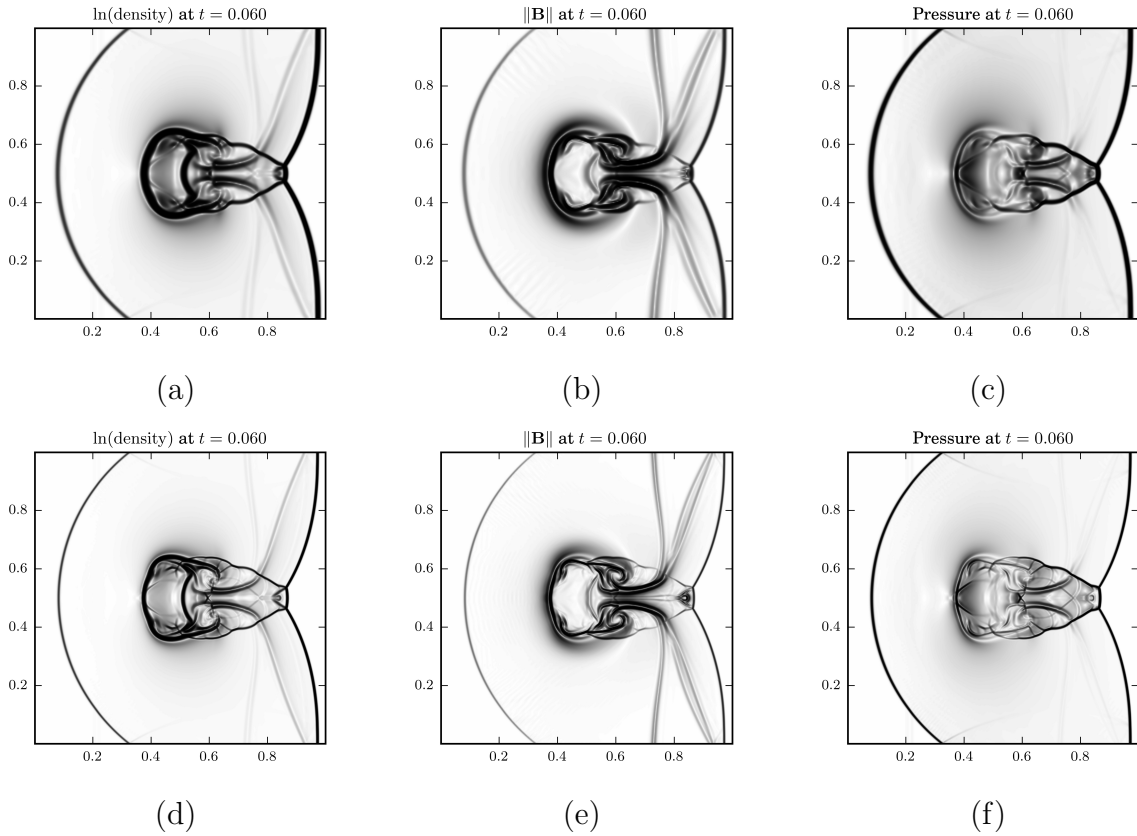


Figure 4.8: The 2D cloud-shock interaction problem. Here, we run the solver to a final time of $t = 0.06$. In the first three panels, we show Schlieren plots for (a) the natural log of the density, (b) the norm of the magnetic field, and (c) the pressure for a mesh of size 256×256 . The same results for a mesh of size 512×512 are presented in panels (d)–(f), where we observe much higher resolution for the problem. Constrained transport and positivity-preserving limiter are turned on for both simulations.

We compute the solution at $t = 0.06$ using a 256×256 mesh. The Schlieren plots of $\ln \rho$ and of $|\mathbf{B}|$ are presented in Figure 4.8. We note here that the current scheme is able to capture the shock-wave-like structure near $x = 0.75$. This is consistent with our previous result in [23], and an improvement over earlier results in [26, 71]. We also note that the positivity-preserving limiter is not required for this simulation. Nonetheless, we present the result here to demonstrate the high resolution of our method, even when the limiter is turned on.

4.5.5.2 Cloud-shock interaction: The 3D problem

The computational domain for this problem is $[0, 1] \times [0, 1] \times [0, 1]$, with zeroth order extrapolation on the conserved quantities and first order extrapolation on the magnetic potential as the boundary conditions on all six faces (i.e., conserved quantities at the ghost points are set equal to the last interior point, and values for the magnetic potential are defined through repeated extrapolation of two point stencils).

We compute the solution to a final time of time $t = 0.06$ on a $256 \times 256 \times 256$ mesh. In Figure 4.9, we show the evolution of the density of the solution. We have two remarks on this result. The first is that the shock-wave-like structure near $x = 0.75$ at the final time is also visible when we use a $128 \times 128 \times 128$ mesh. The second is that the positivity-preserving limiter is required to run this simulation with $256 \times 256 \times 256$ mesh. The reason is that extra structure that contains very low pressure shows up in this mesh at time $t = 0.0378$. This extra structure cannot be observed on the coarser mesh with the method proposed in the current work, nor do we observe it with our previous SSP-RK solver [23]. Therefore, it does not cause trouble for simulations using a $128 \times 128 \times 128$ mesh.

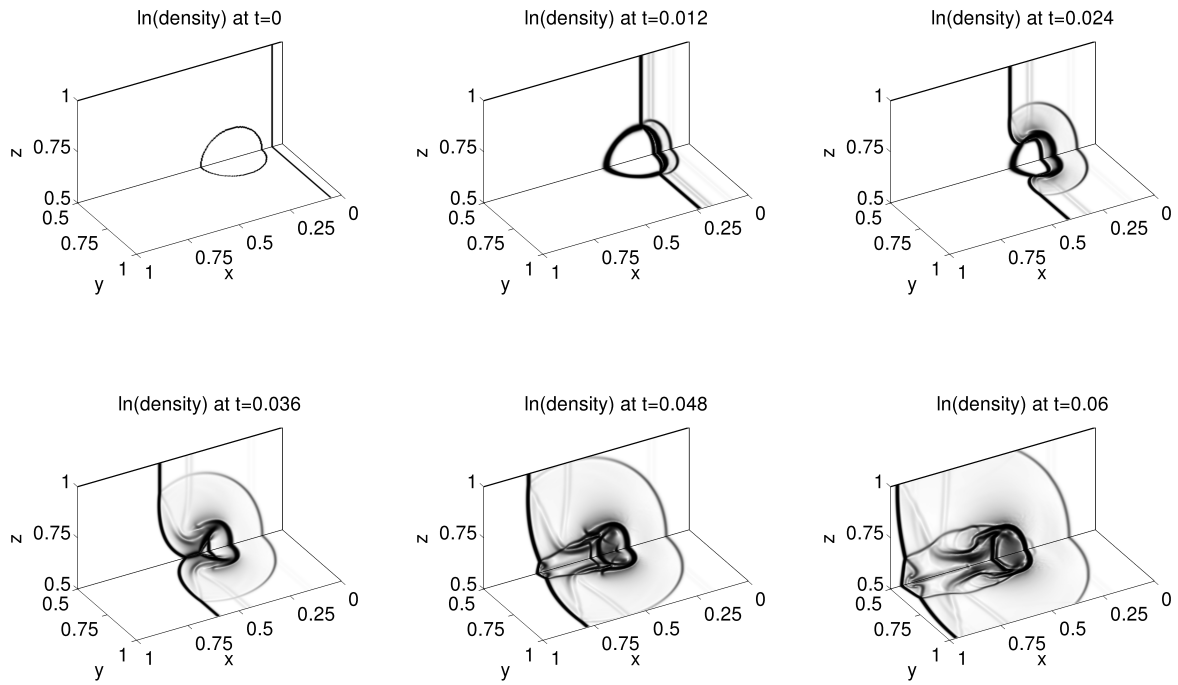


Figure 4.9: The 3D cloud-shock interaction problem. Schlieren plots of $\ln(\rho)$. The solution here is computed using a $256 \times 256 \times 256$ mesh. Cross-sections at $y = 0.5$ and $z = 0.5$ for the region $y \geq 0.5$ and $z \geq 0.5$ are shown. Constrained transport and positivity-preserving limiter are turned on.

4.5.6 Blast wave example

In the blast wave problems, strong shocks interact with a low- β background, which can cause negative pressure if not handled properly. These problems are often used to test the positivity-preserving capabilities of numerical methods for MHD [5, 8, 22, 34, 57, 63, 97].

The initial conditions contain a piecewise defined pressure:

$$p = \begin{cases} 0.1 & r < 0.1, \\ 1000 & \text{otherwise,} \end{cases} \quad (4.80)$$

where r is the distance to the origin, and a constant density, velocity and magnetic field:

$$(\rho, u^x, u^y, u^z, B^x, B^y, B^z) = (1, 0, 0, 0, 100/\sqrt{4\pi}/\sqrt{2}, 100/\sqrt{4\pi}/\sqrt{2}, 0). \quad (4.81)$$

The initial magnetic potential is simply

$$\mathbf{A} = (0, 0, 100y/\sqrt{4\pi}/\sqrt{2} - 100x/\sqrt{4\pi}/\sqrt{2}). \quad (4.82)$$

In 2D we only keep track of A^z , as we do with all the 2D examples.

4.5.6.1 Blast wave example: The 2D problem

In this section, we present our result on the 2D version of the blast wave problem. The computational domain is $[-0.5, 0.5] \times [-0.5, 0.5]$, with zeroth order extrapolation on the conserved quantities and first order extrapolation on the magnetic potential as the boundary conditions on all four sides (i.e., conserved quantities at the ghost points are set equal to the last interior point, and values for the magnetic potential are defined through repeated

extrapolation of two point stencils).

Results for the solution computed to a final time of $t = 0.01$ on a 256×256 mesh are presented in Figure 4.10. There, we display contour plots of ρ , p , $|\mathbf{u}|$, and $|\mathbf{B}|$. These plots are comparable to the previous results in [22]. We note that negative pressure occurs right in the first step if positivity-preserving limiter is turned off.

4.5.6.2 Blast wave example: The 3D problem

For the 3D version of the blast wave problem, we choose the computational domain to be $[-0.5, 0.5] \times [-0.5, 0.5] \times [-0.5, 0.5]$ with zeroth order extrapolation on the conserved quantities and first order extrapolation on the magnetic potential as the boundary conditions on all six faces (i.e., conserved quantities at the ghost points are set equal to the last interior point, and values for the magnetic potential are defined through repeated extrapolation of two point stencils).

The solution at $t = 0.01$ is computed using a $150 \times 150 \times 150$ mesh. We present in Figure 4.11 the plots of the density and pressure, and also in Figure 4.12 the contour plots of the slice at $z = 0$ of the density, pressure, velocity, and magnetic pressure. These results are comparable to those found in [22, 34, 63, 97]. We note here that negative pressure occurs in the second time step if the positivity-preserving limiter is turned off.

4.5.7 Errors in energy conservation

When the positivity-preserving limiter is turned on, we make use of an energy correction step in Eqn. (4.10) in order to keep the pressure the same as before the magnetic field correction. This breaks the conservation of the energy, and therefore we investigate the effect of this step for several test problems. Because (global) energy conservation only holds for problems that

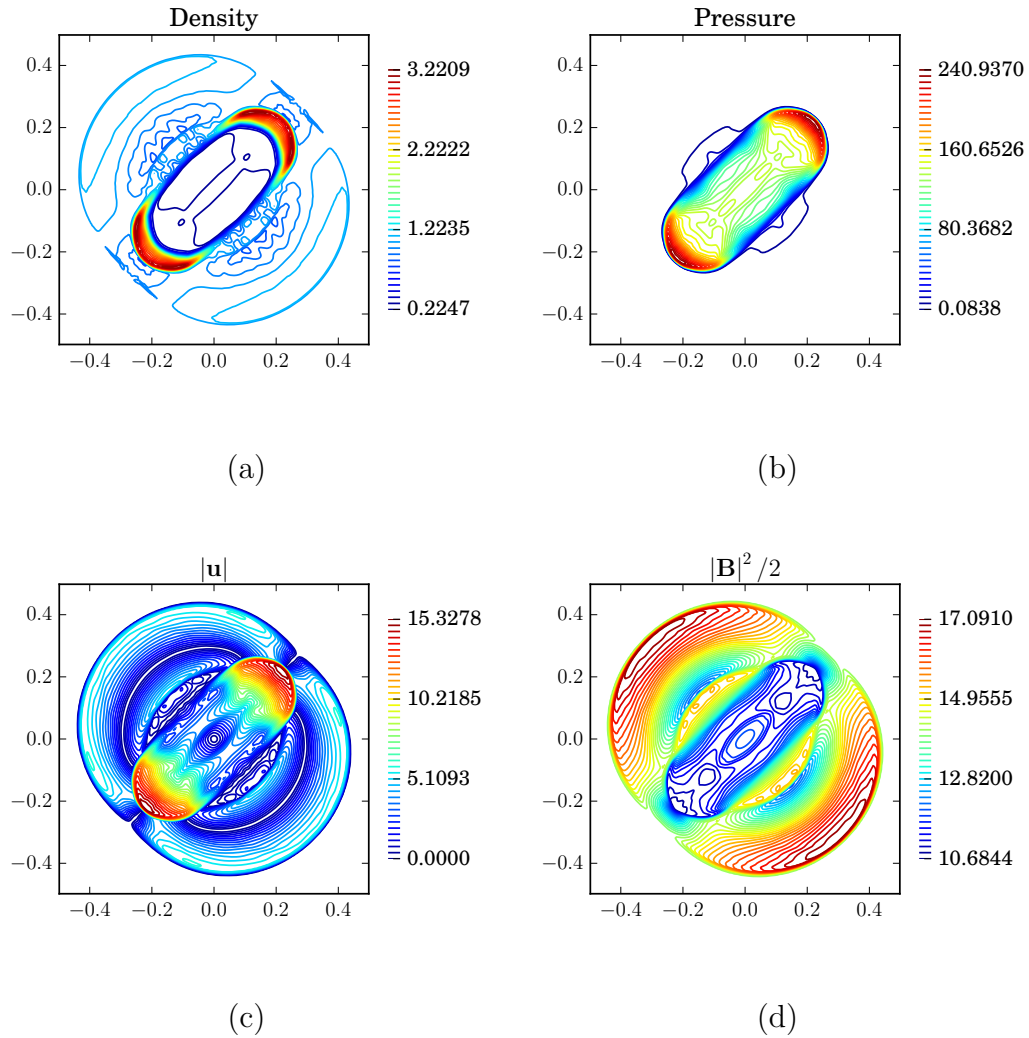


Figure 4.10: 2D blast problem. Shown here are the contour plots at $t = 0.01$ of (a) density, (b) thermal pressure, (c) magnitude of velocity, and (d) magnetic pressure. A total of 40 equally spaced contours ranging from the min to the max of the function are used for each plot. The mesh size is 256×256 .

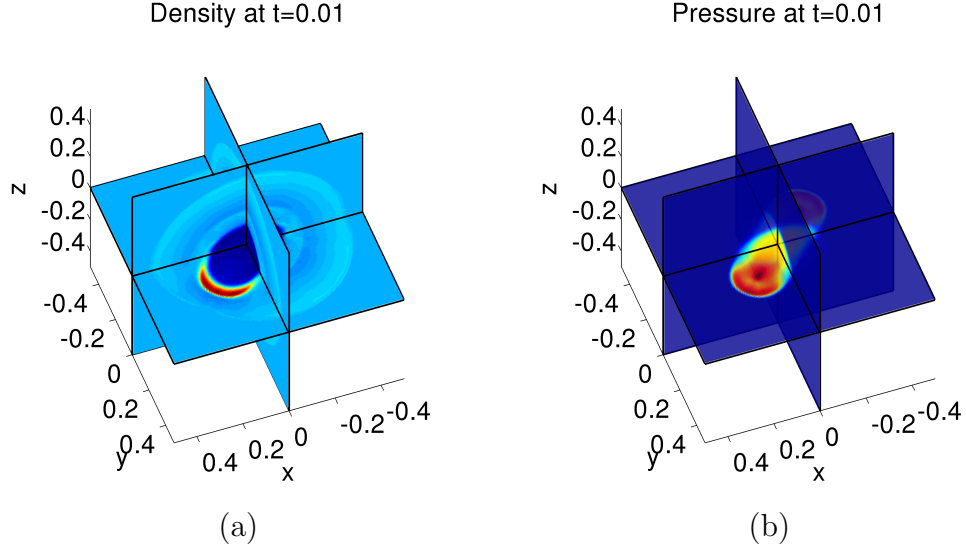


Figure 4.11: 3D blast problem. Shown here are the pseudocolor plots at $t = 0.01$ of (a) density and (b) pressure. The mesh size is $150 \times 150 \times 150$. In Figure 4.12 we plot a cut of the solution along $z = 0$. The positivity-preserving limiter is required to simulate this problem.

have either periodic boundary conditions or constant values near the boundary throughout the entire simulation, we only choose problems with this property for our test cases.

For the 2D problems, the (relative) energy conservation error at time $t = t^n$ is defined as

$$\text{Energy conservation error} := \frac{\left| \sum_{i,j} (\mathcal{E}_{i,j}^n - \mathcal{E}_{i,j}^0) \right|}{\sum_{i,j} \mathcal{E}_{i,j}^0}, \quad (4.83)$$

and the energy conservation errors for the 3D problems are defined similarly.

Results for the 2D and 3D smooth Alfvén test case are presented in Figure 4.13, where we observe negligible errors produced by the energy correction step. We attribute this to the fact that this problem retains a smooth solution for the entirety of the simulation. Results for problems with shocks and vortices are presented in Figure 4.14, where we find non-zero errors. For each of these test problems, we present the results from several different sizes of meshes. All the problems are run to the final time found in Sections 4.5.1–4.5.6 save one.

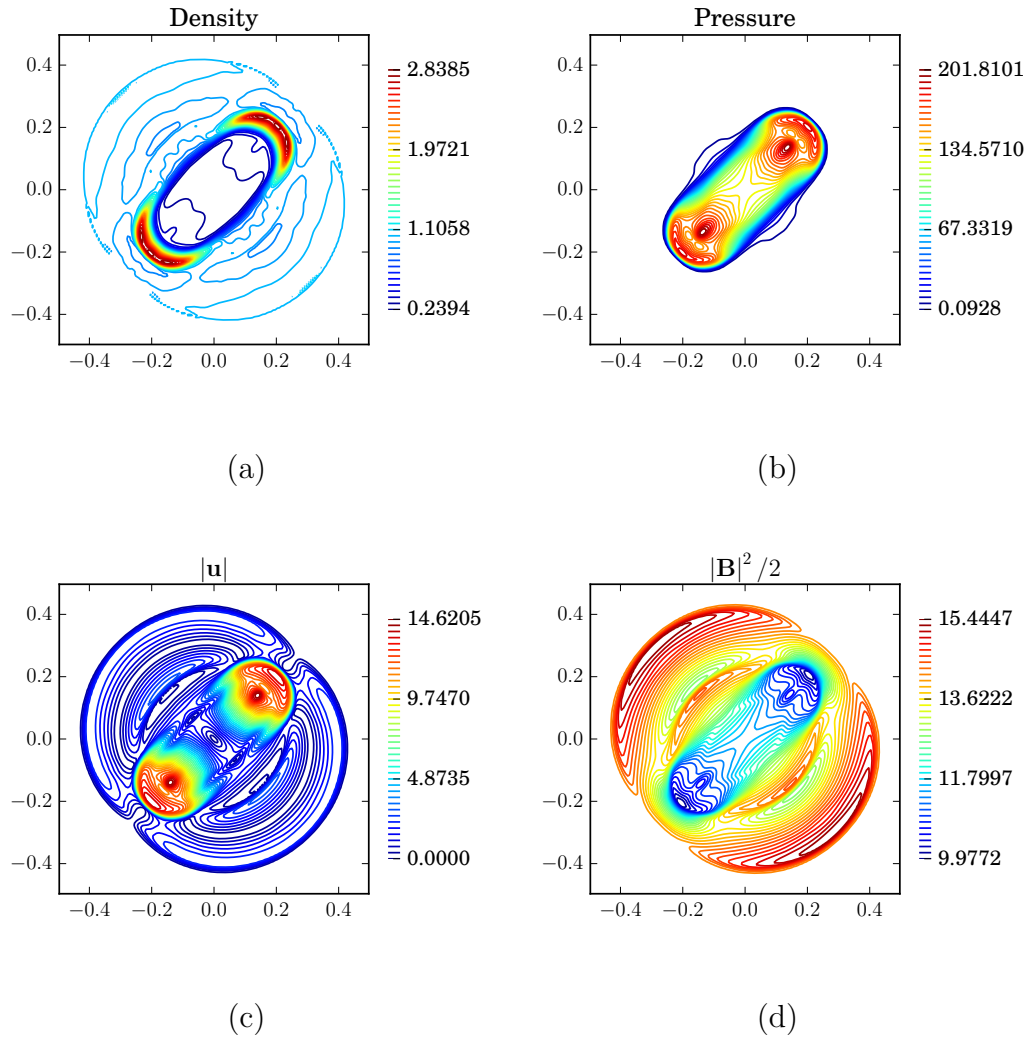


Figure 4.12: 3D blast problem. Shown are the contour plots at time $t = 0.01$ cut at $z = 0$ of (a) density, (b) thermal pressure, (c) norm of velocity, and (d) magnetic pressure. The solution is obtained using a $150 \times 150 \times 150$ mesh. A total of 40 equally spaced contours are used for each plot.

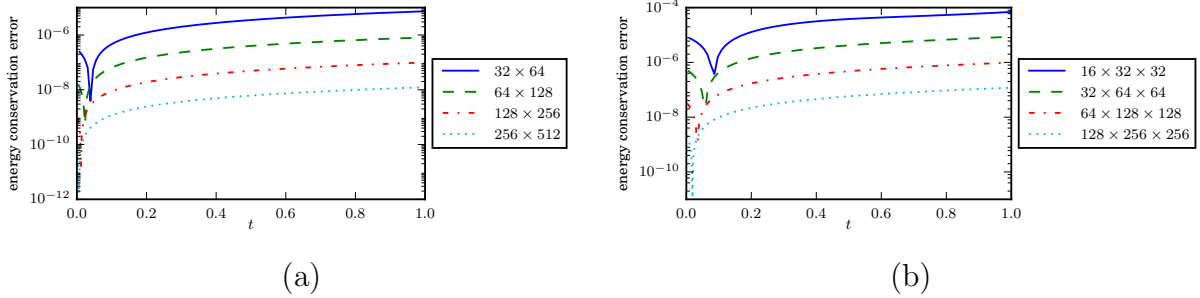


Figure 4.13: Energy conservation errors for the smooth Alfvén test cases. Shown here are results for the (a) 2D smooth Alfvén , and (b) 3D smooth Alfvén test cases. In order to extract the errors, we plot the results on a semi-log scale because otherwise the results are indiscernible from the t -axis. For this smooth test case, the effect of the the energy correction step (and hence the positivity-preserving limiter) is negligible because the solution remains smooth for the entire simulation.

For the 2D Orszag-Tang problem, we run the simulations to a much later time of $t = 30$ in order to quantify the energy conservation errors for a long time simulation on a non-trivial problem.

Finally, in Figure 4.15 we also include the conservation errors when the positivity-preserving limiter is turned off. We observe that the solver retains total energy up to machine roundoff errors, as should be the case.

We note the following patterns in the energy conservation errors:

- The errors are below 1% for all the test problems in the duration of the simulations presented;
- When the positivity-preserving limiter is turned on, the errors grow linearly in time and decrease as the mesh is refined.

We therefore conclude that the violation in energy conservation introduced by the positivity-preserving limiter is insignificant for the problems tested in this work.

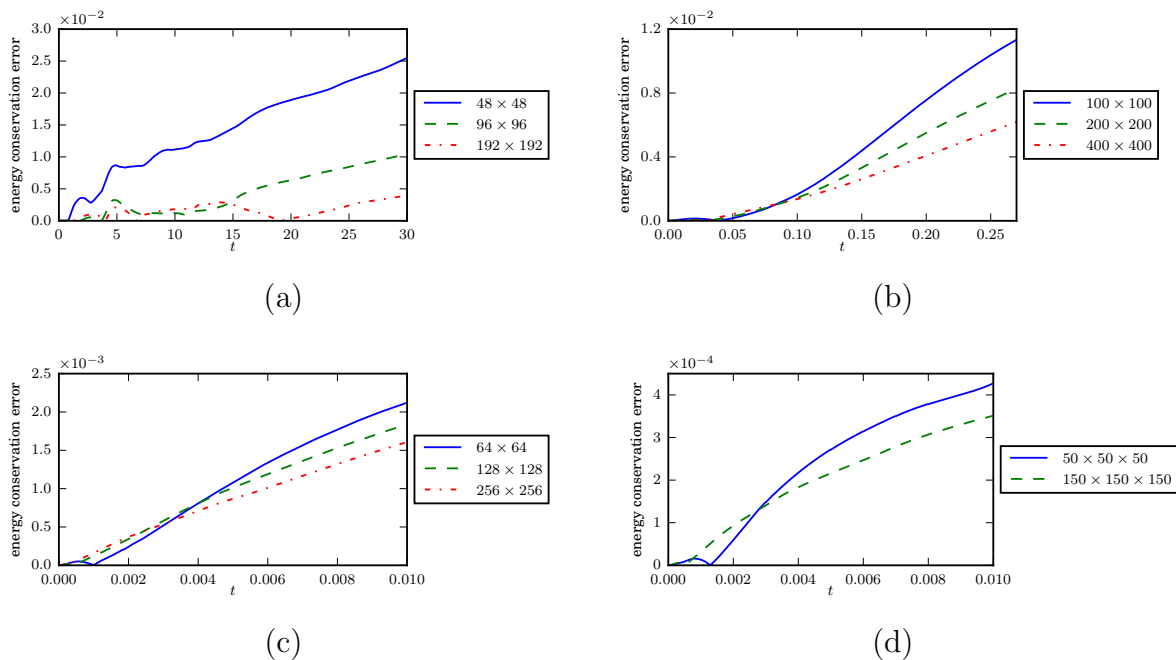


Figure 4.14: Energy conservation errors. Shown here are conservation errors when the positivity-preserving limiter (and hence the energy correction step) is turned on. (a) 2D Orszag-Tang problem, (b) 2D rotor problem, (c) 2D blast problem, and (d) 3D blast problem. Note that the rotor and blast problems require the application of a positivity-preserving limiter in order to run, but this comes at the expense of losing energy conservation. For the Orszag-Tang test problem, we run to a late final time. Again, we observe that the errors in energy conservation decrease as the mesh is refined.

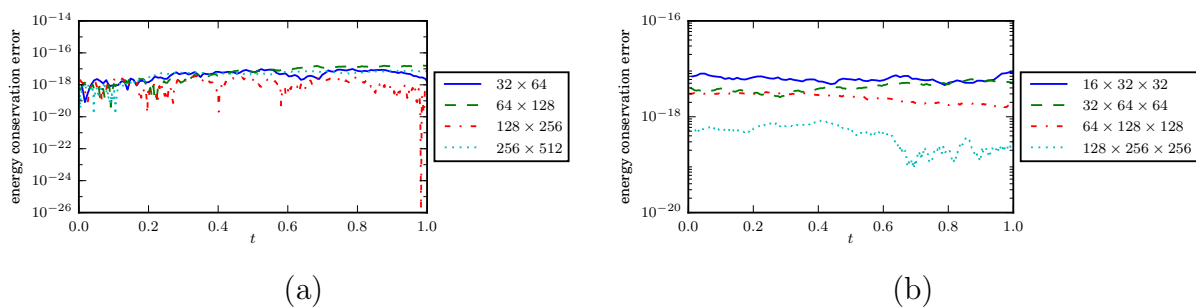


Figure 4.15: Energy conservation errors. Here, we show results for conservation errors when the positivity-preserving limiter (and hence the energy correction step) is turned off. The solver analytically conserves the discrete total energy up to machine precision. Shown here are results for the (a) 2D smooth Alfvén, and (b) 3D smooth Alfvén test cases. Note the logarithmic scale for the axes, and that these errors are numerically conserved up to machine precision.

Chapter 5

A high-order finite difference scheme for ideal magnetohydrodynamics on curvilinear meshes based on an alternative formulation of the WENO scheme and constrained transport

In this chapter, we describe our second scheme, a high-order finite difference scheme for the ideal MHD equations, which is based on an alternative formulation of the WENO scheme and uses constrained transport to control the divergence error of the magnetic field.

In Section 5.1, we describe an alternative flux formulation of the WENO scheme, which is based on the scheme proposed in [51, 52], with the addition of a limiter on the higher order terms. This scheme will be the base scheme we use to solve the ideal MHD equations. In Section 5.2, we describe several HLL type approximate Riemann solvers for the ideal MHD equations. In particular, we describe the HLLD solver in 5.2.3, which is one of the two Riemann solvers we experiment in a component of our base scheme (see Equation (5.22)), the other being Lax-Friedrichs. In Sections 5.3 and 5.4, we describe constrained transport and

positivity-preserving in the current context. Finally in Section 5.5, we present the numerical results.

5.1 An alternative flux formulation of the WENO scheme

In this section, we describe a WENO scheme based on an alternative formulation of fluxes.

5.1.1 Introduction

The simplest hyperbolic conservation law takes the form

$$\frac{\partial q}{\partial t} + \frac{\partial f(q)}{\partial x} = 0, \quad (5.1)$$

where q is a scalar function of t and x , and f is a function of q . Here q is the *conserved quantity* and f is the *flux*. Note this is Equation (2.4) with $m = n = 1$. In order to solve Equation (5.1), we use a semi-discrete conservative finite difference scheme, where we use a uniform mesh with $x_i = i\Delta x$ and discretize Equation (5.1) in space to get

$$\frac{\partial q_i}{\partial t} + \frac{1}{\Delta x}(\hat{f}_{i+1/2} - \hat{f}_{i-1/2}) = 0. \quad (5.2)$$

Here q_i sits on x_i and \hat{f} is some numerical flux that sits on half grid points and depends on the q_i 's. This numerical flux satisfies

$$\frac{1}{\Delta x} \left(\hat{f}_{i+1/2} - \hat{f}_{i-1/2} \right) = \partial_x f(q(x))|_{x_i} + \mathcal{O}(\Delta x^m), \quad (5.3)$$

where m is the spatial order of accuracy of the scheme. Equation (5.1) is then integrated in time using some ODE solver, e.g. Runge-Kutta method. In the current work, we have used the third-order SSP-RK method proposed in [39].

The numerical flux \hat{f} is a high order approximation to the so-called *sliding function* h of $f(q)$. If we let h be the function such that

$$f(q(x)) = \frac{1}{\Delta x} \int_{x-\Delta x/2}^{x+\Delta x/2} h(\xi) d\xi, \quad (5.4)$$

we would have

$$\hat{f}_{i+1/2} = h(x_{i+1/2}) + \mathcal{O}(\Delta x^m). \quad (5.5)$$

Equations (5.4) and (5.5) actually says that we are given the average of h over cells centered at the grid points x_i 's and we need to approximate the values of the function h at half grid points $x_{i+1/2}$'s from those cell averages. This is the *reconstruction problem* at the heart of standard finite volume schemes [41, 60] and has been used to construct various finite difference numerical schemes for hyperbolic conservation laws [79, 49, 6, 77]. It is possible to compute $\hat{f}_{i+1/2}$ directly from the values of f on grid points using the procedure described in Section 3.2. This is sometime called *the* finite difference WENO scheme. We refer the reader to [77] for details. It was noted in [76] that while Equation (5.3) requires the error in Equation (5.5) be of $\mathcal{O}(\Delta x^{m+1})$, the $\mathcal{O}(\Delta x^m)$ error is sufficient because when f is smooth, cancellations in the error terms will give rise to (5.3).

It is noted in [78] that a Taylor expansion of the sliding function h at $x_{i+1/2}$ gives the

following expression of $h_{i+1/2}$ in terms of the cell average function f ,

$$h_{i+1/2} = f_{i+1/2} + \sum_{k=1}^{[(m-1)/2]} a_{2k} \Delta x^{2k} \left(\frac{\partial^{2k}}{\partial x^{2k}} f \right)_{i+1/2} + \mathcal{O}(\Delta x^m), \quad (5.6)$$

where the a_{2k} 's are some constants. In the examples we show later, we use a truncation at $m = 5$, and therefore approximate \hat{f} by

$$\hat{f}_{i+1/2} = f_{i+1/2} - \frac{1}{24} \Delta x^2 \partial_x^2 f|_{i+1/2} + \frac{7}{5760} \Delta x^4 \partial_x^4 f|_{i+1/2}. \quad (5.7)$$

The first term in Equation (5.7) is approximated by

$$f_{i+1/2} = F(q_{i+1/2}^-, q_{i+1/2}^+), \quad (5.8)$$

where F is a monotone flux [86] and $q_{i+1/2}^\pm$ are sufficiently high-order one-sided approximations to q at $x_{i+1/2}$. The WENO interpolation described in Section 3.1 is used to obtain $q_{i+1/2}^\pm$. The higher order terms in Equation (5.7) are approximated using central differences together with a limiter constructed from the WENO smoothness indicators in (3.18).

In what follows, we shall first describe the aforementioned limiter in Section 5.1.2. After that, we will describe how we handle one-dimensional systems, multidimensional cases, and curvilinear meshes in Sections 5.1.3, 5.1.4, and 5.1.5, respectively.

5.1.2 A limiter on the higher order terms in the numerical flux

In this section, we look at approximations to the terms in the summation in Equation (5.6).

In order that we retain an $\mathcal{O}(\Delta x^m)$ error, the approximation to $\left(\frac{\partial^{2k}}{\partial x^{2k}} f \right)_{i+1/2}$ must be

of error $\mathcal{O}(\Delta x^{m-2k})$. In the special case when $m = 5$, this requirement can be satisfied by using the central differences

$$\begin{aligned}\Delta x^2 \partial_x^2 f|_{i+1/2} &\approx \frac{1}{48} (-5f_{i-2} + 39f_{i-1} - 34f_i - 34f_{i+1} + 39f_{i+2} - 5f_{i+3}), \\ \Delta x^4 \partial_x^4 f|_{i+1/2} &\approx \frac{1}{2} (f_{i-2} - 3f_{i-1} + 2f_i + 2f_{i+1} - 3f_{i+2} + f_{i+3}).\end{aligned}\tag{5.9}$$

Note that the stencil needed in Equation (5.9) is contained in the union of S^\pm used in the WENO interpolation procedure described in Section 3.1.

Equation (5.9) is the approach used in [52] to approximate the second and third terms in (5.7). In the original article [51] on the alternative flux formulation WENO scheme, the higher order derivatives $\partial_x^2 f|_{i+1/2}$ and $\partial_x^4 f|_{i+1/2}$ are further expanded in terms of the derivatives of f with respect to q and the derivatives of q with respect to x , before central differences are applied. In both of these articles, which deal with Euler equations of hydrodynamics, satisfactory results can be obtained without using special treatments on these terms. However, in experimenting with the MHD equations, we find it necessary to apply an additional limiter on these terms.

In the case of $m = 5$, we would like to multiply the second and third terms on the right hand side of (5.9) by a number σ that satisfies

$$\begin{aligned}\sigma &= 1 + \mathcal{O}(\Delta x^3), \quad \text{when } q \text{ is smooth on the stencil } S = \{x_{i-2}, \dots, x_{i+3}\}, \\ \sigma &= \mathcal{O}(\Delta x^2), \quad \text{when } q \text{ contains a strong discontinuity on } S.\end{aligned}\tag{5.10}$$

Such σ can be constructed from the smoothness indicators used in WENO interpolation

in the following way. We start from the β_k 's defined in Equation (3.18) and then set

$$\begin{aligned}\sigma_{\max} &= 1 + \frac{|\beta_0 - \beta_2|}{\epsilon + \min\{\beta_0, \beta_1, \beta_2\}}, \\ \sigma_{\min} &= 1 + \frac{|\beta_0 - \beta_2|}{\epsilon + \max\{\beta_0, \beta_1, \beta_2\}},\end{aligned}\tag{5.11}$$

where ϵ is a small positive number (taken to be 10^{-6} in all our examples) to avoid division by zero. We can thus obtain a candidate for the coefficient σ by

$$\sigma^- = \frac{\sigma_{\min}}{\sigma_{\max}}.\tag{5.12}$$

Note that σ^- depends only on the stencil $S^- = \{x_{i-2}, \dots, x_{i+2}\}$. A similar formula for $S^+ = \{x_{i-1}, \dots, x_{i+3}\}$ gives rise to another candidate σ^+ . We then set

$$\sigma = \min\{\sigma^-, \sigma^+\}.\tag{5.13}$$

5.1.3 One-dimensional systems

We consider one-dimensional hyperbolic systems of conservation laws, which are the special case of (2.4) with $m = 1$.

A one-dimensional system of conservation law takes the form

$$\frac{\partial \mathbf{q}}{\partial t} + \frac{\partial \mathbf{f}(\mathbf{q})}{\partial x} = 0,\tag{5.14}$$

where

$$\mathbf{q} = (q^1(t, x), \dots, q^n(t, x))\tag{5.15}$$

is a vector function of t and x and

$$\mathbf{f}(\mathbf{q}) = (f^1(\mathbf{q}), \dots, f^n(\mathbf{q})) \quad (5.16)$$

is the flux function. Here superscripts denote the components of the vectors. Suppose the system (5.14) is hyperbolic, that is, the Jacobian $\partial\mathbf{f}/\partial\mathbf{q}$ has n real eigenvalues

$$\lambda_1(\mathbf{q}) \leq \dots \leq \lambda_n(\mathbf{q}) \quad (5.17)$$

and a set of n independent (right) eigenvectors

$$\mathbf{r}_1(\mathbf{q}), \dots, \mathbf{r}_n(\mathbf{q}). \quad (5.18)$$

Thus, if we let

$$R(\mathbf{q}) = (\mathbf{r}_1(\mathbf{q}), \dots, \mathbf{r}_n(\mathbf{q})) \quad (5.19)$$

be the matrix whose columns are the eigenvectors of $\partial\mathbf{f}/\partial\mathbf{q}$, we will have

$$R^{-1}(\mathbf{q}) \frac{\partial\mathbf{f}}{\partial\mathbf{q}} R(\mathbf{q}) = \text{diag}(\lambda_1(\mathbf{q}), \dots, \lambda_n(\mathbf{q})). \quad (5.20)$$

Similar to Equation (5.7), we have, in the case of spatial order of accuracy $m = 5$, the numerical flux

$$\hat{\mathbf{f}}_{i+1/2} = \mathbf{f}_{i+1/2} - \frac{1}{24}\Delta x^2 \partial_x^2 \mathbf{f}|_{i+1/2} + \frac{7}{5760}\Delta x^4 \partial_x^4 \mathbf{f}|_{i+1/2}, \quad (5.21)$$

where

$$\mathbf{f}_{i+1/2} = \mathbf{F}(\mathbf{q}_{i+1/2}^-, \mathbf{q}_{i+1/2}^+) \quad (5.22)$$

is obtained from some monotone flux \mathbf{F} resulted from any of a variety of Riemann solvers, with $\mathbf{q}_{i+1/2}^\pm$ obtained from WENO interpolation, and the higher order terms is obtained using a combination of central differences and an additional limiter, same as described in Section 5.1.2.

In the case of a hyperbolic *system*, the WENO interpolation we use to obtain $\mathbf{q}_{i+1/2}^\pm$ is performed on the local characteristic variables instead of on the components of \mathbf{q} . To be more precise, we have the following algorithm.

1. At each half grid point $x_{i+1/2}$, compute an average state $\mathbf{q}_{i+1/2}$. In all the examples we show later for the MHD equations, we have used the arithmetic mean of primitive variables, that is, set

$$\psi_{i+1/2} = \frac{1}{2}(\psi_i + \psi_{i+1}) \quad (5.23)$$

for the variables ψ ranging over $\{\rho, \mathbf{u}, p, \mathbf{B}\}$, and recover the conserved variables $\mathbf{q} = \{\rho, \rho\mathbf{u}, \mathcal{E}, \mathbf{B}\}$ from the ψ 's.

2. At each half grid point $x_{i+1/2}$, compute the right and left eigenvectors of the Jacobian $\partial\mathbf{f}/\partial\mathbf{q}$.
3. At each half grid point $x_{i+1/2}$, project the conserved quantities in the stencil needed for computing the numerical flux $\hat{f}_{i+1/2}$ onto the local characteristic variables. That is, let

$$\mathbf{v}_{i,k} = R_{i+1/2}^{-1} \mathbf{q}_i, \quad \text{for } k = -r + 1, \dots, r, \quad (5.24)$$

where we use $\mathbf{v}_{i,k}$ to denote the local characteristic variables, and R^{-1} is the left

eigenvectors computed in last step.

4. For each i , perform the WENO interpolation on the $\mathbf{v}_{i,k}$'s to get $\mathbf{v}_{i+1/2}^\pm$.
5. For each i , project $\mathbf{v}_{i+1/2}^\pm$ back onto the conserved quantities,

$$\mathbf{q}_{i+1/2}^\pm = R_{i+1/2} \mathbf{v}_{i+1/2}^\pm. \quad (5.25)$$

5.1.4 Multidimensional cases

Hyperbolic conservation laws in more than one spatial dimensions can be treated in a dimension-by-dimension fashion, as is usually done in finite difference schemes.

For example, a system of hyperbolic conservation law in two dimensions takes the form

$$\frac{\partial \mathbf{q}}{\partial t} + \frac{\partial \mathbf{f}(\mathbf{q})}{\partial x} + \frac{\partial \mathbf{g}(\mathbf{q})}{\partial y} = 0, \quad (5.26)$$

where \mathbf{q} is a vector function of t , x , and y , and \mathbf{f} and \mathbf{g} are the fluxes in the x and y directions, respectively. On a uniform mesh with $x_i = i\Delta x$ and $y_j = j\Delta y$, Equation (5.26) can be solved by using the semi-discrete scheme

$$\frac{\partial \mathbf{q}_{i,j}}{\partial t} + \frac{1}{\Delta x} (\hat{\mathbf{f}}_{i+1/2,j} - \hat{\mathbf{f}}_{i-1/2,j}) + \frac{1}{\Delta y} (\hat{\mathbf{g}}_{i,j+1/2} - \hat{\mathbf{g}}_{i,j-1/2}) = 0, \quad (5.27)$$

where

$$\frac{1}{\Delta x} (\hat{\mathbf{f}}_{i+1/2,j} - \hat{\mathbf{f}}_{i-1/2,j}) = \partial_x \mathbf{f}(\mathbf{q}(x, y))|_{(x_i, y_j)} + \mathcal{O}(\Delta x^{m-1}) \quad (5.28)$$

and

$$\frac{1}{\Delta y} (\hat{\mathbf{g}}_{i,j+1/2} - \hat{\mathbf{g}}_{i,j-1/2}) = \partial_y \mathbf{g}(\mathbf{q}(x, y))|_{(x_i, y_j)} + \mathcal{O}(\Delta y^{m-1}) \quad (5.29)$$

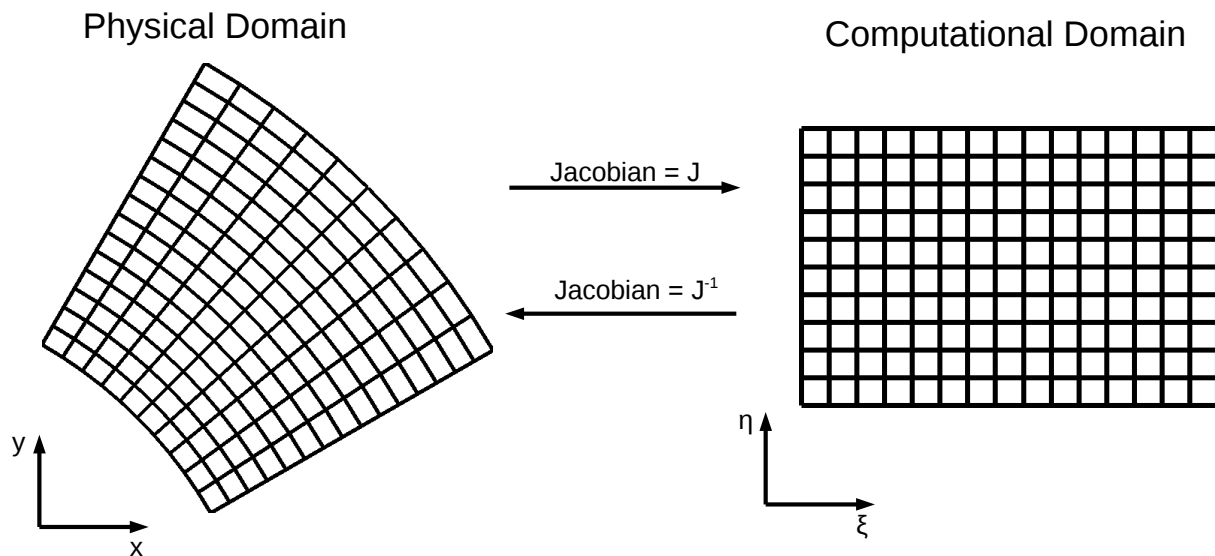


Figure 5.1: A schematic diagram of the physical and computational domain for curvilinear meshes.

for a scheme with spatial order of accuracy equal to m . Now $\hat{\mathbf{f}}$ and $\hat{\mathbf{g}}$ can be approximated by using the method described in the previous sections.

5.1.5 Curvilinear meshes

In this section, we consider the situation where the mesh on the physical domain is obtained from a uniform mesh on the computational domain via a continuous map.

Suppose we have a two-dimensional scalar equation of hyperbolic conservation law (5.26). Also, suppose the coordinates (x, y) is related to the *curvilinear coordinates* (ξ, η) via some continuous coordinate transformation. We also let

$$J = \begin{vmatrix} \xi_x & \xi_y \\ \eta_x & \eta_y \end{vmatrix} = \begin{vmatrix} x_\xi & x_\eta \\ y_\xi & y_\eta \end{vmatrix}^{-1} \quad (5.30)$$

be the Jacobian of the transformation. See Figure 5.1 for a schematic diagram.

Transforming Equation (5.26) into an equation of conservation law in the curvilinear coordinates gives

$$\frac{\partial \tilde{q}}{\partial t} + \frac{\partial \tilde{f}}{\partial \xi} + \frac{\partial \tilde{g}}{\partial \eta} = 0, \quad (5.31)$$

where

$$\tilde{q} = q/J, \quad \tilde{f} = \tilde{\xi}_x f + \tilde{\xi}_y g, \quad \tilde{g} = \tilde{\eta}_x f + \tilde{\eta}_y g, \quad (5.32)$$

for the metric terms defined by

$$\begin{aligned} \tilde{\xi}_x &= \xi_x/J = y_\eta, & \tilde{\xi}_y &= \xi_y/J = -x_\eta, \\ \tilde{\eta}_x &= \eta_x/J = -y_\xi, & \tilde{\eta}_y &= \eta_y/J = x_\xi. \end{aligned} \quad (5.33)$$

We note that Equation (5.31) is hyperbolic as long as Equation (5.26) is hyperbolic.

If we equip the domain in the (ξ, η) -plane with a uniform mesh, we can solve Equation (5.31) using the method we described in the previous sections. In the course of doing that, we will need to compute the metric terms in Equation (5.33), which can be approximated using sufficiently high order central differences.

5.2 HLL type Riemann solvers for MHD equations

In this section, we describe several HLL type Riemann solvers for MHD equations, which we shall use in the alternative flux formulation of the WENO scheme. See Equation (5.22).

The HLL approximate Riemann solver was proposed by Harten, Lax, and van Leer [42]. This solver employs an approximate solution to the Riemann problem in which there is one intermediate state connected to the left and right states by discontinuities. This intermediate state is obtained by exploiting the conservation of the equations, which is called the

consistency condition in the literature. The HLL solver applies to any hyperbolic conservation law and does not make use of knowledge on the particular system. When applied to the Euler equations for hydrodynamics, the HLL solver exhibits excessive dissipation in the presence of contact discontinuities. To remedy this, Toro, Spruce, and Speares [88] proposed what is now known as the HLLC (C for contact) solver for the Euler’s equations. This solver assumes two intermediate states in the approximate solution, connected to each other by a contact discontinuity and to the left and right states by shocks. The Rankine-Hugoniot condition, in addition to the consistency condition, is used to determine the intermediate states.

Similar ideas were also applied to the ideal MHD equations in [40, 58, 64]. Gurski [40] and Li [58] named their solvers “HLLC” solvers for MHD, because they assume two intermediate states connected to each other by a contact discontinuity, as was the case in the HLLC solvers for the Euler’s equations. Miyoshi and Kusano [64] named their solver “HLLD” (D for discontinuities) solver, because their solver assumes four intermediate states and can exactly resolve most types of discontinuities in the ideal MHD equations, the only exception being the slow shocks. The HLLD solver is one of the two Riemann solvers we experiment when we explore the effects of the choice of Riemann solver in the alternative flux formulation of the WENO scheme, the other being Lax-Friedrichs. In [64], it is assumed that the normal vector to the discontinuity interface is parallel to one of the coordinate axes and that the magnetic field component normal to the discontinuity interface is the same at all points in space. Neither necessarily holds true in the problems we need the Riemann solver to handle. Curvilinear meshes demand that we consider Riemann problems with initial conditions (2.15) where the normal vector \mathbf{n} to discontinuity interface could be any direction. Multidimensional MHD problems allows for jumps in the normal magnetic field because divergence-free

condition can be saved by such jumps in other directions. We present our version of an HLLD solver that can handle these issues by dropping the assumptions on the direction \mathbf{n} and the normal magnetic field. Since the HLLD solver uses certain results obtained from the HLL and HLLC solvers, we first present these two simpler solvers in Sections 5.2.1 and 5.2.2. After that, we present the HLLD solver in Section 5.2.3.

5.2.1 The HLL approximate Riemann solver

Consider the Riemann problem given by the initial conditions (2.15). We use \mathbf{F} to denote the flux in the \mathbf{n} direction which we wrote as $\mathbf{n} \cdot \mathbb{F}$ in (2.6). We also introduce the notation

$$[a] = a_+ - a_- \tag{5.34}$$

to denote the jump of a quantity a across a discontinuity interface normal to \mathbf{n} , where a_+ is the value on the side that \mathbf{n} points to, and a_- is on the side that \mathbf{n} points from. For example, for the discontinuity in the initial conditions (2.15), $[\rho] = \rho_R - \rho_L$.

The approximate solution $\tilde{\mathbf{q}}$ employed in the HLL solver consists of three states, \mathbf{q}_R , \mathbf{q}_{HLL} , and \mathbf{q}_L , separated by two discontinuities propagating at wave speeds S_L and S_R , respectively, where $S_L \leq S_R$. In other words,

$$\tilde{\mathbf{q}}(t, \mathbf{x} \cdot \mathbf{n}) = \begin{cases} \mathbf{q}_L, & \text{if } (\mathbf{x} \cdot \mathbf{n})/t \leq S_L, \\ \mathbf{q}_{\text{HLL}}, & \text{if } S_L \leq (\mathbf{x} \cdot \mathbf{n})/t \leq S_R, \\ \mathbf{q}_R, & \text{if } S_R \leq (\mathbf{x} \cdot \mathbf{n})/t. \end{cases} \tag{5.35}$$

Here S_L and S_R are respectively the smallest and the largest of all the signal speeds, ap-

proximated by the smallest and largest among all wave speeds in \mathbf{q}_L and \mathbf{q}_R . The intermediate state \mathbf{q}_{HLL} is so defined that for all T , ξ_L , and ξ_R such that $T > 0$ and $\xi_L \leq \min(0, TS_L) \leq \max(0, TS_R) \leq \xi_R$, the *consistency condition*

$$\int_{\xi_L}^{\xi_R} \tilde{\mathbf{q}}(t, \xi) d\xi = \xi_R \mathbf{q}_R - \xi_L \mathbf{q}_L + T\mathbf{F}_L - T\mathbf{F}_R \quad (5.36)$$

is satisfied (see [86]). In the *subsonic* situation, where $S_L < 0 < S_R$, the consistency condition with $\xi_L = TS_L$ and $\xi_R = TS_R$ implies

$$\mathbf{q}_{\text{HLL}} = \frac{S_R \mathbf{q}_R - S_L \mathbf{q}_L + \mathbf{F}_L - \mathbf{F}_R}{S_R - S_L}. \quad (5.37)$$

The Godunov type numerical flux corresponding to this approximate solution is

$$\mathbf{F} = \begin{cases} \mathbf{F}_L, & \text{if } 0 \leq S_L, \\ \frac{S_R - S_L + S_L S_R (\mathbf{q}_R - \mathbf{q}_L)}{S_R - S_L}, & \text{if } S_L \leq 0 \leq S_R, \\ \mathbf{F}_R, & \text{if } S_R \leq 0. \end{cases} \quad (5.38)$$

5.2.2 The HLLC approximate Riemann solver

The HLLC approximate Riemann solver we present in this section was first proposed by Li in [58]. The approximate solution employed in this solver has two intermediate states

connected by a contact discontinuity. That is, the approximate solution is given by

$$\tilde{\mathbf{q}}(t, \mathbf{x} \cdot \mathbf{n}) = \begin{cases} \mathbf{q}_L, & \text{if } (\mathbf{x} \cdot \mathbf{n})/t \leq S_L, \\ \mathbf{q}_L^*, & \text{if } S_L \leq (\mathbf{x} \cdot \mathbf{n})/t \leq S_M, \\ \mathbf{q}_R^*, & \text{if } S_M \leq (\mathbf{x} \cdot \mathbf{n})/t \leq S_R, \\ \mathbf{q}_R, & \text{if } S_R \leq (\mathbf{x} \cdot \mathbf{n})/t, \end{cases} \quad (5.39)$$

where S_L and S_R are the estimated smallest and largest signal speeds, S_M is the estimated speed of the entropy wave (as well as that of the divergence wave), and \mathbf{q}_L^* and \mathbf{q}_R^* are some intermediate states to be determined. Once this approximate solution is determined, the corresponding Godunov type numerical flux is

$$\mathbf{F} = \begin{cases} \mathbf{F}_L, & \text{if } 0 \leq S_L, \\ \mathbf{F}_L^* = \mathbf{F}_L + S_L(\mathbf{q}_L^* - \mathbf{q}_L), & \text{if } S_L \leq 0 \leq S_M, \\ \mathbf{F}_R^* = \mathbf{F}_R + S_R(\mathbf{q}_R^* - \mathbf{q}_R), & \text{if } S_M \leq 0 \leq S_R, \\ \mathbf{F}_R, & \text{if } S_R \leq 0. \end{cases} \quad (5.40)$$

We now proceed to describe the approximate solution in the case where $S_L \leq 0 \leq S_R$. We mentioned before that the normal velocities and the total pressures do not change across a contact discontinuity in MHD. It is therefore reasonable to assume

$$\mathbf{u}_L^* \cdot \mathbf{n} = \mathbf{u}_R^* \cdot \mathbf{n} = S_M = \mathbf{u}_{HLL} \cdot \mathbf{n} \quad (5.41)$$

and

$$p_{\text{totL}}^* = p_{\text{totR}}^*. \quad (5.42)$$

We shall further make the assumption that

$$\mathbf{B}_L^* \cdot \mathbf{n} = \mathbf{B}_R^* \cdot \mathbf{n} = \mathbf{B}_{\text{HLL}} \cdot \mathbf{n}. \quad (5.43)$$

The Rankine-Hugoniot condition (2.17) across S_α , where α is either L or R, implies

$$S_\alpha \mathbf{q}_\alpha^* - \mathbf{F}_\alpha^* = S_\alpha \mathbf{q}_\alpha - \mathbf{F}_\alpha. \quad (5.44)$$

Equation (5.44) on ρ gives

$$S_\alpha \rho_\alpha^* - \rho_\alpha^* \mathbf{u}_\alpha^* \cdot \mathbf{n} = S_\alpha \rho_\alpha - \rho_\alpha \mathbf{u}_\alpha \cdot \mathbf{n}. \quad (5.45)$$

Therefore

$$\rho_\alpha^* = \rho_\alpha \frac{S_\alpha - \mathbf{u}_\alpha \cdot \mathbf{n}}{S_\alpha - S_M}, \quad (5.46)$$

in view of (5.41). Equation (5.44) on $\rho \mathbf{u}$ gives

$$\begin{aligned} & S_\alpha \rho_\alpha^* \mathbf{u}_\alpha^* - (\rho_\alpha^* (\mathbf{u}_\alpha^* \cdot \mathbf{n}) \mathbf{u}_\alpha^* + p_{\text{tot}\alpha}^* \mathbf{n} - (\mathbf{B}_\alpha^* \cdot \mathbf{n}) \mathbf{B}_\alpha^*) \\ &= S_\alpha \rho_\alpha \mathbf{u}_\alpha - (\rho_\alpha (\mathbf{u}_\alpha \cdot \mathbf{n}) \mathbf{u}_\alpha + p_{\text{tot}\alpha} \mathbf{n} - (\mathbf{B}_\alpha \cdot \mathbf{n}) \mathbf{B}_\alpha). \end{aligned} \quad (5.47)$$

Taking dot products of both sides of (5.47) with \mathbf{n} , we get

$$S_\alpha \rho_\alpha^* S_M - \rho_\alpha^* S_M^2 - p_{\text{tot}\alpha}^* + (\mathbf{B}_\alpha^* \cdot \mathbf{n})^2 = S_\alpha \rho_\alpha S_M - \rho_\alpha (\mathbf{u}_\alpha \cdot \mathbf{n})^2 - p_{\text{tot}\alpha} + (\mathbf{B}_\alpha \cdot \mathbf{n})^2. \quad (5.48)$$

From this and (5.46), we get

$$p_{\text{tot}\alpha}^* = p_{\text{tot}\alpha} + \rho_\alpha (S_\alpha - \mathbf{u}_\alpha \cdot \mathbf{n})(S_M - \mathbf{u}_\alpha \cdot \mathbf{n}) + (\mathbf{B}_\alpha^* \cdot \mathbf{n})^2 - (\mathbf{B}_\alpha \cdot \mathbf{n})^2. \quad (5.49)$$

Thus we are able to compute from (5.48) the momenta in the intermediate states,

$$\rho_\alpha^* \mathbf{u}_\alpha^* = \frac{\rho_\alpha (S_\alpha - \mathbf{u}_\alpha \cdot \mathbf{n}) + (p_{\text{tot}\alpha}^* - p_{\text{tot}\alpha}) \mathbf{n} + (\mathbf{B}_\alpha \cdot \mathbf{n}) \mathbf{B}_\alpha - (\mathbf{B}_\alpha^* \cdot \mathbf{n}) \mathbf{B}_\alpha^*}{S_\alpha - S_M} \quad (5.50)$$

To obtain the total energy \mathcal{E}_α in the intermediate states, we again use the Rankine-Hugoniot condition (5.44) across S_α . This time we get

$$\begin{aligned} & S_\alpha \mathcal{E}_\alpha^* - ((\mathcal{E}_\alpha^* + p_{\text{tot}\alpha}^*)(\mathbf{u}_\alpha^* \cdot \mathbf{n}) - (\mathbf{u}_\alpha^* \cdot \mathbf{B}_\alpha^*)(\mathbf{B}_\alpha^* \cdot \mathbf{n})) \\ &= S_\alpha \mathcal{E}_\alpha - ((\mathcal{E}_\alpha + p_{\text{tot}\alpha})(\mathbf{u}_\alpha \cdot \mathbf{n}) - (\mathbf{u}_\alpha \cdot \mathbf{B}_\alpha)(\mathbf{B}_\alpha \cdot \mathbf{n})). \end{aligned} \quad (5.51)$$

Solving for \mathcal{E}_α^* , we get

$$\frac{\mathcal{E}_\alpha (S_\alpha - \mathbf{u}_\alpha \cdot \mathbf{n}) + p_{\text{tot}\alpha}^* S_M - p_{\text{tot}\alpha} (\mathbf{u}_\alpha \cdot \mathbf{n}) + (\mathbf{B}_\alpha \cdot \mathbf{n})(\mathbf{B}_\alpha \cdot \mathbf{u}_\alpha) - (\mathbf{B}_\alpha^* \cdot \mathbf{n})(\mathbf{B}_\alpha^* \cdot \mathbf{u}_\alpha^*)}{S_\alpha - S_M}. \quad (5.52)$$

We still need to determine \mathbf{B}_α^* in (5.50) and (5.52). We shall use the consistency condition, which in the current context takes the form

$$\frac{S_M - S_L}{S_R - S_L} \mathbf{q}_L^* + \frac{S_R - S_M}{S_R - S_L} \mathbf{q}_R^* = \mathbf{q}_{\text{HLL}}. \quad (5.53)$$

Apply (5.53) and (5.37) to $\rho\mathbf{u}$ and simplify with (5.42) taken into account, and we get

$$-(\mathbf{B}_R^* \cdot \mathbf{n})\mathbf{B}_R^* + (\mathbf{B}_L^* \cdot \mathbf{n})\mathbf{B}_L^* = 0. \quad (5.54)$$

In view of (5.43), it is reasonable to set

$$\mathbf{B}_L^* = \mathbf{B}_R^* = \mathbf{B}_{\text{HLL}}. \quad (5.55)$$

Now the intermediate states in the approximate solution are completely determined in (5.41), (5.43), (5.46), (5.49), (5.55), (5.50), and (5.52). Li [58] noted that if the Rankine-Hugoniot condition (5.44) on \mathbf{B} were used in place of the consistency condition (5.53) on $\rho\mathbf{u}$ to get \mathbf{B}_α , the consistency condition will be violated and instabilities will happen.

5.2.3 The HLLD approximate Riemann solver

The approximate solution employed in the HLLD solver has four intermediate states, connected by two rotational discontinuities and one contact or tangential discontinuity. In other words,

$$\tilde{\mathbf{q}}(t, \mathbf{x} \cdot \mathbf{n}) = \begin{cases} \mathbf{q}_L, & \text{if } (\mathbf{x} \cdot \mathbf{n})/t \leq S_L, \\ \mathbf{q}_L^*, & \text{if } S_L \leq (\mathbf{x} \cdot \mathbf{n})/t \leq S_L^*, \\ \mathbf{q}_L^{**}, & \text{if } S_L^* \leq (\mathbf{x} \cdot \mathbf{n})/t \leq S_M, \\ \mathbf{q}_R^{**}, & \text{if } S_M \leq (\mathbf{x} \cdot \mathbf{n})/t \leq S_R^*, \\ \mathbf{q}_R^*, & \text{if } S_R^* \leq (\mathbf{x} \cdot \mathbf{n})/t \leq S_R, \\ \mathbf{q}_R, & \text{if } S_R \leq (\mathbf{x} \cdot \mathbf{n})/t, \end{cases} \quad (5.56)$$

where S_L and S_R are estimated fast shock speeds, S_L^* and S_R^* are estimated speeds of the rotational discontinuities, and S_M is the estimated speed of the contact or tangential discontinuity. The corresponding Godunov type numerical flux is

$$\mathbf{F} = \begin{cases} \mathbf{F}_L, & \text{if } 0 \leq S_L, \\ \mathbf{F}_L^* = \mathbf{F}_L + S_L \mathbf{q}_L^* - S_L \mathbf{q}_L, & \text{if } S_L \leq 0 \leq S_L^*, \\ \mathbf{F}_L^{**} = \mathbf{F}_L + S_L^* \mathbf{q}_L^{**} - (S_L^* - S_L) \mathbf{q}_L^* - S_L \mathbf{q}_L, & \text{if } S_L^* \leq 0 \leq S_M, \\ \mathbf{F}_R^{**} = \mathbf{F}_R + S_R^* \mathbf{q}_R^{**} - (S_R^* - S_R) \mathbf{q}_R^* - S_R \mathbf{q}_R, & \text{if } S_M \leq 0 \leq S_R^*, \\ \mathbf{F}_R^* = \mathbf{F}_R + S_R \mathbf{q}_R^* - S_R \mathbf{q}_R, & \text{if } S_R^* \leq 0 \leq S_R, \\ \mathbf{F}_R, & \text{if } S_R \leq 0. \end{cases} \quad (5.57)$$

We now proceed to describe the approximate solution in the case where $S_L \leq 0 \leq S_R$. Similar to the assumptions (5.41), (5.42), and (5.43) made in HLLC solver, we assume

$$\mathbf{u}_L^* \cdot \mathbf{n} = \mathbf{u}_L^{**} \cdot \mathbf{n} = \mathbf{u}_R^{**} \cdot \mathbf{n} = \mathbf{u}_R^* \cdot \mathbf{n} = S_M = \mathbf{u}_{\text{HLL}} \cdot \mathbf{n}, \quad (5.58)$$

$$p_{\text{tot}_L}^* = p_{\text{tot}_L}^{**} = p_{\text{tot}_R}^{**} = p_{\text{tot}_R}^*, \quad (5.59)$$

and

$$\mathbf{B}_L^* \cdot \mathbf{n} = \mathbf{B}_L^{**} \cdot \mathbf{n} = \mathbf{B}_R^{**} \cdot \mathbf{n} = \mathbf{B}_R^* \cdot \mathbf{n} = \mathbf{B}_{\text{HLL}} \cdot \mathbf{n}. \quad (5.60)$$

Recall that rotational discontinuities are linearly degenerate and correspond to the Alfvén waves, which propagate at speeds $\mathbf{u} \cdot \mathbf{n} \mp \sqrt{(\mathbf{B} \cdot \mathbf{n})^2 / \rho}$. Since $[\rho] = 0$ across rotational

discontinuities, we can set

$$S_L^* = S_M - \sqrt{\frac{(\mathbf{B}_{\text{HLL}} \cdot \mathbf{n})^2}{\rho_L^*}} \quad (5.61)$$

and

$$S_R^* = S_M + \sqrt{\frac{(\mathbf{B}_{\text{HLL}} \cdot \mathbf{n})^2}{\rho_R^*}}, \quad (5.62)$$

where ρ_α^* can be obtained by using the Rankine-Hugoniot condition (5.44) on ρ across S_α , which gives

$$\rho_\alpha^* = \rho_\alpha \frac{S_\alpha - \mathbf{u}_\alpha \cdot \mathbf{n}}{S_\alpha - S_M}, \quad (5.63)$$

the same as (5.46). The four-intermediate-state approximate solution (5.56) degenerates to a two-intermediate-state solution when S_L^* and S_R^* are either too close to S_L and S_R , respectively, or when they are too close to S_M . In both cases, we fall back to the HLLC solver and forego what we describe below.

We now consider the non-degenerate case where S_L , S_L^* , S_L^{**} , S_M , S_R^{**} , S_R^* , and S_R are sufficiently spread apart. The state \mathbf{q}_α^* is obtained from the Rankine-Hugoniot condition across S_α . The value of ρ_α^* was given in (5.63). Equations (5.49) and (5.50) in HLLC remain valid in the current context. We repeat them here:

$$p_{\text{tot}\alpha}^* = p_{\text{tot}\alpha} + \rho_\alpha (S_\alpha - \mathbf{u}_\alpha \cdot \mathbf{n}) (S_M - \mathbf{u}_\alpha \cdot \mathbf{n}) + (\mathbf{B}_\alpha^* \cdot \mathbf{n})^2 - (\mathbf{B}_\alpha \cdot \mathbf{n})^2, \quad (5.64)$$

$$\rho_\alpha^* \mathbf{u}_\alpha^* = \frac{\rho_\alpha (S_\alpha - \mathbf{u}_\alpha \cdot \mathbf{n}) + (p_{\text{tot}\alpha}^* - p_{\text{tot}\alpha}) \mathbf{n} + (\mathbf{B}_\alpha \cdot \mathbf{n}) \mathbf{B}_\alpha - (\mathbf{B}_\alpha^* \cdot \mathbf{n}) \mathbf{B}_\alpha^*}{S_\alpha - S_M}. \quad (5.65)$$

Now apply the Rankine-Hugoniot condition across S_α on \mathbf{B} , which gives

$$S_\alpha \mathbf{B}_\alpha^* - ((\mathbf{u} \cdot \mathbf{n})\mathbf{B} - (\mathbf{B} \cdot \mathbf{n})\mathbf{u})_\alpha^* = S_\alpha \mathbf{B}_\alpha - ((\mathbf{u} \cdot \mathbf{n})\mathbf{B} - (\mathbf{B} \cdot \mathbf{n})\mathbf{u})_\alpha. \quad (5.66)$$

With $\mathbf{u}_\alpha^* \cdot \mathbf{n}$ given by (5.58), $\mathbf{B}_\alpha^* \cdot \mathbf{n}$ given by (5.60), ρ_α^* given by (5.63), and $p_{\text{tot}\alpha}^*$ given by (5.64), we see that (5.65) and (5.66) form a linear system of (algebraic) equations in \mathbf{u}_α^* and \mathbf{B}_α^* . The solution to this system is

$$\begin{aligned} \mathbf{u}_\alpha^* = & \frac{\rho_\alpha(S_\alpha - \mathbf{u}_\alpha \cdot \mathbf{n})(S_\alpha - S_M) - (\mathbf{B}_{\text{HLL}} \cdot \mathbf{n})(\mathbf{B}_\alpha \cdot \mathbf{n})}{\rho_\alpha(S_\alpha - \mathbf{u}_\alpha \cdot \mathbf{n})(S_\alpha - S_M) - (\mathbf{B}_{\text{HLL}} \cdot \mathbf{n})^2} \mathbf{u}_\alpha \\ & + \frac{(p_{\text{tot}\alpha}^* - p_{\text{tot}\alpha})(S_\alpha - S_M)}{\rho_\alpha(S_\alpha - \mathbf{u}_\alpha \cdot \mathbf{n})(S_\alpha - S_M) - (\mathbf{B}_{\text{HLL}} \cdot \mathbf{n})^2} \mathbf{n} \\ & + \frac{(\mathbf{B}_\alpha \cdot \mathbf{n})(S_\alpha - S_M) - (\mathbf{B}_{\text{HLL}} \cdot \mathbf{n})(S_\alpha - \mathbf{u}_\alpha \cdot \mathbf{n})}{\rho_\alpha(S_\alpha - \mathbf{u}_\alpha \cdot \mathbf{n})(S_\alpha - S_M) - (\mathbf{B}_{\text{HLL}} \cdot \mathbf{n})^2} \mathbf{B}_\alpha \end{aligned} \quad (5.67)$$

and

$$\begin{aligned} \mathbf{B}_\alpha^* = & \frac{\rho_\alpha(S_\alpha - \mathbf{u}_\alpha \cdot \mathbf{n})^2 - (\mathbf{B}_{\text{HLL}} \cdot \mathbf{n})(\mathbf{B}_\alpha \cdot \mathbf{n})}{\rho_\alpha(S_\alpha - \mathbf{u}_\alpha \cdot \mathbf{n})(S_\alpha - S_M) - (\mathbf{B}_{\text{HLL}} \cdot \mathbf{n})^2} \mathbf{B}_\alpha \\ & + \frac{\rho_\alpha(S_\alpha - \mathbf{u}_\alpha \cdot \mathbf{n})(\mathbf{B}_\alpha \cdot \mathbf{n} - \mathbf{B}_{\text{HLL}} \cdot \mathbf{n})}{\rho_\alpha(S_\alpha - \mathbf{u}_\alpha \cdot \mathbf{n})(S_\alpha - S_M) - (\mathbf{B}_{\text{HLL}} \cdot \mathbf{n})^2} \mathbf{u}_\alpha \\ & - \frac{(p_{\text{tot}\alpha}^* - p_{\text{tot}\alpha})(\mathbf{B}_{\text{HLL}} \cdot \mathbf{n})}{\rho_\alpha(S_\alpha - \mathbf{u}_\alpha \cdot \mathbf{n})(S_\alpha - S_M) - (\mathbf{B}_{\text{HLL}} \cdot \mathbf{n})^2} \mathbf{n}. \end{aligned} \quad (5.68)$$

Using the Rankine-Hugoniot condition across S_α on \mathcal{E} , we can obtain

$$\mathcal{E}_\alpha^* = \frac{\mathcal{E}_\alpha(S_\alpha - \mathbf{u}_\alpha \cdot \mathbf{n}) + p_{\text{tot}\alpha}^* S_M - p_{\text{tot}\alpha}(\mathbf{u}_\alpha \cdot \mathbf{n}) + (\mathbf{B}_\alpha \cdot \mathbf{n})(\mathbf{B}_\alpha \cdot \mathbf{u}_\alpha) - (\mathbf{B}_\alpha^* \cdot \mathbf{n})(\mathbf{B}_\alpha^* \cdot \mathbf{u}_\alpha^*)}{S_\alpha - S_M}, \quad (5.69)$$

which has the same form as (5.52). We note that whereas in the HLLC solver we used consistency condition (5.53) on $\rho\mathbf{u}$ to obtain a equation for \mathbf{B}_α^* (5.55), in the HLLD solver

we used the Rankine-Hugoniot condition across S_α on $\rho\mathbf{u}$ and \mathbf{B} to get $\rho\mathbf{u}_\alpha^*$ and \mathbf{B}_α^* , and save a consistency condition similar to (5.53) for determining $(\rho\mathbf{u})_\alpha^{**}$ and \mathbf{B}_α^{**} in the two inner intermediate states.

We now proceed to find the values of the inner intermediate states \mathbf{q}_α^{**} . The Rankine-Hugoniot condition across S_α^* on ρ gives

$$S_\alpha^* \rho_\alpha^{**} - (\rho\mathbf{u})_\alpha^{**} \cdot \mathbf{n} = S_\alpha^* \rho_\alpha^* - (\rho\mathbf{u})_\alpha^* \cdot \mathbf{n}. \quad (5.70)$$

Solve (5.70) with (5.58) taken into account, we get

$$\rho_\alpha^{**} = \rho_\alpha^*. \quad (5.71)$$

Note that this is consistent with the fact that $[\rho] = 0$ across a rotational discontinuity, which we assumed in deriving the estimates of S_L^* and S_R^* in (5.61) and (5.62).

Since we have been considering the case where S_L , S_L^* , S_L^{**} , S_M , S_R^{**} , S_R^* , and S_R are sufficiently spread apart, we can assume that

$$\mathbf{B}_{\text{HLL}} \cdot \mathbf{n} \neq 0, \quad (5.72)$$

in view of (5.61) and (5.62). Under the assumption (5.72), the Rankine-Hugoniot condition across S_M on $\rho\mathbf{u}$ implies

$$\mathbf{B}_L^{**} = \mathbf{B}_R^{**} \quad (5.73)$$

and the same condition on \mathbf{B} implies

$$\mathbf{u}_L^{**} = \mathbf{u}_R^{**}. \quad (5.74)$$

The consistency condition (consistency with the integral conservation law) in the current context takes the form

$$(S_R - S_R^*)\mathbf{q}_R^* + (S_R^* - S_M)\mathbf{q}_R^{**} + (S_M - S_L^*)\mathbf{q}_L^{**} + (S_L^* - S_L)\mathbf{q}_L^* - S_R\mathbf{q}_R + S_L\mathbf{q}_L + \mathbf{F}_R - \mathbf{F}_L = 0. \quad (5.75)$$

We regroup the terms in (5.75) and get

$$\begin{aligned} & (S_R^* - S_M)\mathbf{q}_R^{**} + (S_M - S_L^*)\mathbf{q}_L^{**} + (S_R(\mathbf{q}_R^* - \mathbf{q}_R) + \mathbf{F}_R) - (S_L(\mathbf{q}_L^* - \mathbf{q}_L) + \mathbf{F}_L) \\ & - S_R^*\mathbf{q}_R^* + S_L^*\mathbf{q}_L^* = 0. \end{aligned} \quad (5.76)$$

The Rankine-Hugoniot condition (2.17) across S_α^* gives

$$S_\alpha(\mathbf{q}_\alpha^* - \mathbf{q}_\alpha) = \mathbf{F}_\alpha^* - \mathbf{F}_\alpha \quad (5.77)$$

Substitute (5.61), (5.62), (5.77) into (5.76), and we get

$$|\mathbf{B}_{\text{HLL}} \cdot \mathbf{n}| \left(\frac{\mathbf{q}_R^{**}}{\sqrt{\rho_R^*}} + \frac{\mathbf{q}_L^{**}}{\sqrt{\rho_L^*}} \right) + \mathbf{F}_R^* - \mathbf{F}_L^* - S_R^*\mathbf{q}_R^* + S_L^*\mathbf{q}_L^* = 0. \quad (5.78)$$

Applying (5.78) to $\rho\mathbf{u}$ with (5.71) and (5.74) taken into account, we get

$$\begin{aligned} & |\mathbf{B}_{\text{HLL}} \cdot \mathbf{n}| \left(\sqrt{\rho_R^*} + \sqrt{\rho_L^*} \right) \mathbf{u}_\alpha^{**} + ((\mathbf{u} \cdot \mathbf{n})\rho\mathbf{u} + p_{\text{tot}}\mathbf{n} - (\mathbf{B} \cdot \mathbf{n})\mathbf{B})_R^* \\ & - ((\mathbf{u} \cdot \mathbf{n})\rho\mathbf{u} + p_{\text{tot}}\mathbf{n} - (\mathbf{B} \cdot \mathbf{n})\mathbf{B})_L^* - S_R^*(\rho\mathbf{u})_R^* + S_L^*(\rho\mathbf{u})_L^* = 0. \end{aligned} \quad (5.79)$$

Solving for \mathbf{u}_α^{**} with (5.58), (5.59), (5.60), (5.61), and (5.62) taken into account gives

$$\mathbf{u}_\alpha^{**} = \frac{\sqrt{\rho_L^*} \mathbf{u}_L^* + \sqrt{\rho_R^*} \mathbf{u}_R^* + \text{sign}(\mathbf{B}_{\text{HLL}} \cdot \mathbf{n})(\mathbf{B}_R^* - \mathbf{B}_L^*)}{\sqrt{\rho_L^*} + \sqrt{\rho_R^*}}. \quad (5.80)$$

Applying (5.78) to \mathbf{B} with (5.73) taken into account gives

$$\begin{aligned} & |\mathbf{B}_{\text{HLL}} \cdot \mathbf{n}| \left(\frac{1}{\sqrt{\rho_R^*}} + \frac{1}{\sqrt{\rho_L^*}} \right) \mathbf{B}_\alpha^{**} + ((\mathbf{u} \cdot \mathbf{n})\mathbf{B} - (\mathbf{B} \cdot \mathbf{n})\mathbf{u})_R^* \\ & - ((\mathbf{u} \cdot \mathbf{n})\mathbf{B} - (\mathbf{B} \cdot \mathbf{n})\mathbf{u})_L^* - S_R^* \mathbf{B}_R^* + S_L^* \mathbf{B}_L^* = 0. \end{aligned} \quad (5.81)$$

Solving for \mathbf{B}_α^{**} with (5.58), (5.60), (5.61), and (5.62) taken into account gives

$$\mathbf{B}_\alpha^{**} = \frac{\sqrt{\rho_R^*} \mathbf{B}_L^* + \sqrt{\rho_L^*} \mathbf{B}_R^* + \text{sign}(\mathbf{B}_{\text{HLL}} \cdot \mathbf{n}) \sqrt{\rho_L^* \rho_R^*} (\mathbf{u}_R^* - \mathbf{u}_L^*)}{\sqrt{\rho_L^*} + \sqrt{\rho_R^*}}. \quad (5.82)$$

The Rankine-Hugoniot condition across S_α^* on \mathcal{E} gives

$$S_\alpha^* \mathcal{E}_\alpha^{**} - ((\mathcal{E} + p_{\text{tot}})(\mathbf{u} \cdot \mathbf{n}) - (\mathbf{u} \cdot \mathbf{B})(\mathbf{B} \cdot \mathbf{n}))_\alpha^{**} = S_\alpha^* \mathcal{E}_\alpha^* - ((\mathcal{E} + p_{\text{tot}})(\mathbf{u} \cdot \mathbf{n}) - (\mathbf{u} \cdot \mathbf{B})(\mathbf{B} \cdot \mathbf{n}))_\alpha^*. \quad (5.83)$$

Solving for \mathcal{E}_α^{**} with (5.58), (5.59), (5.60), (5.61), and (5.62) taken into account gives

$$\mathcal{E}_\alpha^{**} = \mathcal{E}_\alpha^* \mp \sqrt{\rho_\alpha^*} (\mathbf{u}_\alpha^* \cdot \mathbf{B}_\alpha^* - \mathbf{u}_\alpha^{**} \cdot \mathbf{B}_\alpha^{**}) \text{sign}(\mathbf{B}_{\text{HLL}} \cdot \mathbf{n}), \quad (5.84)$$

where $-$ and $+$ corresponds to $\alpha = \text{L}$ and $\alpha = \text{R}$, respectively.

Now the intermediate states in the approximate solution are completely determined in (5.58), (5.59), (5.60), (5.61), (5.62), (5.63), (5.64), (5.67), (5.68), (5.69), (5.71), (5.73),

(5.74), (5.80), (5.82), and (5.84).

5.3 Constrained transport

In our current scheme, we use the same constrained transport framework as in Section 4.1 to control the divergence error of the magnetic field. Namely, we evolve a vector potential \mathbf{A} , which satisfies (4.1)

$$\mathbf{B} = \nabla \times \mathbf{A}.$$

The evolution equation is given by (4.7)

$$\partial_t \mathbf{A} + (\nabla \times \mathbf{A}) \times \mathbf{u} = 0.$$

In the current multistage setting, we set

$$\mathbf{B} = \nabla \times \mathbf{A}$$

after each stage in the time integrator.

As explained in Section 4.3.1, in the case of two spatial dimensions, the divergence-free condition becomes (4.19)

$$\nabla \cdot \mathbf{B} = \partial_x B^x + \partial_y B^y = 0,$$

where B^z does not play any role. It therefore suffices to correct only B^x and B^y in 2D, which can be done by evolving A^z according to (4.20)

$$\partial_t A^z + u^x \partial_x A^z + u^y \partial_y A^z = 0$$

and correcting B^x and B^y through (4.21)

$$B^x = \partial_y A^z, \quad B^y = -\partial_x A^z.$$

In the current multistage scheme, Equation (4.20) is solved by a WENO method for Hamilton-Jacobi equations in the same way as in [23]. The magnetic field correction (4.21) is discretized by using fourth-order accuracy central differences, also in the same way as in [23].

Constrained transport on curvilinear meshes is done similarly. In the curvilinear coordinates, Equation (4.20) becomes

$$\partial_t A^z + J(u^x \tilde{\xi}_x + u^y \tilde{\xi}_y) \partial_\xi A^z + J(u^x \tilde{\eta}_x + u^y \tilde{\eta}_y) \partial_\eta A^z = 0 \quad (5.85)$$

and Equation (4.21) becomes

$$B^x = J(\tilde{\xi}_y \partial_\xi A^z + \tilde{\eta}_y \partial_\eta A^z), \quad B^y = -J(\tilde{\xi}_x \partial_\xi A^z + \tilde{\eta}_x \partial_\eta A^z). \quad (5.86)$$

Equation (5.85) is solved by a WENO method for Hamilton-Jacobi equations and Equation (5.86) is discretized by using fourth-order accuracy central differences. We note that while such discretization only guarantees the divergence-free condition of magnetic field to truncation errors, in practice we find this is sufficient to suppress the unphysical oscillations associated with the divergence error of \mathbf{B} .

5.4 A positivity-preserving limiter

When we apply the current scheme with the HLLD Riemann solver, we find it necessary to apply a positivity-preserving limiter similar to the one described in Section 4.4. This is possibly due to the enhanced resolution provided by the HLLD solver. We encountered a similar situation in Section 4.5.5.2, where a finer mesh reveals a region of low pressure not resolved in coarser meshes.

The positivity-preserving limiter goes mostly the same as the limiter in Section 4.4. The differences are as follows.

1. On a curvilinear mesh, the equation actually being solved is given by (5.31). Therefore the expressions for the updates and fluxes in Section 4.4 need to be modified accordingly.
2. In the current multistage scheme, the procedure described in Section 4.4 is to be applied at each stage. We note that while it is suggested in [22] that it is sufficient to apply the limiter only at the final stage of each time step, we find it necessary to apply it at each stage in the current scheme. This, again, is possibly due to the enhanced resolution provided by the HLLD solver.
3. We have used \mathbf{f} and \mathbf{g} to denote the high order fluxes in the current chapter. In Chapter 4, however, we used \mathbf{F} and \mathbf{G} to denote the high-order time-averaged fluxes and \mathbf{f} and \mathbf{g} to denote the low-order fluxes. It should be clear how to translate the description in Section 4.4 into a description with the notations in the current chapter.

5.5 Numerical results

5.5.1 2D smooth Alfvén wave problem

We use the smooth Alfvén wave problem to test the order of convergence of our numerical scheme. The initial conditions were given in (4.65) as

$$\begin{aligned} &(\rho, u^x, u^y, u^z, p, B^x, B^y, B^z)(0, x) \\ &= (1, 0, 0.1 \sin(2\pi x), 0.1 \cos(2\pi x), 0.1, 1, 0.1 \sin(2\pi x), 0.1 \cos(2\pi x)). \end{aligned}$$

The exact solution propagates with the Alfvén speed, which equals 1 (i.e., $\mathbf{q}(t, x) = \mathbf{q}(0, x + t)$).

In Section 4.5.1 we rotated the direction of Alfvén wave propagation so that it is not parallel to any mesh lines. In the current section, we keep the direction of wave propagation parallel to the x -axis and tweak the mesh to achieve the same effect.

The computational domain is set to be $(\xi, \eta) \in [0, 1]^2$, with the mesh lines perturbed according to

$$\begin{aligned} x &= \xi + \epsilon_x \sin(2\pi\eta a_x), \\ y &= \eta + \epsilon_y \sin(2\pi\xi a_y), \end{aligned} \tag{5.87}$$

where ϵ_x and ϵ_y are the magnitude of perturbation and a_x and a_y are the wave numbers of the perturbation. In the results we show below, we use $\epsilon_x = 0.01$, $\epsilon_y = 0.02$, $a_x = 2$, and $a_y = 4$. As an illustration, we plot a 32×32 mesh with these parameters in Figure 5.2.

In Tables 5.1 and 5.2, we present the L^∞ -errors in \mathbf{B} and A^z , obtained using the alternative WENO method with the Lax-Friedrichs flux and with the HLLD flux, respectively. These results confirm that our method has fourth order of accuracy. We note that for this

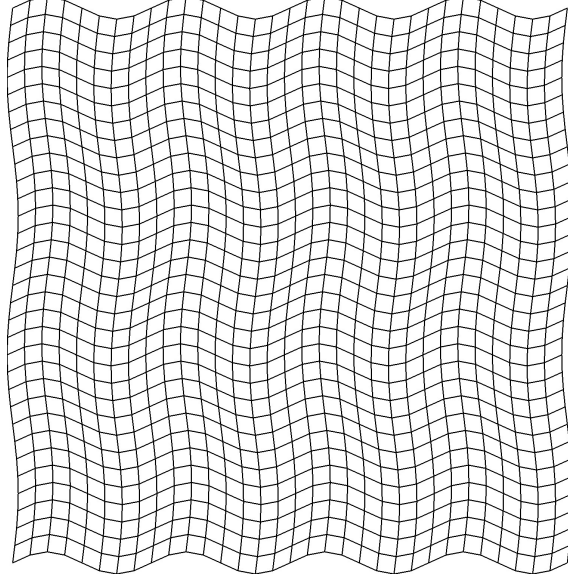


Figure 5.2: Perturbed mesh used for 2D Alfvén problem. 32×32 mesh. $(\xi, \eta) \in [0, 1]^2$. $x = \xi + 0.01 \sin(2\pi\eta \cdot 2)$, $y = \eta + 0.02 \sin(2\pi\xi \cdot 4)$.

Mesh	Error in \mathbf{B}	Order	Error in A^z	Order
32×32	5.131×10^{-3}	—	1.560×10^{-4}	—
64×64	4.090×10^{-4}	3.65	8.394×10^{-6}	4.22
128×128	2.658×10^{-5}	3.94	5.266×10^{-7}	3.99
256×256	1.677×10^{-6}	3.99	3.322×10^{-8}	3.99

Table 5.1: L^∞ -errors in 2D smooth Alfvén problem. Alternative WENO with Lax-Friedrichs flux. Constrained transport and positivity-preserving limiter on.

smooth problem, the difference between using the Lax-Friedrichs flux and the HLLD flux is very small.

5.5.2 Brio-Wu shock tube

This is a frequently tested Riemann problem. The initial conditions are as given in (4.68),

$$(\rho, u^x, u^y, u^z, p, B^x, B^y, B^z) = \begin{cases} (1, 0, 0, 0, 1, 0.75, 1, 0) & \text{if } x < 0, \\ (0.125, 0, 0, 0, 0.1, 0.75, -1, 0) & \text{if } x \geq 0. \end{cases} \quad (5.88)$$

Mesh	Error in \mathbf{B}	Order	Error in A^z	Order
32×32	5.257×10^{-3}	—	1.604×10^{-4}	—
64×64	4.090×10^{-4}	3.68	8.388×10^{-6}	4.26
128×128	2.658×10^{-5}	3.94	5.264×10^{-7}	3.99
256×256	1.677×10^{-6}	3.99	3.322×10^{-8}	3.99

Table 5.2: L^∞ -errors in 2D smooth Alfvén problem. Alternative WENO with HLLD flux. Constrained transport and positivity-preserving limiter on.

In Section 5.5.2.1, we run our scheme on both uniform and non-uniform 1D meshes, so as to test its handling of shocks across abrupt changes in mesh spacing. In Section 5.5.2.2, we run our scheme on a 2D mesh, with the initial conditions rotated, so as to test the handling of shocks and control of divergence error of the magnetic field.

5.5.2.1 1D shock tube

In Figures 5.3–5.6, we present plots of the density and the transverse magnetic field using various setups of 1D simulations. In all results, we have used meshes of 200 points. The meshes in Figures 5.3 and 5.4 are uniform. The meshes in Figures 5.5 and 5.6 are determined by

$$x = \begin{cases} \frac{10}{9}\xi & \text{if } |\xi| \leq 0.2, \\ \text{sign}(\xi) \left(\frac{2}{9} + \frac{20}{9} (|\xi| - 0.2) \right) & \text{otherwise,} \end{cases} \quad (5.89)$$

with $-1 \leq \xi \leq 1$. We note that both the alternative WENO methods with Lax-Friedrichs flux and with the HLLD flux can handle the abrupt change in the spacing in the non-uniform cases without introducing too much oscillations.

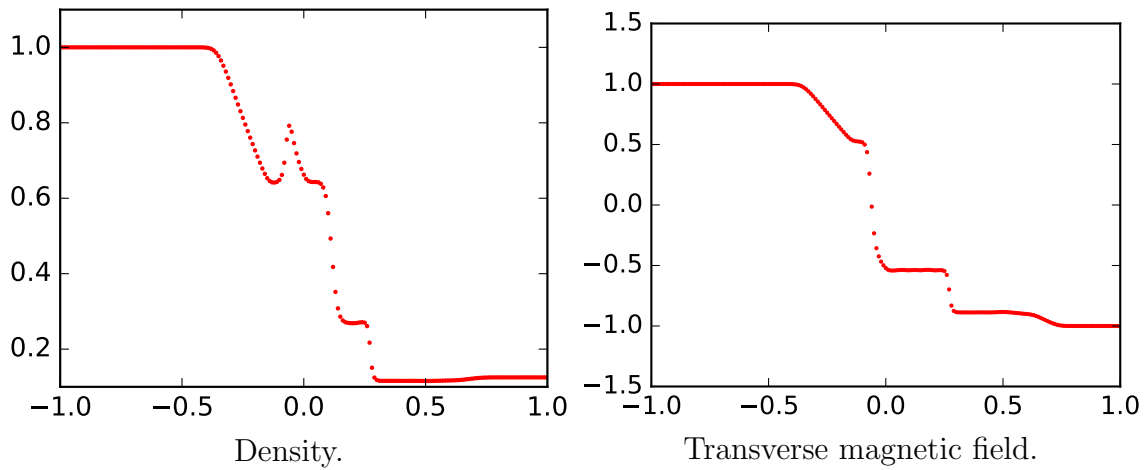


Figure 5.3: Brio-Wu shock tube. $t = 0.2$. Alternative WENO with Lax-Friedrichs flux. A uniform mesh of 200 points were used. Positivity-preserving limiter is turned on.

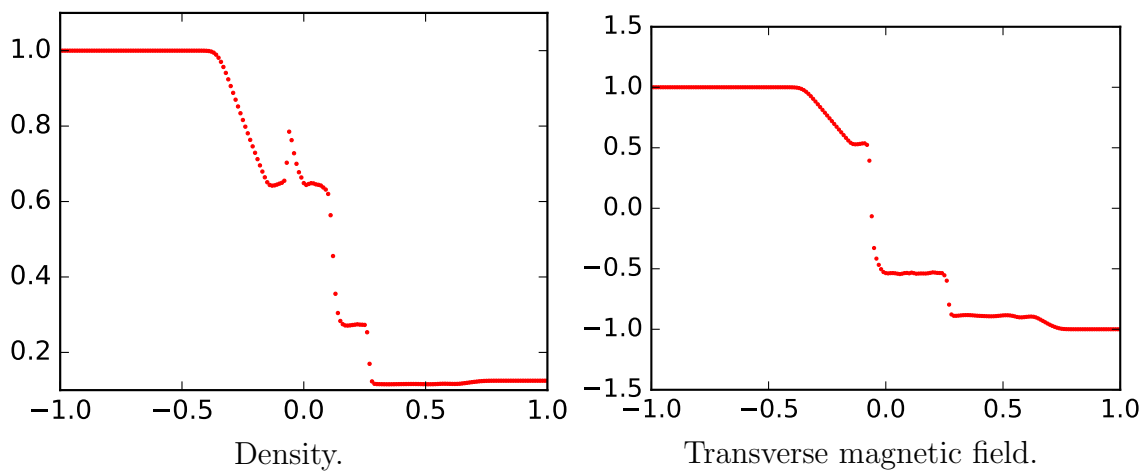


Figure 5.4: Brio-Wu shock tube. $t = 0.2$. Alternative WENO with HLLD flux. A uniform mesh of 200 points were used. Positivity-preserving limiter is turned on.

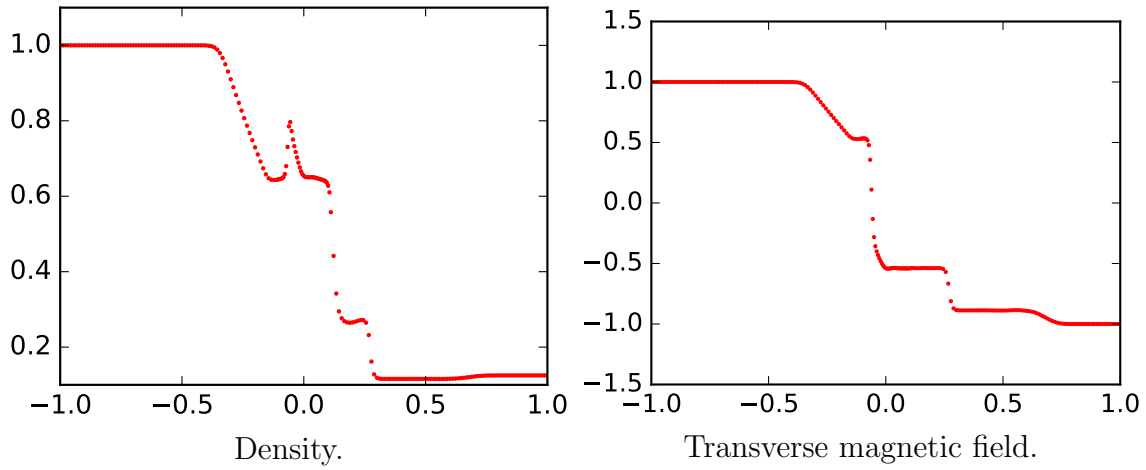


Figure 5.5: Brio-Wu shock tube. $t = 0.2$. Alternative WENO with Lax-Friedrichs flux. A non-uniform mesh of 200 points were used. Positivity-preserving limiter is turned on.

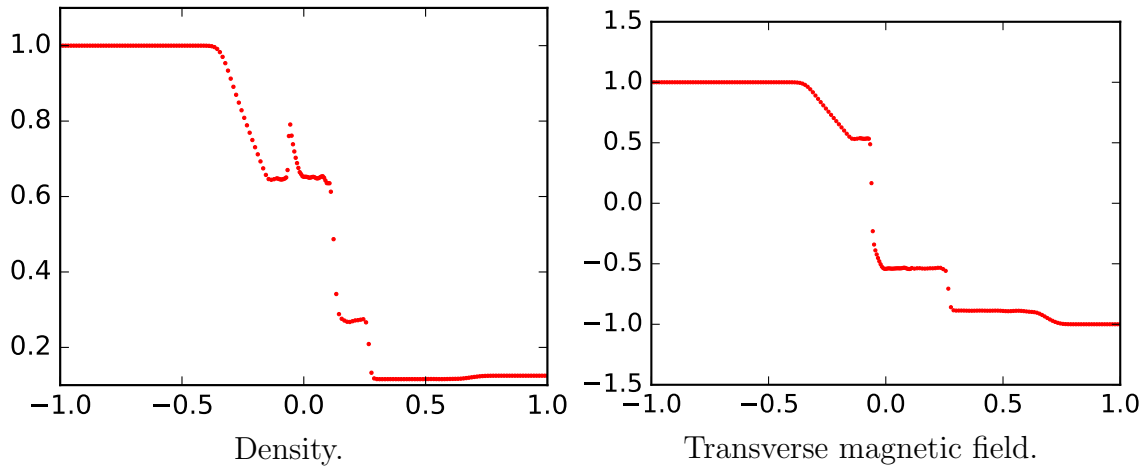


Figure 5.6: Brio-Wu shock tube. $t = 0.2$. Alternative WENO with HLLD flux. A non-uniform mesh of 200 points were used. Positivity-preserving limiter is turned on.

5.5.2.2 2D rotated shock tube

We also run the Brio-Wu shock tube test on 2D meshes. In all the results presented in this section, we use a 200×100 uniform mesh on the domain $[-1, 1] \times [-0.5, 0.5]$. We have rotated the initial condition by an angle of $\tan^{-1}(0.5)$. In this setup, the enforcing of the divergence-free condition becomes crucial. Without the constrained transport, the simulation using alternative WENO with HLLD flux crashes before t reaches 0.2, whereas the simulation using alternative WENO with Lax-Friedrichs flux demonstrates excessive unphysical oscillations, which can be seen from the plots in 5.7. On the other hand, the plots in Figures 5.8 and 5.9 show that turning on constrained transport can satisfactorily control the unphysical oscillations.

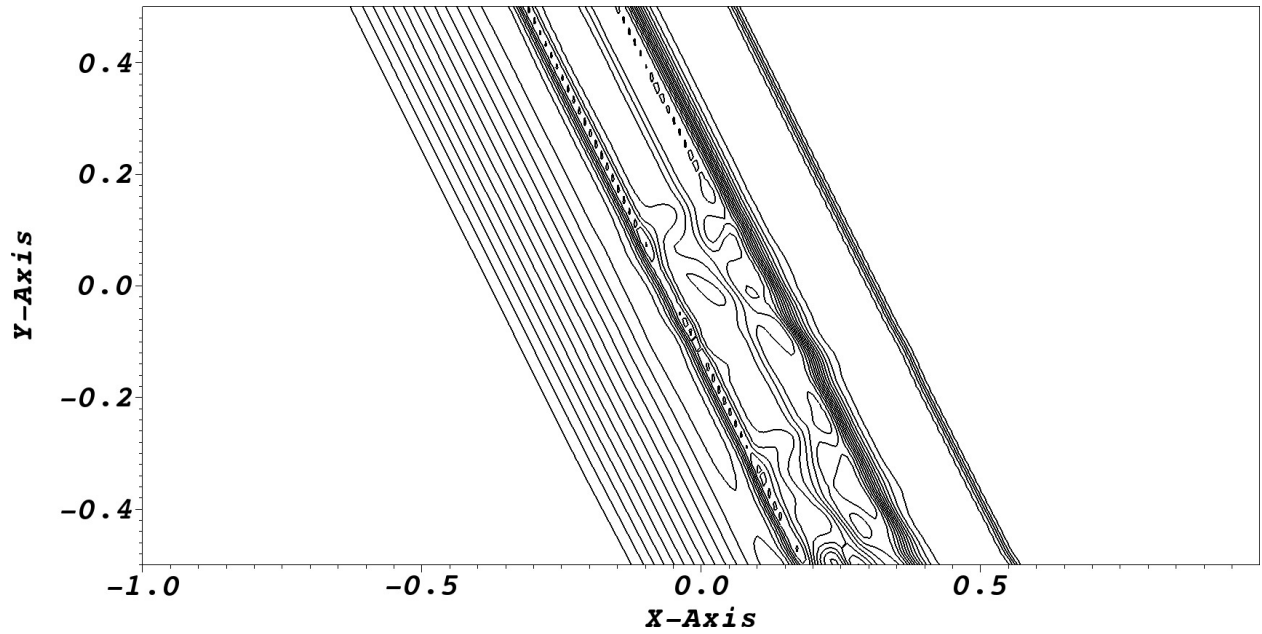
5.5.3 2D Orszag-Tang vortex

In this section, we test our scheme on the 2D Orszag-Tang vortex problem, which we investigated in Section 4.5.3 with our first scheme. The initial conditions were given in (4.72),

$$\rho = \gamma^2, \quad \mathbf{u} = (-\sin(y), \sin(x), 0), \quad \mathbf{B} = (-\sin(y), \sin(2x), 0), \quad p = \gamma, \quad (5.90)$$

with an initial magnetic potential given in (4.73),

$$A^z(0, x, y) = 0.5 \cos(2x) + \cos(y). \quad (5.91)$$



Contour plots of density.

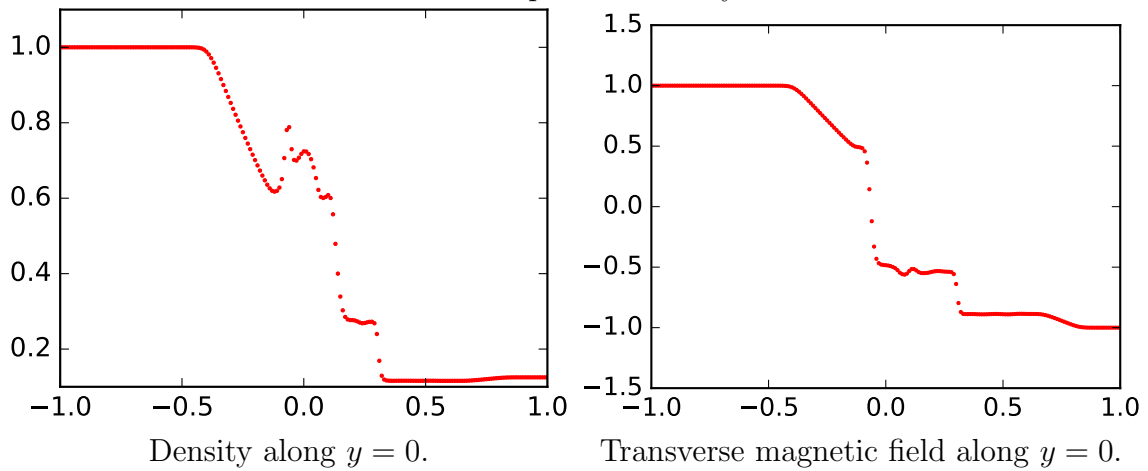
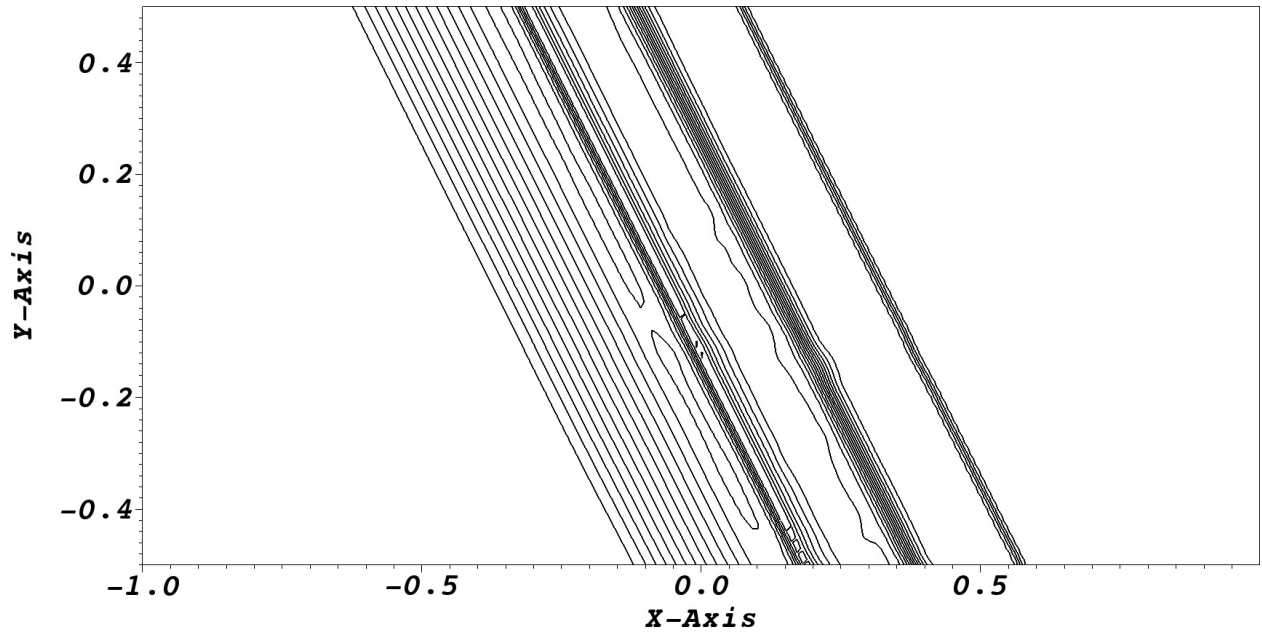


Figure 5.7: Rotated Brio-Wu shock tube. $t = 0.2$. Alternative WENO with Lax-Friedrichs flux. 200×100 uniform mesh. Constrained transport and positivity-preserving limiter turned off.



Contour plots of density.

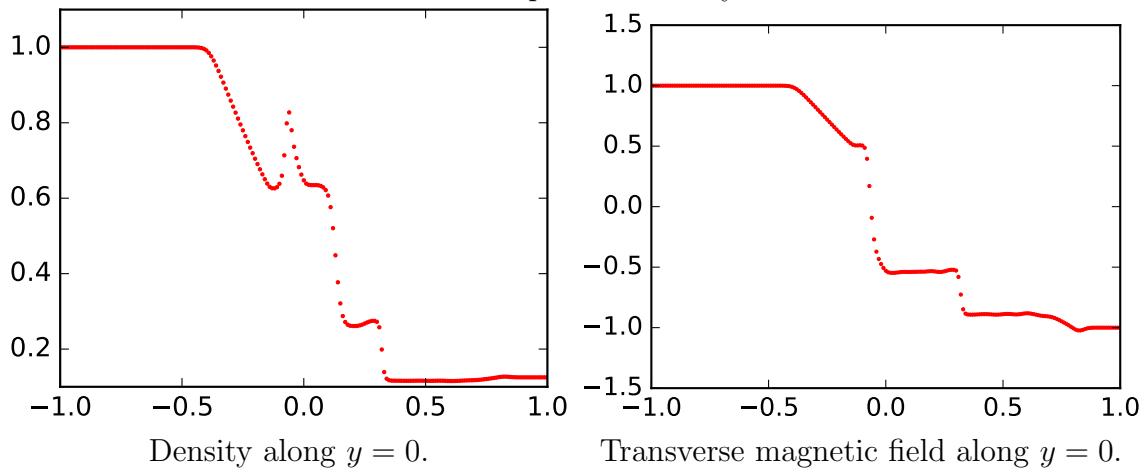
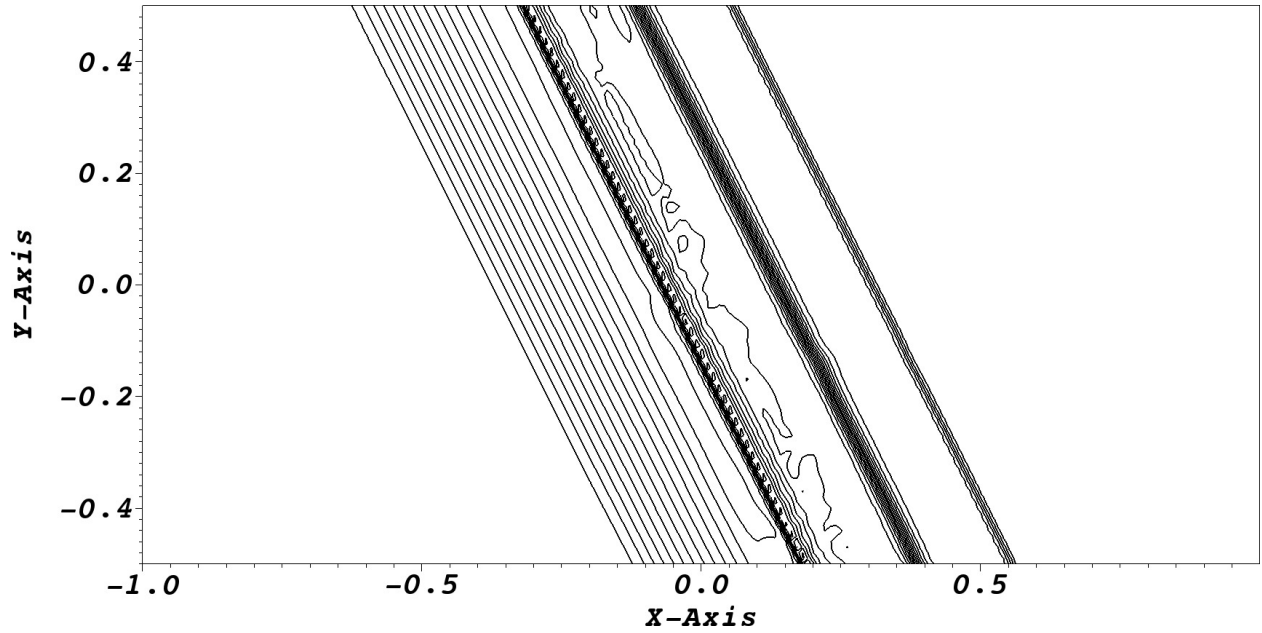


Figure 5.8: Rotated Brio-Wu shock tube. $t = 0.2$. Alternative WENO with Lax-Friedrichs flux. 200×100 uniform mesh. Constrained transport and positivity-preserving limiter turned on.



Contour plots of density.

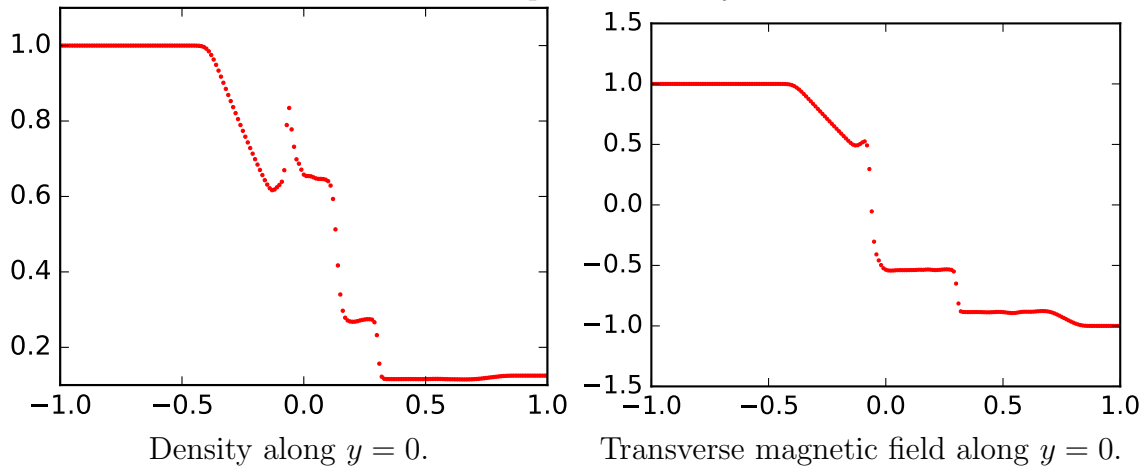


Figure 5.9: Rotated Brio-Wu shock tube. $t = 0.2$. Alternative WENO with HLLD flux. 200×100 uniform mesh. Constrained transport and positivity-preserving limiter turned on.

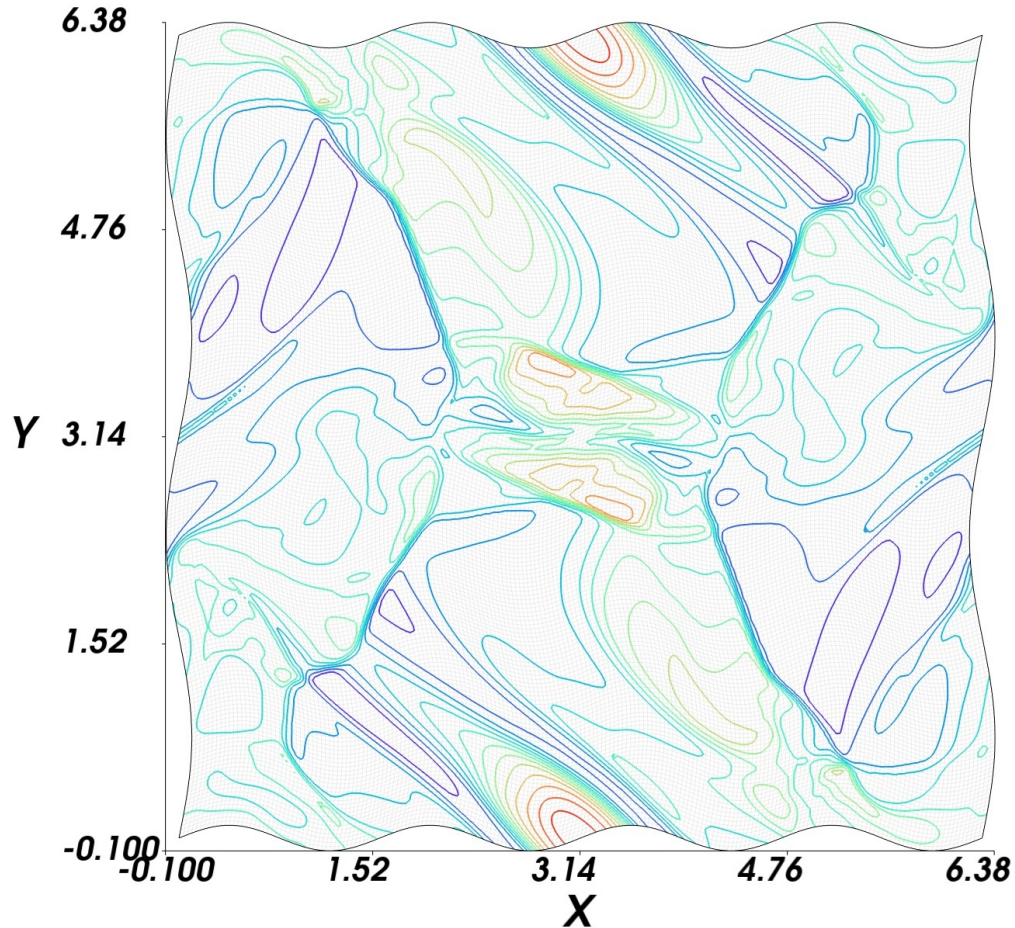


Figure 5.10: Orszag-Tang test problem. Contour plot of density at $t = 3$. A perturbed 192×192 mesh. 15 equally spaced contour lines. Alternative WENO with Lax-Friedrichs flux. Constrained transport and positivity-preserving limiter turned on.

The computational domain is $(\xi, \eta) \in [0, 2\pi] \times [0, 2\pi]$, and the mesh is given by

$$\begin{aligned} x &= \xi + \epsilon_x \sin(\eta a_x), \\ y &= \eta + \epsilon_y \sin(\xi a_y), \end{aligned} \tag{5.92}$$

where $\epsilon_x = 0.03$, $\epsilon_y = 0.05$, $a_x = 2$, and $a_y = 4$. We present the contour plots of the density at time $t = 3$ in Figures 5.10 and 5.11. The results agree with those found in the literature [23, 26, 71, 90, 94]. We note that we have also successfully run the simulation to the much later time of $t = 10$, which shows the robustness of the our scheme.

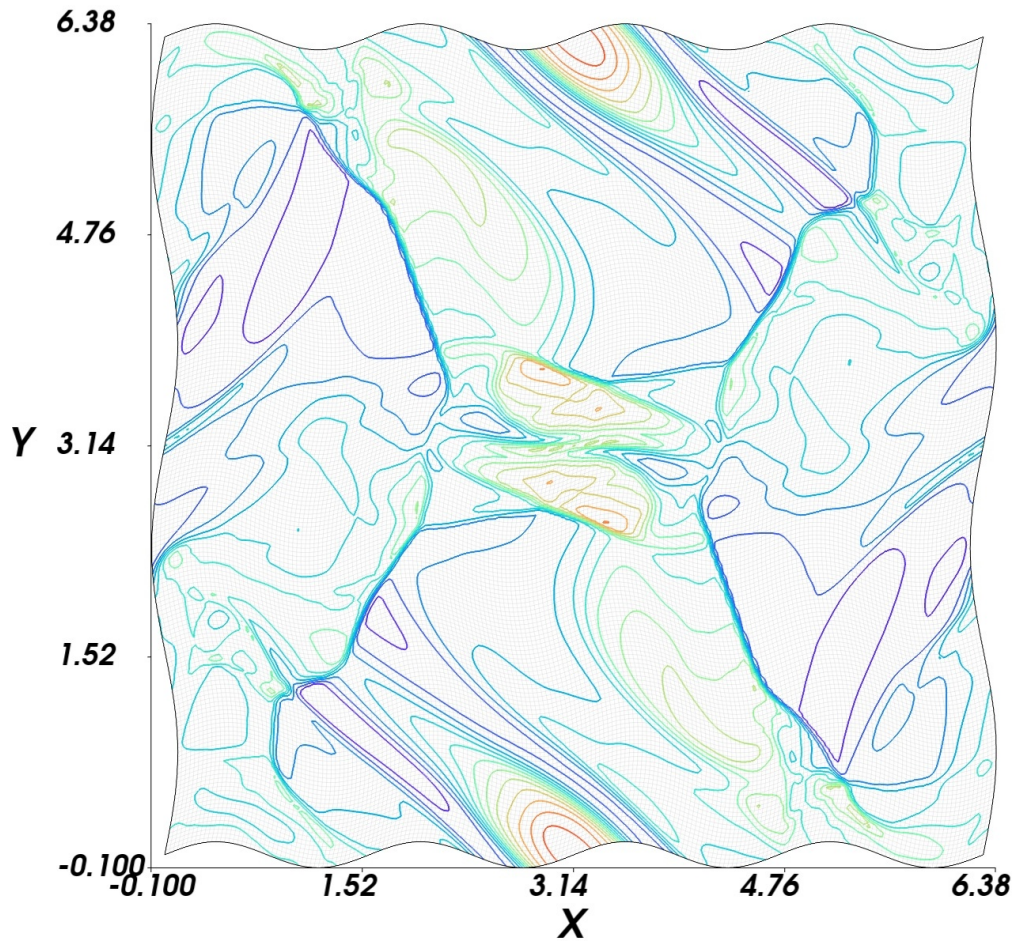


Figure 5.11: Orszag-Tang test problem. Plot of density at $t = 3$. A perturbed 192×192 mesh. 15 equally spaced contour lines. Alternative WENO with HLLD flux. Constrained transport and positivity-preserving limiter turned on.

5.5.4 2D cloud-shock interaction

In this section, we test the 2D cloud-shock interaction problem, which we tested in Section 4.5.5. The initial conditions were given in (4.79)

$$\begin{aligned}
 & (\rho, u^x, u^y, u^z, p, B^x, B^y, B^z) \\
 & = \begin{cases} (3.86859, 11.2536, 0, 0, 167.345, 0, 2.1826182, -2.1826182) & \text{if } x < 0.05, \\ (10, 0, 0, 0, 1, 0, 0.56418958, 0.56418958) & \text{if } x > 0.05, r < 0.15, \\ (1, 0, 0, 0, 1, 0, 0.56418958, 0.56418958) & \text{otherwise,} \end{cases}
 \end{aligned}$$

where $r = \sqrt{(x - 0.25)^2 + (y - 0.5)^2}$. The initial magnetic potential we use was given in (4.79),

$$A^z = \begin{cases} -2.1826182x + 0.080921431 & \text{if } x \leq 0.05, \\ -0.56418958x & \text{if } x \geq 0.05. \end{cases}$$

In Figures 5.12 and 5.13, we show results obtained by running the simulation on a 256×256 uniform mesh that covers the physical domain $(x, y) \in [0, 1] \times [0, 1]$. We note that the HLLD flux gives better resolution of shocks and other complex features. A similar phenomenon is also observed in Figures 5.15 and 5.16, where we show results obtained by running the simulation on a 256×256 non-uniform mesh determined by

$$\begin{aligned}
 x &= (3 - 2\xi) \cos(\pi + (1 - 2\eta)\pi/4) + 3 \cos(\pi/4), \\
 y &= (3 - 2\xi) \sin(\pi + (1 - 2\eta)\pi/4) + 0.5,
 \end{aligned} \tag{5.93}$$

where $(\xi, \eta) \in [0, 1] \times [0, 1]$.

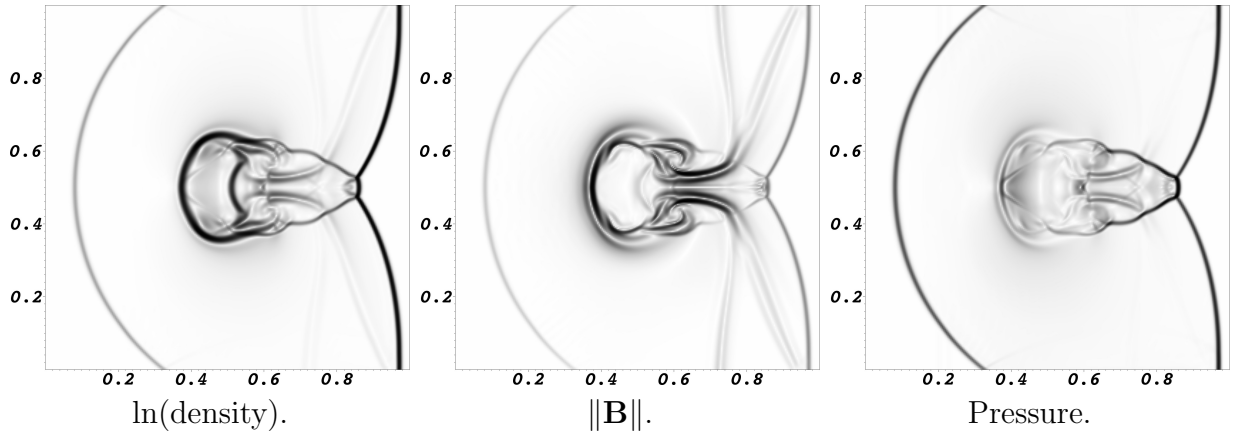


Figure 5.12: 2D cloud-shock interaction. Alternative WENO with Lax-Friedrichs flux. 256×256 uniform mesh. Schlieren plots at $t = 0.06$. Constrained transport and positivity-preserving limiter turned on.

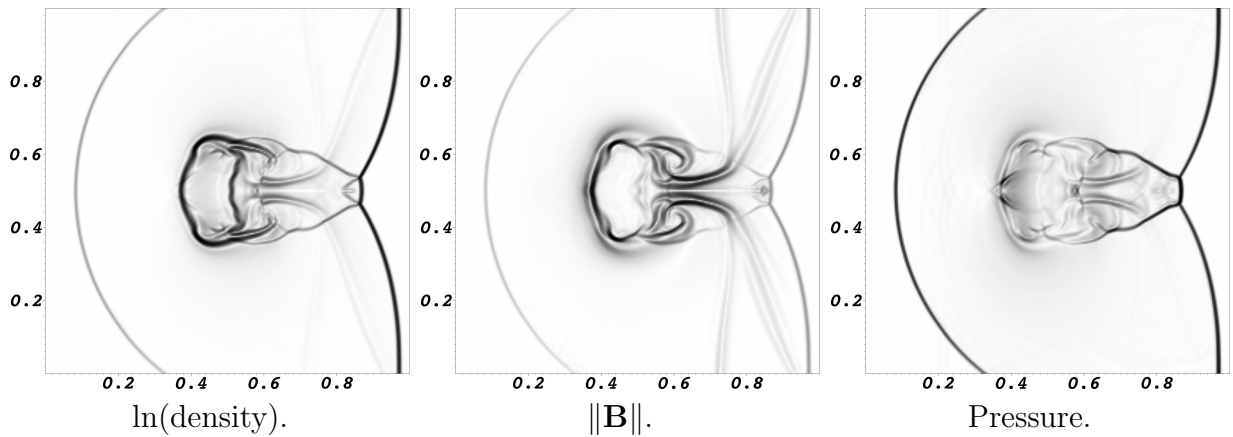


Figure 5.13: 2D cloud-shock interaction. Alternative WENO with HLLD flux. 256×256 uniform mesh. Schlieren plots at $t = 0.06$. Constrained transport and positivity-preserving limiter turned on.

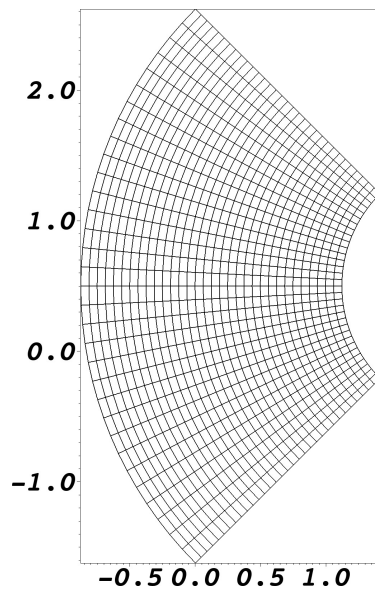


Figure 5.14: Sketch of the non-uniform mesh used in cloud-shock problem. Actual mesh is 256×256 . A 32×32 mesh is shown here for clarity.

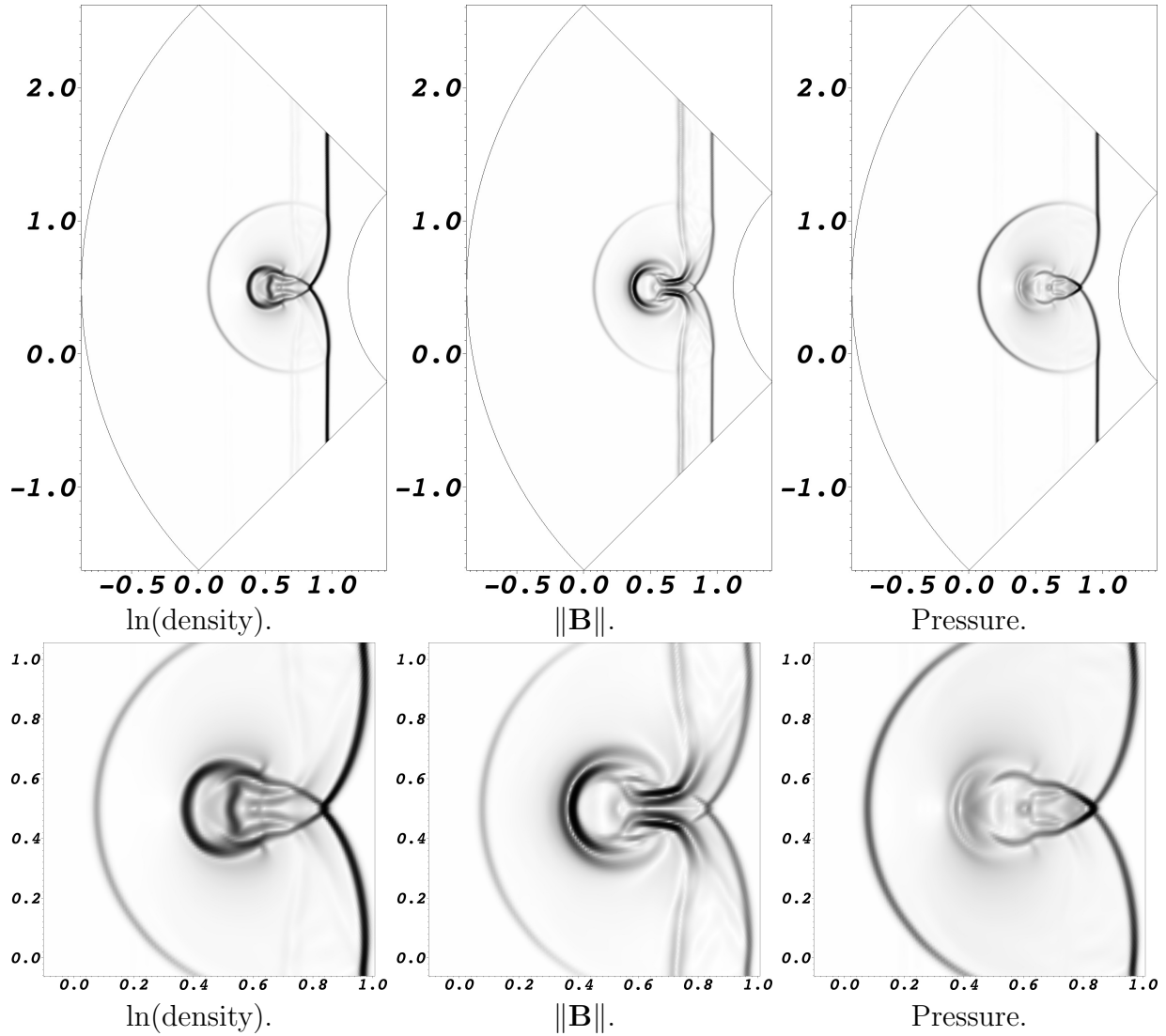


Figure 5.15: 2D cloud-shock interaction. Alternative WENO with Lax-Friedrichs flux. 256×256 non-uniform mesh. Schlieren plots at $t = 0.06$. Constrained transport and positivity-preserving limiter turned on. The second row shows the region near the center of the computational domain.

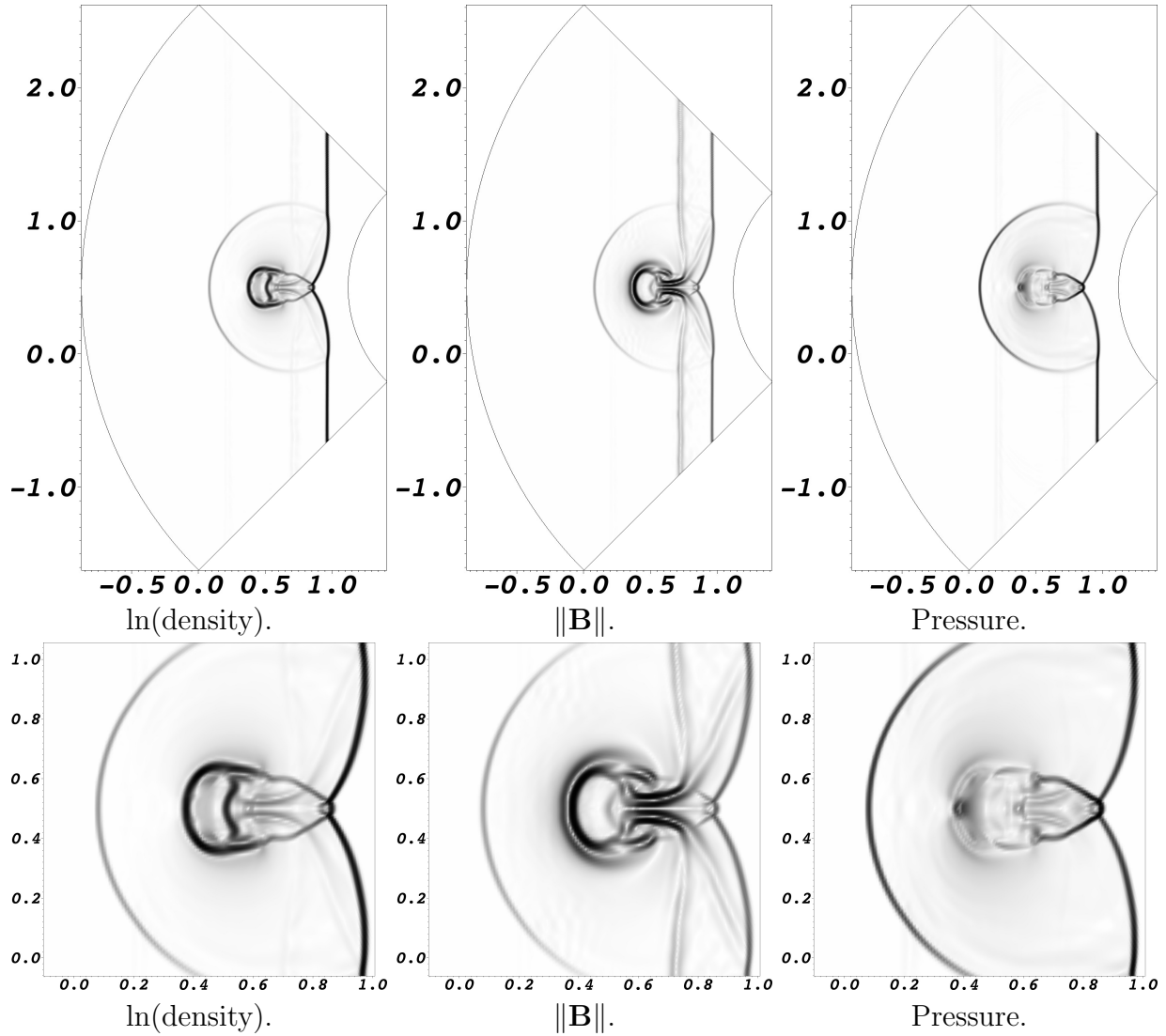


Figure 5.16: 2D cloud-shock interaction. Alternative WENO with HLLD flux. 256×256 non-uniform mesh. Schlieren plots at $t = 0.06$. Constrained transport and positivity-preserving limiter turned on. The second row shows the region near the center of the computational domain.

Chapter 6

Conclusions and future work

In this dissertation we proposed two high order finite difference schemes for the ideal magnetohydrodynamics.

The first scheme is single-stage single-step. The base scheme uses a finite difference WENO method with a Lax-Wendroff time discretization that is based on the Picard integral formulation of hyperbolic conservation laws. A discrete divergence-free condition on the magnetic field is enforced by using an unstaggered constrained transport method that evolves a vector potential alongside the conserved quantities on the same mesh as the conserved variables. This vector potential is evolved with a modified version of a finite difference Lax-Wendroff WENO method that was originally developed for Hamilton-Jacobi equations. This allows us to define non-oscillatory derivatives for the magnetic field. To further enhance the robustness of our scheme, a flux limiter is added to preserve the positivity of the density and pressure. Unlike our previous solvers that are based on SSP-RK time stepping [23, 22], this solver does not require the use of intermediate stages. This reduces the total storage required for the method, and may lead to more efficient implementation for an AMR setting. Moreover, we need only apply one WENO reconstruction per time step for the fluid variables, whereas the third and fourth-order solvers in [23] require three and ten, respectively, WENO reconstructions per time step. Numerical results show that our scheme has the expected high-order accuracy for smooth problems, and is capable of solving some very stringent test

problems.

The second scheme is based on an alternative flux formulation of the WENO scheme. In this formulation, the numerical flux is Taylor expanded in space. The leading (lowest order) term in the expansion is approximated by applying a Riemann solver on one-sided approximations to the conserved quantities on half grid points. These one-sided approximations are obtained by WENO interpolation. The higher order terms in the expansion is approximated by a combination of central differences and an additional limiter that is based on the smoothness indicators for WENO interpolation. Similar to our first scheme, an unstaggered constrained transport method is used to control the divergence error of the magnetic field. The magnetic potential is evolved using a WENO scheme originally designed for the Hamilton-Jacobi equations in the same way we did in [23, 22]. Also similar to our first scheme, a positivity-preserving flux limiter is applied to further enhance the robustness of the scheme. This scheme is also applied on curvilinear meshes, where we change the ideal MHD equations to a new hyperbolic system of conservation laws under the curvilinear coordinates and change the magnetic potential evolution equation to a new equation under the curvilinear coordinates. Numerical results shows that when we use the HLLD Riemann solver in the base scheme, the resolution of shocks and other complex features is better than what we would get by using the Lax-Friedrichs flux, which is comparable to the results we got by using the classical WENO scheme with Lax-Friedrichs flux splitting. The numerical results also demonstrated the robustness of our scheme, on both uniform and non-uniform meshes.

This dissertation serves as the starting point for the following directions of possible further explorations.

1. Single-stage single-step schemes based on the alternative flux formulation of the WENO

scheme. The work in [51] suggested that the alternative flux formulation can be made into a Lax-Wendroff type single-stage single-step scheme by applying the Cauchy-Kovalevskaya procedure similar to what we described in Chapter 4. Such a scheme would have an even smaller effective stencil than what we have in Chapter 4.

2. Treatment of more complex physical boundary conditions. The periodic and zeroth order extrapolation we used in our numerical examples are useful in areas such as simulations of galaxial formations and large-scale structures of matters in the universe. However, in areas such as solar system physics and thermonuclear fusion, more complex boundary conditions are needed and it is a non-trivial task to implement them in a high order finite difference scheme.
3. Incorporate the single-stage single-step scheme into AMR frameworks. This is an important motivation for work in this dissertation, as well as the work in [23, 22].

BIBLIOGRAPHY

BIBLIOGRAPHY

- [1] D. S. BALSARA, *Second-order-accurate schemes for magnetohydrodynamics with divergence-free reconstruction*, *Astrophys. J. Suppl. S.*, 151 (2004), p. 149.
- [2] ———, *Divergence-free reconstruction of magnetic fields and WENO schemes for magnetohydrodynamics*, *Journal of Computational Physics*, 228 (2009), pp. 5040–5056.
- [3] D. S. BALSARA, *Self-adjusting, positivity preserving high order schemes for hydrodynamics and magnetohydrodynamics*, *J. Comput. Phys.*, 231 (2012), pp. 7504–7517.
- [4] D. S. BALSARA, C. MEYER, M. DUMBSER, H. DU, AND Z. XU, *Efficient implementation of ADER schemes for Euler and magnetohydrodynamical flows on structured meshes—speed comparisons with Runge-Kutta methods*, *J. Comput. Phys.*, 235 (2013), pp. 934–969.
- [5] D. S. BALSARA, T. RUMPF, M. DUMBSER, AND C.-D. MUNZ, *Efficient, high accuracy ADER-WENO schemes for hydrodynamics and divergence-free magnetohydrodynamics*, *J. Comput. Phys.*, 228 (2009), pp. 2480–2516.
- [6] D. S. BALSARA AND C.-W. SHU, *Monotonicity preserving weighted essentially non-oscillatory schemes with increasingly high order of accuracy*, *J. Comput. Phys.*, 160 (2000), pp. 405–452.
- [7] D. S. BALSARA AND D. SPICER, *Maintaining pressure positivity in magnetohydrodynamic simulations*, *J. Comput. Phys.*, 148 (1999), pp. 133–148.
- [8] D. S. BALSARA AND D. S. SPICER, *A staggered mesh algorithm using high order Godunov fluxes to ensure solenoidal magnetic fields in magnetohydrodynamic simulations*, *J. Comput. Phys.*, 149 (1999), pp. 270–292.
- [9] J. W. BANKS AND W. D. HENSHAW, *Upwind schemes for the wave equation in second-order form*, *J. Comput. Phys.*, 231 (2012), pp. 5854–5889.
- [10] T. J. BARTH, *Numerical methods for gasdynamic systems on unstructured meshes*, in *An introduction to recent developments in theory and numerics for conservation laws*, Springer, 1999, pp. 195–285.
- [11] J. A. BITTENCOURT, *Fundamentals of Plasma Physics*, Springer New York, New York, NY, 2004.
- [12] J. P. BORIS AND D. L. BOOK, *Flux-corrected transport. I. SHASTA, a fluid transport algorithm that works* [*J. Comput. Phys.* **11** (1973), no. 1, 38–69], *J. Comput. Phys.*,

- 135 (1997), pp. 170–186. With an introduction by Steven T. Zalesak, Commemoration of the 30th anniversary of *J. Comput. Phys.*
- [13] W. BOSCHERI, M. DUMBSER, AND D. S. BALSARA, *High-order ADER-WENO ALE schemes on unstructured triangular meshes—application of several node solvers to hydrodynamics and magnetohydrodynamics*, *Internat. J. Numer. Methods Fluids*, 76 (2014), pp. 737–778.
- [14] J. U. BRACKBILL AND D. C. BARNES, *The effect of nonzero $\nabla \cdot \mathbf{B}$ on the numerical solution of the magnetohydrodynamic equations*, *J. Comput. Phys.*, 35 (1980), pp. 426–430.
- [15] M. BRIO AND C. C. WU, *Characteristic fields for the equations of magnetohydrodynamics*, in *Nonstrictly hyperbolic conservation laws (Anaheim, Calif., 1985)*, vol. 60 of *Contemp. Math.*, Amer. Math. Soc., Providence, RI, 1987, pp. 19–23.
- [16] L. CHACÓN, *A non-staggered, conservative, finite-volume scheme for 3D implicit extended magnetohydrodynamics in curvilinear geometries*, *Comput. Phys. Commun.*, 163 (2004), pp. 143–171.
- [17] Y. CHEN, G. TÓTH, AND T. I. GOMBOSI, *A fifth-order finite difference scheme for hyperbolic equations on block-adaptive curvilinear grids*, *J. Comput. Phys.*, 305 (2016), pp. 604–621.
- [18] Y. CHENG, F. LI, J. QIU, AND L. XU, *Positivity-preserving DG and central DG methods for ideal MHD equations*, *J. Comput. Phys.*, 238 (2013), pp. 255–280.
- [19] A. J. CHRISTLIEB, X. FENG, D. C. SEAL, AND Q. TANG, *A high-order positivity-preserving single-stage single-step method for the ideal magnetohydrodynamic equations*, *J. Comput. Phys.*, 316 (2016), pp. 218–242.
- [20] A. J. CHRISTLIEB, Y. GÜÇLÜ, AND D. C. SEAL, *The Picard integral formulation of weighted essentially nonoscillatory schemes*, *SIAM J. Numer. Anal.*, 53 (2015), pp. 1833–1856.
- [21] A. J. CHRISTLIEB, Y. LIU, Q. TANG, AND Z. XU, *High order parametrized maximum-principle-preserving and positivity-preserving WENO schemes on unstructured meshes*, *J. Comput. Phys.*, 281 (2015), pp. 334–351.
- [22] —, *Positivity-preserving finite difference weighted ENO schemes with constrained transport for ideal magnetohydrodynamic equations*, *SIAM J. Sci. Comput.*, 37 (2015), pp. A1825–A1845.

- [23] A. J. CHRISTLIEB, J. A. ROSSMANITH, AND Q. TANG, *Finite difference weighted essentially non-oscillatory schemes with constrained transport for ideal magnetohydrodynamics*, J. Comput. Phys., 268 (2014), pp. 302–325.
- [24] P. COLELLA, *Multidimensional upwind methods for hyperbolic conservation laws*, J. Comput. Phys., 87 (1990), pp. 171–200.
- [25] W. DAI AND P. R. WOODWARD, *On the divergence-free condition and conservation laws in numerical simulations for supersonic magnetohydrodynamical flows*, Astrophys. J., 494 (1998), p. 317.
- [26] W. DAI AND P. R. WOODWARD, *A simple finite difference scheme for multidimensional magnetohydrodynamical equations*, J. Comput. Phys., 142 (1998), pp. 331–369.
- [27] A. DEDNER, F. KEMM, D. KRÖNER, C.-D. MUNZ, T. SCHNITZER, AND M. WESSENBERG, *Hyperbolic divergence cleaning for the MHD equations*, J. Comput. Phys., 175 (2002), pp. 645–673.
- [28] W. D. D’HAESELEER, W. N. G. HITCHON, J. D. CALLEN, AND J. L. SHOHET, *Toroidal Flux Coordinates*, Springer Berlin Heidelberg, Berlin, Heidelberg, 1991, pp. 116–155.
- [29] A. DUBEY, K. ANTYPAS, A. C. CALDER, C. DALEY, B. FRYXELL, J. B. GALLAGHER, D. Q. LAMB, D. LEE, K. OLSON, L. B. REID, P. RICH, P. M. RICKER, K. M. RILEY, R. ROSNER, A. SIEGEL, N. T. TAYLOR, K. WEIDE, F. X. TIMMES, N. VLADIMIROVA, AND J. ZUHONE, *Evolution of FLASH, a multi-physics scientific simulation code for high-performance computing*, Int. J. High Perform. C., 28 (2014), pp. 225–237.
- [30] C. R. EVANS AND J. F. HAWLEY, *Simulation of magnetohydrodynamic flows – a constrained transport method*, Astrophys. J., 332 (1988), pp. 659–677.
- [31] S. A. FALLE AND S. S. KOMISSAROV, *On the inadmissibility of non-evolutionary shocks*, J. Plasma Phys., 65 (2001), pp. 29–58.
- [32] H. FENG AND J. WANG, *Observations of a $2 \rightarrow 3$ type interplanetary intermediate shock*, Solar Phys., 247 (2008), pp. 195–201.
- [33] M. FEY AND M. TORRILHON, *A constrained transport upwind scheme for divergence-free advection*, in Hyperbolic problems: theory, numerics, applications, Springer, Berlin, 2003, pp. 529–538.
- [34] T. A. GARDINER AND J. M. STONE, *An unsplit Godunov method for ideal MHD via constrained transport in three dimensions*, J. Comput. Phys., 227 (2008), pp. 4123–4141.

- [35] S. K. GODUNOV, *A difference method for numerical calculation of discontinuous solutions of the equations of hydrodynamics*, Mat. Sb. (N.S.), 47 (89) (1959), pp. 271–306.
- [36] GODUNOV, S. K., ZABRODIN, A. V., IVANOV, M. YA., KRAIKO, A. N., AND PROKOPOV, G. P., *Numerical solution of multidimensional problems of gas dynamics*, Izdat. “Nauka”, Moscow, 1976.
- [37] S. V. GOLOVIN, *Natural curvilinear coordinates for ideal MHD equations. non-stationary flows with constant total pressure*, Physics Letters A, 375 (2011), pp. 283 – 290.
- [38] T. I. GOMBOSI, K. G. POWELL, AND D. L. DE ZEEUW, *Axisymmetric modeling of cometary mass loading on an adaptively refined grid: Mhd results*, J. Geophys. Res. – Space, 99 (1994), pp. 21525–21539.
- [39] S. GOTTLIEB, C.-W. SHU, AND E. TADMOR, *Strong stability-preserving high-order time discretization methods*, SIAM Rev., 43 (2001), pp. 89–112 (electronic).
- [40] K. F. GURSKI, *An HLLC-type approximate Riemann solver for ideal magnetohydrodynamics*, SIAM J. Sci. Comput., 25 (2004), pp. 2165–2187 (electronic).
- [41] A. HARTEN, B. ENGQUIST, S. OSHER, AND S. R. CHAKRAVARTHY, *Uniformly high-order accurate essentially nonoscillatory schemes. III*, J. Comput. Phys., 71 (1987), pp. 231–303.
- [42] A. HARTEN, P. D. LAX, AND B. VAN LEER, *On upstream differencing and Godunov-type schemes for hyperbolic conservation laws*, SIAM Rev., 25 (1983), pp. 35–61.
- [43] C. HELZEL, J. A. ROSSMANITH, AND B. TAETZ, *An unstaggered constrained transport method for the 3D ideal magnetohydrodynamic equations*, J. Comput. Phys., 230 (2011), pp. 3803–3829.
- [44] ———, *A high-order unstaggered constrained-transport method for the three-dimensional ideal magnetohydrodynamic equations based on the method of lines*, SIAM J. Sci. Comput., 35 (2013), pp. A623–A651.
- [45] W. D. HENSHAW, *A high-order accurate parallel solver for Maxwell’s equations on overlapping grids*, SIAM Journal on Scientific Computing, 28 (2006), pp. 1730–1765.
- [46] P. JANHUNEN, *A positive conservative method for magnetohydrodynamics based on HLL and Roe methods*, J. Comput. Phys., 160 (2000), pp. 649–661.
- [47] S. C. JARDIN, *Review of implicit methods for the magnetohydrodynamic description of magnetically confined plasmas*, J. Comput. Phys., 231 (2012), pp. 822–838.

- [48] A. JEFFREY AND T. TANIUTI, *Non-linear wave propagation*, Mathematics in Science and Engineering, New York: Academic Press, 1964, 1 (1964).
- [49] G.-S. JIANG AND C.-W. SHU, *Efficient implementation of weighted ENO schemes*, J. Comput. Phys., 126 (1996), pp. 202–228.
- [50] G.-S. JIANG AND C.-C. WU, *A high-order WENO finite difference scheme for the equations of ideal magnetohydrodynamics*, J. Comput. Phys., 150 (1999), pp. 561–594.
- [51] Y. JIANG, C.-W. SHU, AND M. ZHANG, *An alternative formulation of finite difference weighted ENO schemes with Lax-Wendroff time discretization for conservation laws*, SIAM J. Sci. Comput., 35 (2013), pp. A1137–A1160.
- [52] —, *Free-stream preserving finite difference schemes on curvilinear meshes*, Methods Appl. Anal., 21 (2014), pp. 1–30.
- [53] M. G. KIVELSON AND C. T. RUSSELL, *Introduction to Space Physics*, Cambridge University Press, 1995.
- [54] P. LAX AND B. WENDROFF, *Systems of conservation laws*, Comm. Pure Appl. Math., 13 (1960), pp. 217–237.
- [55] R. J. LEVEQUE, *Numerical Methods for Conservation Laws*, Lectures in Mathematics ETH Zürich, Birkhäuser Verlag, Basel, second ed., 1992.
- [56] —, *Finite Volume Methods for Hyperbolic Problems*, Cambridge Texts in Applied Mathematics, Cambridge University Press, Cambridge, 2002.
- [57] F. LI, L. XU, AND S. YAKOVLEV, *Central discontinuous Galerkin methods for ideal MHD equations with the exactly divergence-free magnetic field*, J. Comput. Phys., 230 (2011), pp. 4828–4847.
- [58] S. LI, *An HLLC Riemann solver for magneto-hydrodynamics*, J. Comput. Phys., 203 (2005), pp. 344–357.
- [59] S. LI AND H. LI, *A modern code for solving magnetohydrodynamics or hydrodynamic equations*, tech. rep., Los Alamos National Lab., 2003.
- [60] X.-D. LIU, S. OSHER, AND T. CHAN, *Weighted essentially non-oscillatory schemes*, J. Comput. Phys., 115 (1994), pp. 200–212.
- [61] P. LONDRILLO AND L. D. ZANNA, *High-order upwind schemes for multidimensional magnetohydrodynamics*, The Astrophysical Journal, 530 (2000), p. 508.

- [62] P. MCCORQUODALE AND P. COLELLA, *A high-order finite-volume method for conservation laws on locally refined grids*, Commun. Appl. Math. Comput. Sci., 6 (2011), pp. 1–25.
- [63] A. MIGNONE AND P. TZEFERACOS, *A second-order unsplit Godunov scheme for cell-centered MHD: the CTU-GLM scheme*, J. Comput. Phys., 229 (2010), pp. 2117–2138.
- [64] T. MIYOSHI AND K. KUSANO, *A multi-state HLL approximate Riemann solver for ideal magnetohydrodynamics*, J. Comput. Phys., 208 (2005), pp. 315–344.
- [65] S. OSHER AND C.-W. SHU, *High-order essentially nonoscillatory schemes for Hamilton-Jacobi equations*, SIAM J. Numer. Anal., 28 (1991), pp. 907–922.
- [66] J. QIU, *WENO schemes with Lax-Wendroff type time discretizations for Hamilton-Jacobi equations*, J. Comput. Appl. Math., 200 (2007), pp. 591–605.
- [67] J. QIU, M. DUMBSER, AND C.-W. SHU, *The discontinuous Galerkin method with Lax-Wendroff type time discretizations*, Comput. Methods Appl. Mech. Engrg., 194 (2005), pp. 4528–4543.
- [68] J. QIU AND C.-W. SHU, *Finite difference WENO schemes with Lax-Wendroff-type time discretizations*, SIAM J. Sci. Comput., 24 (2003), pp. 2185–2198.
- [69] P. L. ROE, *Approximate Riemann solvers, parameter vectors, and difference schemes*, J. Comput. Phys., 43 (1981), pp. 357–372.
- [70] M. ROSENBLUTH AND M. BUSSAC, *MHD stability of spheromak*, Nucl. Fusion, 19 (1979), p. 489.
- [71] J. A. ROSSMANITH, *An unstaggered, high-resolution constrained transport method for magnetohydrodynamic flows*, SIAM J. Sci. Comput., 28 (2006), pp. 1766–1797.
- [72] D. D. SCHNACK, *Lectures in Magnetohydrodynamics*, vol. 780 of Lecture Notes in Physics, Springer-Verlag, Berlin, 2009.
- [73] D. C. SEAL, Q. TANG, Z. XU, AND A. J. CHRISTLIEB, *An explicit high-order single-stage single-step positivity-preserving finite difference WENO method for the compressible Euler equations*, J. Sci. Comput., (2015), pp. 1–20.
- [74] C. SHEN, J.-M. QIU, AND A. CHRISTLIEB, *Adaptive mesh refinement based on high order finite difference WENO scheme for multi-scale simulations*, J. Comput. Phys., 230 (2011), pp. 3780–3802.
- [75] Y. SHEN, G. ZHA, AND M. A. HUERTA, *E-CUSP scheme for the equations of ideal magnetohydrodynamics with high order WENO scheme*, J. Comput. Phys., 231 (2012), pp. 6233–6247.

- [76] C.-W. SHU, *Essentially non-oscillatory and weighted essentially non-oscillatory schemes for hyperbolic conservation laws*, in *Advanced numerical approximation of nonlinear hyperbolic equations* (Cetraro, 1997), vol. 1697 of *Lecture Notes in Math.*, Springer, Berlin, 1998, pp. 325–432.
- [77] —, *High order weighted essentially nonoscillatory schemes for convection dominated problems*, *SIAM Rev.*, 51 (2009), pp. 82–126.
- [78] C.-W. SHU AND S. OSHER, *Efficient implementation of essentially non-oscillatory shock-capturing schemes*, *J. Comput. Phys.*, 77 (1988), pp. 439–471.
- [79] —, *Efficient implementation of essentially non-oscillatory shock-capturing schemes,II*, *J. Comput. Phys.*, 83 (1989), pp. 32–78.
- [80] A. STEGMEIR, D. COSTER, O. MAJ, AND K. LACKNER, *Numerical methods for 3d tokamak simulations using a flux-surface independent grid*, *Contrib. Plasm. Phys.*, 54 (2014), pp. 549–554.
- [81] D. P. STERN, *The art of mapping the magnetosphere*, *J. Geophys. Res.-Space*, 99 (1994), pp. 17169–17198.
- [82] J. M. STONE, T. A. GARDINER, P. TEUBEN, J. F. HAWLEY, AND J. B. SIMON, *Athena: a new code for astrophysical MHD*, *Astrophys. J. Suppl. S.*, 178 (2008), p. 137.
- [83] K. TAKAHASHI AND S. YAMADA, *Regular and non-regular solutions of the Riemann problem in ideal magnetohydrodynamics*, *J. Plasma Phys.*, 79 (2013), pp. 335–356.
- [84] —, *Exact Riemann solver for ideal magnetohydrodynamics that can handle all types of intermediate shocks and switch-on/off waves*, *J. Plasma Phys.*, 80 (2014), pp. 255–287.
- [85] V. A. TITAREV AND E. F. TORO, *ADER: arbitrary high order Godunov approach*, *J. Sci. Comput.*, 17 (2002), pp. 609–618.
- [86] E. F. TORO, *Riemann solvers and numerical methods for fluid dynamics*, Springer-Verlag, Berlin, third ed., 2009. A practical introduction.
- [87] E. F. TORO, R. C. MILLINGTON, AND L. A. M. NEJAD, *Towards very high order Godunov schemes*, in *Godunov methods* (Oxford, 1999), Kluwer/Plenum, New York, 2001, pp. 907–940.
- [88] E. F. TORO, M. SPRUCE, AND W. SPEARES, *Restoration of the contact surface in the HLL-Riemann solver*, *Shock Waves*, 4 (1994), pp. 25–34.
- [89] M. TORRILHON, *Uniqueness conditions for Riemann problems of ideal magnetohydrodynamics*, *J. Plasma Phys.*, 69 (2003), pp. 253–276.

- [90] G. TÓTH, *The $\nabla \cdot B = 0$ constraint in shock-capturing magnetohydrodynamics codes*, J. Comput. Phys., 161 (2000), pp. 605–652.
- [91] K. WAAGAN, *A positive MUSCL-Hancock scheme for ideal magnetohydrodynamics*, J. Comput. Phys., 228 (2009), pp. 8609–8626.
- [92] C. WANG, X. DONG, AND C.-W. SHU, *Parallel adaptive mesh refinement method based on WENO finite difference scheme for the simulation of multi-dimensional detonation*, J. Comput. Phys., 298 (2015), pp. 161–175.
- [93] Z. XU, *Parametrized maximum principle preserving flux limiters for high order schemes solving hyperbolic conservation laws: one-dimensional scalar problem*, Math. Comp., 83 (2014), pp. 2213–2238.
- [94] A. L. ZACHARY, A. MALAGOLI, AND P. COLELLA, *A higher-order Godunov method for multidimensional ideal magnetohydrodynamics*, SIAM J. Sci. Comput., 15 (1994), pp. 263–284.
- [95] S. T. ZALESAK, *Fully multidimensional flux-corrected transport algorithms for fluids*, J. Comput. Phys., 31 (1979), pp. 335–362.
- [96] X. ZHANG AND C.-W. SHU, *On positivity-preserving high order discontinuous Galerkin schemes for compressible Euler equations on rectangular meshes*, J. Comput. Phys., 229 (2010), pp. 8918–8934.
- [97] U. ZIEGLER, *A central-constrained transport scheme for ideal magnetohydrodynamics*, J. Comput. Phys., 196 (2004), pp. 393–416.